Non Orthogonal Stagnation Point Flows with Rheological Characteristics

By

Rashid Mehmood

Department of Mathematics
Quaid-i-Azam University
Islamabad, Pakistan
2015

Non Orthogonal Stagnation Point Flows with Rheological Characteristics

By

Rashid Mehmood

Supervised By

Dr. Sohail Nadeem

Department of Mathematics
Quaid-i-Azam University
Islamabad, Pakistan
2015

Non Orthogonal Stagnation Point Flows with Rheological Characteristics

By

Rashid Mehmood

A Dissertation Submitted in the Partial Fulfillment of the Requirements

for the Degree of

DOCTOR OF PHILOSOPHY

IN

MATHEMATICS

Supervised By

Dr. Sohail Nadeem

Department of Mathematics
Quaid-i-Azam University
Islamabad, Pakistan
2015

Non Orthogonal Stagnation Point Flows with Rheological Characteristics

By

Rashid Mehmood

CERTIFICATE

A Dissertation Submitted in the Partial Fulfillment of the Requirements for the Degree of the Doctor of Philosophy

WE ACCEPT THIS DISSERTATION AS CONFORMING TO THE REQUIRED STANDARD

1. _____
Dr. Sohail Nadeem
(Supervisor)

2. _____
Prof. Dr. Tasawar Hayat
(Chairman)

3. _____
Dr. Khalid Hanif
(External Examiner)

4. _____
Dr. Muhammad Salahuddin
(External Examiner)

Department of Mathematics
Quaid-i-Azam University
Islamabad, Pakistan
2015

All praise is to Allah, the Lord of the Creation. The Most Gracious, the Most Merciful. Owner of the Day of Recompense. Who blessed us being the Ummah of His Beloved Prophet Muhammad (P.B.U.H), who blessed us with the most precious treasure of Iman (Faith). Countless Salutations, Peace and Blessings of Allah be upon the Cream of the Creation; Mercy for all Worlds; Seal of the Prophets Sayyiduna wa Mawlana Muhammadur Rasoolullah Sallallaho Alaihi wa Sallam, His Blessed Parents, His entire Family, His Progeny, His Companions and all those who Follow Him!!

I express my deepest and heart-felt gratitude to my supervisor, Dr. Sohail Nadeem for his knowledgeable discussions, valuable guidance and inexhaustible inspiration throughout my research time. His sympathetic attitude and encouragement prop up me to work harder with deep interest. Whatever I had learned and achieve today is all because of his splendid support. May Allah bless him with Long and Healthy life.

I am also grateful to the chairman, Department of Mathematics, Prof. Dr. Tasawar Hayat because he really inspired me to work hard and to follow his footsteps in research work.

I am very much grateful to my Father and Mother for their continuous support throughout my career. With tear in my eyes, with a sour throat I just cannot find true words at the moment that can truly reflect my regards and respects for my late great mother. Without her I could never ever have achieved this success in my life. May Allah almighty bless her with the highest rewards in the heaven. I am extremely thankful to my brothers and sister, some very special relations for their prayers, encouragement and support. A very special thanks to some of my very special friends Fahad, Salman, Zeeshan (Shani), Taha, Fani, Farrukh, Ahmed Jamal, Farhan, Sabir, Atif, Navid Usmani, Tayyab, Sajjad, Rizwan, Ashfaq Bhai, Bilal, Usman, Jamil, Zafar, Afzal, Mudasir and Qasim Bahi for being always with me. I am sorry if I missed someone in the above list.

At the end exceptional thanks to Noreen Baji, Ehnber and my junior colleagues and sisters, Hina, Shagufta and Iqra for their moral support.

Rashid Mehmood

Contents

Nomenclature

T_w, T_∞	Wall and ambient fluid temperature
C_w, C_∞	Wall and ambient fluid concentration
C_p	Specific heat of the material
α^*	Thermal diffusivity of the fluid
x^*, y^*	Cartesian co ordinates measured along surface
u^*, v^*	Velocity components along x and y axis
p^*	Fluid pressure
T^*, C^*	Fluid Temperature and Concentration
D_B, D_T	Brownian diffusion and thermophoresis coefficient
$(\rho c)_p, (\rho c)_f$	Effective heat capacity of nanofluid and fluid
a/c	Stretching ratio
β	non − Newtonian Casson parameter
ω	Slip parameter
M	Hartman number
Nb	Brownian motion parameter
Nt	Thermophoresis parameter
Sc	Schmidt number
K	Jeffery fluid parameter
Pr	Prandtl number
We	Weissenberg number
K_w	Local Weissenberg number
Bi	Biot number
S_r	Soret number
D_f	Dufour number
δ	non − dimensional relaxation time

λ	Heat source/sink parameter
ν	Kinematic viscosity
ψ	Stream function
$f'(y)$	Normal velocity profile
$h'(y)$	Tangential velocity profile
$\theta(y)$	Dimensionless Temperature
$\phi(y)$	Dimensionless Concentration
$f''(0)$	Normal skin friction co − efficient
$h'(0)$	Tangential friction co − efficient

Chapter 1

Introduction

Stagnation point flows are universal as they certainly appear to be composite flow fields. Such flows are either stagnated by a compact wall or by means of a free stagnation point in the fluid domain. They can be viscous or in viscid, steady or unsteady, 2D or 3D and orthogonal or non-orthogonal. The typical problems of 2D and 3D stagnation point flow are manipulated by Hiemenz [1] and Howarth [2] respectively. The 2D stagnation point flow is among the most widely studied problems in the field of fluid dynamics. Such flows arise when a fluid slants the boundary of a surface, for example, on an aircraft wing or on an oscillating cylinder immersed in fluid. These flows have a stagnation-point existent in the fluid and their streamlines locally look like those nearby a saddle point. Blood flow at a junction within an artery can be considered as an example of such flows. Stuart [3] devised the non-orthogonal stagnation point flow over a flat surface, an idea which was later on invigorated by Tamada [4] and Dorrepaal [5]. Stagnation point flow is a problem of speculative and practical interest in terms of heat transfer analysis. The importance of stagnation point heat transfer in problems such as atmospheric re-entry and other esoteric hypersonic flows make reckoning the heat transfer, a problem of concrete engineering concern. Chiam [6] discussed the stagnated flow towards a stretched surface. Gupta et al [7] investigated heat transfer in stagnation point flow towards stretching sheet. Mahapatra et al [8] and Ishak et al [9] investigated hydro magnetic stagnation-point flow towards a stretching and shrinking surface respectively. Reza et al [10] examined the steady oblique stagnation point flow passed a stretching surface. Lok et al [11] discussed non-orthogonal stagnation point flow of a micropolar fluid. Gupta et al [12] inferred the viscoelastic fluid flow for the case of a slanted

stagnation-point and later on highlighted some useful aspects of non-orthogonal stagnation point flow over a stretched surface [13]. Pop et al [14] examined the heat transfer of a non-orthogonal stagnation point flow in a non-Newtonian fluid. Similarly, Bagheri et al [15] analytically discussed the problem of non-orthogonal stagnation point flow over a flat sheet. Recently, rheological fluids are much appreciated for their importance in industrial applications such as extrusion of plastic sheets, fabrication of adhesives and in coating of inelastic substrates. It applies to substances which have a complex structure including muds, sludge's, suspensions, emulsions and other biological materials. Rheological fluids are more complex in nature so their non-dimensional properties are not easy to understand. Walters [16] discussed the second-order effects in elasticity. Among the class of several other non-Newtonian fluids one important fluid model is the Maxwell fluid model [17]. This model has the beauty that it relates the relaxation time with the stress which proves to be very valuable in defining the response of geological and many other polymeric fluids [18]. Nakamura et al [19] numerically studied the flow through an axisymmetric stenosis considering non-Newtonian fluid. Similarly Abel et al [20] investigated hydromagnetic viscoelastic fluid with heat source and variable thermal conductivity. Recently, Ahmad and Asghar [21] conducted a valuable study on flow of a MHD second grade fluid over an arbitrary stretching sheet. Liao et al [22] analysed the non-Newtonian flow over a stretching surface. Xu et al [23] analytically discussed unsteady MHD flow over a stretching surface. Nazar et al [24] numerically deliberated three-dimensional viscoelastic flow past a stretching surface. Prasad et al [25] discussed MHD viscoelastic fluid with variable viscosity.

In certain engineering processes like paper production, glass blowing, crystal growing and metal spinning, heat transfer at the stretching surface is dynamic since it is closely related with the

quality of final product. Therefore, it is exceptionally valuable if we can control the heat transfer rate at the surface. A nano fluid comes up with the solution to meet such debits. Choi [26] devised the notable concept of nanofluids. In fact the notion of nanofluids have become a topic of global interest in the last few decades as they provide an effective way of improving heat transfer characteristics of fluids. It is expected that nanofluids have higher thermal conductivity than that of common fluids. Heat transfer fluids like water, Oil and Glycols are extensively used in industrial and civil applications such as hot metal shears, fire-resistance, air conditioning, electric cooling etc but they possess low thermal conductivity. In order to overcome this deficiency, thermally conductive Nano meter sized particles (1-100 nm) are suspended in fluid to accelerate heat transfer at the wall. Putra et al [27] studied the natural convection of nano fluids. Li et al [28] highlighted some useful features of nano fluids. Buongiorno [29] presented a mathematical model to describe the flow characteristics of nano fluids. Nield [30] discussed the flow of a nano fluid past a vertical surface with natural convection. Ishak et al [31] inspected the stagnation-point flow over a stretched sheet in a nano fluid. Hydro-magnetic fluids are given a lot of respect in the last few decades as they can be quite useful in certain flow problems like in refrigeration coils, pumps, power generators, filament cooling and in the purification process of liquid metals. Anderson [32] discussed the MHD flow of a viscoelastic fluid past a stretching surface. Pop et al [33] re-investigated the similar kind of problem for the case of stagnation point flow. Ellahi et al [34] presented the analytical solutions of MHD third-grade fluid flow with variable viscosity. Nazar et al [35] inspected the influence of induced magnetic field on flow over a stretching surface. It is a well-known fact that no-slip condition for various rheological fluids is not good enough, as certain polymer melts exhibits wall slip. Such kind of flows have their own applications like in synthetic heart valves refining and flows in interior cavities. Navier

[36] suggested that this wall slip can be related with the shear stress of the fluid. Later on, a number of researchers have invoked this astonishing concept in their studies. Anderson [37] discussed the flow over a stretching surface with slip factor. Wang [38] perceived the partial slip flow on a stretching surface and further extended the work for stagnation point flows with slip [39]. Fotini et al [40] examined the stagnation point flow for Walter's B fluid in the presence of surface slip. In another article, Ariel [41] addressed stagnation point slip flow assuming non-Newtonian fluid. Turkyilmazoglu [42] presented multiple solutions of MHD viscoelastic slip flow over a stretching sheet. Fluid flows over convective surface are beneficial precisely in processes like filtration, petroleum recovery, thermal energy storage and nuclear plants etc. Aziz [43] examined the thermal boundary layer on a convective flat plate. Makinde [44] deliberated hydro magnetic flow over a convective vertical plate. Similarly Ishak [45] discussed flow over a permeable convective surface with heat transfer. In another article, Olanrewaju et al [46] interpreted flow over a vertically stretching surface with buoyancy effects and convective boundary condition. Aziz [47] deliberated a study on MHD flow with constant heat flux and later on inspected the MHD mixed convective flow past a vertical plate inserted in a porous medium [48]. MHD flow over a convective moving vertical plate has been investigated by Makinde [49]. Rundora et al [50] highlighted the effects of variable viscosity on non-Newtonian fluid with porous medium and asymmetric convective surface. Soret effect is basically a diffusion flux which occurs due to temperature gradient in the flow, whereas Dufour effect measures the heat flux because of a chemical potential gradient. These effects have their own importance in the areas of geoscience and chemical engineering. Diffusion-thermo effect is extremely vital in isotropic separation among gases having various molecular weights. Huang et al [51] studied Hiemenz flow over a porous stretching surface with soret and dufour effects. Prasad et al [52]

numerically explored Soret and Dufour effects on MHD convective flow over a stretched surface towards a porous medium. Afify [53] deliberated a useful study to discuss thermo diffusion effects on a free convective porous medium. Pal et al [54] investigated MHD mixed convective flow over a stretching sheet with soret dufour and chemical reaction.

Keeping in view all of the above mentioned aspects, stagnation point flows of rheological fluids over a stretching surface have been presented in which the flow approaches a surface obliquely. We have applied analytical technique optimal homotopy analysis method (OHAM) for the series solutions of governing nonlinear equations. Optimal homotopy analysis method (OHAM) proposed by Liao [55-62] is an extremely effective analytical technique to solve coupled highly nonlinear ordinary differential equations. In addition numerical schemes known as Spectral Quasilinearisation method (QLM), Spectral Local Linearization method (SLM) and mid-point integration scheme along with Richardson's extrapolation are applied to deal the governing system of differential equations [63-66].

The chapter wise analysis of this thesis is planned as follow:

Chapter 2 deals with the steady stagnation point flow of a Casson nano fluid with convective boundary condition. The fluid strikes the wall in an oblique manner. The prevailing nonlinear partial differential equations of the non-dimensional problem are presented and then converted into nonlinear ordinary differential equations by means of similar and non-similar variables. The consequential ordinary differential equations are successfully solved using Optimal Homotopy analysis method (OHAM). Non-dimensional velocities, temperature, nano particle concentration, skin friction co-efficient and local heat and mass flux profiles are discussed against emerging non-dimensional parameters. The contents of this chapter are **published in International**

Journal of Thermal Sciences. **(2014):78; 90-100.**

Simultaneous effects of partial slip and transversely applied uniform magnetic field on an oblique stagnation point rheological fluid over a stretched convective surface has been inspected in **chapter 3**. The prevailing momentum equations are designed by manipulating casson fluid model. The obtained differential equations are solved numerically through midpoint integration scheme together with Richardson's extrapolation. Numerical values of normal and tangential components of wall shear stress are tabulated. This chapter is **published in Journal of Magnetism and Magnetic Materials**. **(2015):378; 457-462.**

Chapter 4 is related to the steady oblique stagnation flow of Jeffery fluid over a stretching surface with convective boundary condition. Optimal homotopy analysis method (OHAM) is operated to deal the resulting ordinary differential equations. OHAM is found to be extremely effective analytical technique to obtain convergent series solutions of highly non-linear differential equations. Graphically, non-dimensional velocities and temperature profile are expressed. Numerical values of skin friction coefficients and heat flux are computed. This problem is **published in International Journal of Numerical Methods for Heat and fluid flow. (2015): 25; 454-471.**

The main intention of **chapter 5** is to present a comparative study on non-orthogonal stagnation point fluid flow using Jeffery nano fluid as a rheological fluid model. The effects of thermophoresis and Brownian motion are taken into account. Consequential highly non-linear system of differential equations is solved numerically through mid-point integration as a basic

scheme along with Richardson's extrapolation as an enhancement scheme and analytical results are also obtained using optimal homotopy analysis Method (OHAM). Numerical values of local skin friction coefficients, local heat and mass flux are tabulated numerically as well as analytically for various non-dimensional parameters emerging in the flow problem. The findings of this chapter are **submitted** for publication in **Neural Computing and Applications**.

Chapter 6 is presented to analyse the soret dufour effects on a steady, 2-D magneto hydrodynamic (MHD) stagnation point flow of an obliquely striking second grade fluid over a stretched convective surface. The governing systems of equations are solved numerically using midpoint integration scheme with Richardson's extrapolation. The results for normal and tangential components of velocity as well as temperature and concentration profiles are exhibited graphically and analysed. Numerical computations are performed to discover the influence of pertinent non-dimensional parameters on local skin friction co-efficient, heat and mass flux and are presented in tabulated form. This work is **published in European Non-dimensional Journal plus**. **(2014)129:182**

In Chapter 7, we have numerically investigated the oblique flow of a Walter-B type nano fluid over a stretching convective surface. Effects of transversely applied magnetic field are also taken into account. The governing system is presented in the form of highly nonlinear coupled ordinary differential equations by means of appropriate similarity transformations. These equations have been solved numerically using the Spectral Quasilinearization Method (QLM) and the Spectral Local Linearization Method (LLM). Numerical values of skin friction co-efficient, local heat and

mass flux are presented. This chapter is **published in International Journal of Thermal Sciences. (2015):95; 162-172.**

Chapter 8 studies the influence of internal heat generation/absorption on oblique stagnation point flow of a Maxwell fluid on a convective surface. By transforming the governing equations via suitable similarity transformations, numerical solutions are presented using the Spectral Quasilinearization Method (QLM) and Spectral Local Linearization Method (LLM). The velocity, temperature and local heat flux rate at the stretching convective surface are presented through graphs against pertinent flow parameters and analysed. The findings of this chapter are **submitted for publication in Applied Numerical Mathematics.**

Chapter 2

Optimized analytical solution for oblique flow of a Casson-nano fluid with convective boundary conditions

2.1 Introduction

This chapter deals with the steady stagnation point flow of a Casson nano fluid with convective boundary conditions. The fluid strikes the wall in an oblique manner. The governing nonlinear partial differential equations of the non-dimensional problem are presented and then converted into nonlinear ordinary differential equations by using similar and non-similar variables. The resulting ordinary differential equations are successfully solved analytically using Optimal Homotopy analysis method (OHAM). Non-dimensional velocities, temperature and nano particle concentration profiles are expressed through graphs. In order to understand the flow behavior at the stretching convective surface, Numerical values of skin friction co-efficient and local heat and mass flux are tabulated. Comparison of the present analysis with the previous existing literature is made and an appreciable agreement in the values is observed for the limiting case.

2.2 Mathematical formulation

Let us consider the steady 2D oblique flow of Casson-nano fluid over a stretching surface. Surface is stretched by means of two opposite forces of equal magnitude, as shown in Fig (2.1). We further assume that the surface has convective fluid temperature T_f and uniform ambient temperature T_∞ here ($T_f \rangle T_\infty$).

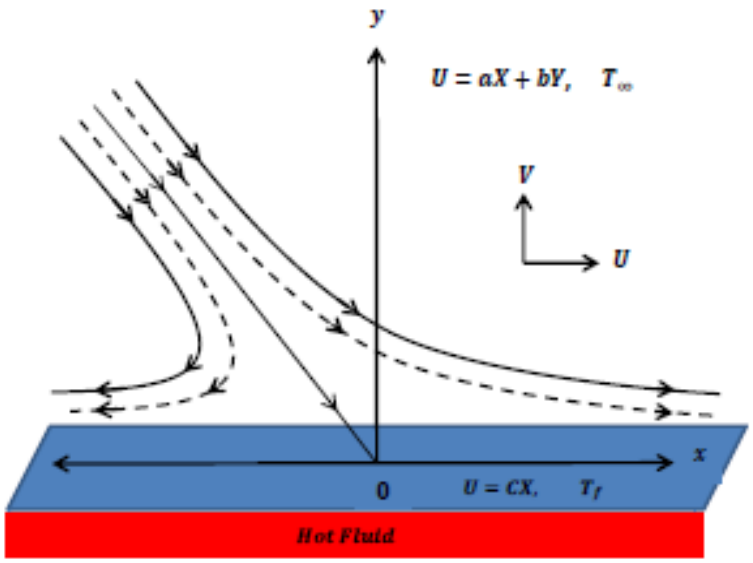

Fig (2.1) A non-dimensional description of the problem

The velocity, temperature and concentration functions are defined as

$$\mathbf{V}^*(x^*, y^*) = (u^*(x^*, y^*), v^*(x^*, y^*)), \qquad (2.1)$$

$$\mathbf{T}^* = \mathbf{T}^*(x^*, y^*), \mathbf{C}^* = \mathbf{C}^*(x^*, y^*). \qquad (2.2)$$

The governing equations of mass, momentum, energy and concentration are defined as

$$div\,\mathbf{V}^* = 0, \tag{2.3}$$

$$\rho_f \frac{d\mathbf{V}^*}{dt} = div\,\mathbf{S} + \mathbf{J} \times \mathbf{B}, \tag{2.4}$$

$$(\rho c)_f \frac{d\mathbf{T}^*}{dt} = -div\,q^* + (\rho c)_p (D_B \nabla^* \mathrm{C}^*.\nabla^* \mathrm{T}^* + \frac{D_T}{T_\infty} \nabla^* \mathrm{T}^*.\nabla^* \mathrm{T}^*), \tag{2.5}$$

$$\frac{d\mathbf{C}^*}{dt} = D_B \nabla^{*2} \mathrm{C}^* + \frac{D_T}{T_\infty} \nabla^{*2} \mathrm{T}^*, \tag{2.6}$$

Here $\mathbf{V}^*$ is the velocity, ρ_f is the fluid density, ρ_p is the nanoparticle mass density, $\mathbf{S}$ is the stress tensor, $\mathbf{T}^*$ is the temperature, $\mathbf{C}^*$ is the concentration, $q^* = -k\nabla^* \mathrm{T}^*$ is the heat flux, k is the thermal conductivity, D_B is the Brownian diffusion coefficient, D_T and is the thermophoresis coefficient.

The stress tensor $\mathbf{S}$ of a Casson fluid can be written as [19]

$$\mathbf{S} = -p\boldsymbol{I} + \begin{pmatrix} 2\left[\mu_B + \frac{p_y}{\sqrt{2\pi}}\right] e_{ij}, \pi > \pi_c \\ 2\left[\mu_B + \frac{p_y}{\sqrt{2\pi_c}}\right] e_{ij}, \pi_c > \pi \end{pmatrix} \tag{2.7}$$

where p denotes the pressure, $\boldsymbol{I}$ is the identity matrix, $\pi = e_{ij}.e_{ij}$ and e_{ij} is the $(i,j)^{th}$ deformation rate in component form, μ_B is the plastic dynamic viscosity of the non-Newtonian fluid, π is the product of the component of deformation rate with itself, π_c is a critical value of this product and p_y is yield stress of slurry fluid.

Invoking Eqs (2.1) and(2.2) in Eqs. (2.3)-(2.6), we have

$$\frac{\partial u^*}{\partial x^*} + \frac{\partial v^*}{\partial y^*} = 0 \tag{2.8}$$

$$u^* \frac{\partial u^*}{\partial x^*} + v^* \frac{\partial u^*}{\partial y^*} + \frac{1}{\rho_f} \frac{\partial p^*}{\partial x^*} = \nu(1 + \frac{1}{\beta}) \nabla^{*2} u^* \tag{2.9}$$

$$u^* \frac{\partial v^*}{\partial x^*} + v^* \frac{\partial v^*}{\partial y^*} + \frac{1}{\rho_f} \frac{\partial p^*}{\partial y^*} = \nu(1 + \frac{1}{\beta}) \nabla^{*2} v^* \tag{2.10}$$

$$u^* \frac{\partial T^*}{\partial x^*} + v^* \frac{\partial T^*}{\partial y^*} = \alpha^* \nabla^{*2} T^* + \frac{(\rho c)_p}{(\rho c)_f} (D_B \nabla^* C^*.\nabla^* T^* + \frac{D_T}{T_\infty} \nabla^* T^*.\nabla^* T^*), \tag{2.11}$$

$$u^* \frac{\partial C^*}{\partial x^*} + v^* \frac{\partial C^*}{\partial y^*} = D_B \nabla^{*2} C^* + \frac{D_T}{T_\infty} \nabla^{*2} T^*. \quad (2.12)$$

With the following boundary conditions [14]

$$u^* = cx^*, v^* = 0, -k \frac{\partial T^*}{\partial y^*} = h\left(T_f - T^*\right), C^* = C_w \; at \; y^* = 0,$$

$$u^* = ax^* + by^*, \; T^* \to T_\infty, C^* \to C_\infty \; as \; y^* \to \infty \quad (2.13)$$

In above expressions u^* and v^* are the velocity components along the $x^* -$ and $y^* -$ axes respectively, ν is the kinematic viscosity, C_p is the specific heat of the material, $\alpha^*$the thermal diffusivity, h is the convective heat transfer coefficient and a, b, c are positive constants having dimensions of inverse time.

Introducing the following quantities [14]

$$x = x^* \sqrt{\frac{c}{\nu}}, y = y^* \sqrt{\frac{c}{\nu}}, u = \frac{1}{\sqrt{\nu c}} u^*,$$

$$v = \frac{1}{\sqrt{\nu c}} v^*, p = \frac{1}{\sqrt{\mu c}} p^*, T = \frac{T^* - T_\infty}{T_f - T_\infty}, C = \frac{C^* - C_\infty}{C_w - C_\infty}. \quad (2.14)$$

Substituting Eq(2.14)into Eqs (2.8) -(2.12), we have

$$\frac{\partial u}{\partial x} + \frac{\partial v}{\partial y} = 0, \quad (2.15)$$

$$u \frac{\partial u}{\partial x} + v \frac{\partial u}{\partial y} + \frac{1}{\rho_f} \frac{\partial p}{\partial x} = \left(1 + \frac{1}{\beta}\right) \nabla^2 u, \quad (2.16)$$

$$u \frac{\partial v}{\partial x} + v \frac{\partial v}{\partial y} + \frac{1}{\rho_f} \frac{\partial p}{\partial y} = \left(1 + \frac{1}{\beta}\right) \nabla^2 v, \quad (2.17)$$

$$\Pr(u \frac{\partial T}{\partial x} + v \frac{\partial T}{\partial y}) = \nabla^2 T + Pr(N_b \nabla C . \nabla T + N_t \nabla T . \nabla T), \quad (2.18)$$

$$Sc \left(u \frac{\partial C}{\partial x} + v \frac{\partial C}{\partial y}\right) = \nabla^2 C + \frac{N_t}{N_b} \nabla^2 T. \quad (2.19)$$

Introducing the stream function relations

$$u = \frac{\partial \psi}{\partial y}, v = -\frac{\partial \psi}{\partial x}. \quad (2.20)$$

Substitution of Eq (2.20) into Eqs (2.15) -(2.19) and eliminating the pressure from the resulting equations using $P_{xy} = P_{yx}$ yield

$$\left(1+\frac{1}{\beta}\right)\nabla^4\psi + \frac{\partial(\psi,\nabla^2\psi)}{\partial(x,y)} = 0, \tag{2.21}$$

$$\Pr\left(\frac{\partial\psi}{\partial y}\frac{\partial T}{\partial x} - \frac{\partial\psi}{\partial x}\frac{\partial T}{\partial y}\right) = \nabla^2 T + Pr(N_b\nabla C.\nabla T + N_t\nabla T.\nabla T), \tag{2.22}$$

$$Sc\left(\frac{\partial\psi}{\partial y}\frac{\partial C}{\partial x} - \frac{\partial\psi}{\partial x}\frac{\partial C}{\partial y}\right) = \nabla^2 C + \frac{N_t}{N_b}\nabla^2 T. \tag{2.23}$$

The corresponding boundary conditions are defined as

$$\psi = 0, \frac{\partial\psi}{\partial y} = x, \frac{\partial T}{\partial x} = -\frac{h}{k}\sqrt{\frac{\nu}{c}}(1-T), = 1, C = 1 \; at \; y = 0,$$

$$\psi = \frac{a}{c}xy + \frac{1}{2}\gamma_1 y^2, T = 0, C = 0 \; at \; y \to \infty, \tag{2.24}$$

where $\gamma_1 = \frac{b}{c}$ denotes shear in the stream. We seek solutions of Eqs. $(2.21) - (2.23)$ of the following form [14]

$$\psi(x,y) = xf(y) + g(y), T = \theta(y), C = \phi(y), \tag{2.25}$$

where $f(y)$ and $g(y)$ are normal and tangential components of the flow, and prime indicates derivative with respect to y. Substituting Eq (2.25) in Eqs $(2.21) - (2.24)$, we obtain following system of coupled ordinary differential equations along with the corresponding boundary conditions

$$\left(1+\frac{1}{\beta}\right)f''' + ff'' - f'^2 + C_1 = 0, \tag{2.26}$$

$$\left(1+\frac{1}{\beta}\right)g''' + fg'' - f'g' + C_2 = 0, \tag{2.27}$$

$$\theta'' + Pr(f\theta' + N_b\theta'\phi' + N_t\theta'^2) = 0, \tag{2.28}$$

$$\phi'' + Scf\phi' + \frac{N_t}{N_b}\theta'' = 0, \tag{2.29}$$

$$f(0)=0, f'(0)=1, f'(\infty)=\frac{a}{c}, g(0)=0, g'(0)=0, g''(\infty)=\gamma_1,$$

$$\theta'(0)=-Bi\big(1-\theta(0)\big), \theta(\infty)=0, \phi(0)=1, \phi(\infty)=0, \quad (2.30)$$

where C_1 and C_2 represent integral constants. The non-Newtonian (Casson) parameter β, Prandtl number Pr, the thermophoresis parameter N_t, the Brownian motion parameter N_b, Biot number Bi and the Schmidt number Sc are defined as $[29-31]$

$$\beta=\mu_B\frac{\sqrt{2\pi_c}}{p_y}, Pr=\frac{\nu}{\alpha}, N_t=\frac{D_T}{T_\infty}\frac{(\rho c)_p}{(\rho c)_f}\frac{\big(T_f-T_\infty\big)}{\nu},$$

$$N_b=D_B\frac{(\rho c)_p}{(\rho c)_f}\frac{(C_w-C_\infty)}{\nu}, Bi=\frac{h}{k}\sqrt{\frac{\nu}{c}}, Sc=\frac{\nu}{D_B}. \quad (2.31)$$

Taking the limit $y\to\infty$ in Eq (2.26) and using the boundary condition $f'(\infty)=\frac{a}{c}$, we get $C_1=(\frac{a}{c})^2$. Eq. (2.26) reveals that $f(y)$ acts as $f(y)=\frac{a}{c}y+A$ at $y\to\infty$, where A is the boundary layer displacement constant. Taking $y\to\infty$ in Eq (2.27) and making use of the boundary condition at infinity $g''(\infty)=\gamma_1$, we get $C_2=-A\gamma_1$. Thus Eqs. $(2.26)-(2.29)$ become

$$\Big(1+\frac{1}{\beta}\Big)f'''+ff''-f'^2+(\frac{a}{c})^2=0, \quad (2.32)$$

$$\Big(1+\frac{1}{\beta}\Big)g'''+fg''-f'g'+-A\gamma_1=0, \quad (2.33)$$

$$\theta''+Pr(f\theta'+N_b\theta'\phi'+N_t\theta'^2)=0, \quad (2.34)$$

$$\phi''+Scf\phi'+\frac{N_t}{N_b}\theta''=0. \quad (2.35)$$

Note that in above equations when $\beta\to\infty$, we obtain the equations for viscous fluid ·

Introducing

$$g'(y)=\gamma_1 h(y). \quad (2.36)$$

Using Eq (2.36) in Eq (2.33), we have

$$\left(1+\frac{1}{\beta}\right)h''+fh'-f'h+-A=0, \tag{2.37}$$

With the boundary conditions

$$h(0)=0, h'(\infty)=1. \tag{2.38}$$

Quantities which are of non-dimensional interest are the skin friction coefficient, local heat and mass diffusion flux rate the surface, which are given in terms of stream function as

$$\tau_w=\left(1+\frac{1}{\beta}\right)(\frac{\partial^2\psi}{\partial y^2}-\frac{\partial^2\psi}{\partial x^2})_{y=0},$$

$$q_w=-k\left(\frac{\partial T}{\partial y}\right)_{y=0}, q_m=-j\left(\frac{\partial C}{\partial y}\right)_{y=0}. \tag{2.39}$$

In dimensionless form above equations take the following form

$$\tau_w=\left(1+\frac{1}{\beta}\right)(xf''(0)+\gamma_1 h'(0))_{y=0},$$

$$q_w=-\theta'(0),\ q_m=-\phi'(0). \tag{2.40}$$

The position x_s of attachment of the dividing stream line is determined by the point of zero shear stress at the wall i.e. $\tau_w=0$, and is presented by

$$x_s=\frac{-\gamma_1 h'(0)}{f''(0)} \tag{2.41}$$

2.3 Solution by Optimal Homotopy analysis method

We now solve these nonlinear boundary value equations by the OHAM, and give an explicit formula for f, h, θ and φ. First of all, it is obvious that $f(y), h(y), \theta(y)$ and $\varphi(y)$ can be

articulated by a set of certain type of exponential base functions [55]

$$\{y^k \exp(-ny) \,|k \geq 0, n \geq 0\}, \tag{2.42}$$

in the forms

$$f(y) = a_{0,0}^0 + \sum_{n=0}^{\infty} \sum_{k=0}^{\infty} a_{m,n}^k \, y^k \exp(-ny), \tag{2.43}$$

$$h(y) = \sum_{n=0}^{\infty} \sum_{k=0}^{\infty} b_{m,n}^k \, y^k \exp(-ny), \tag{2.44}$$

$$\theta(y) = \sum_{n=0}^{\infty} \sum_{k=0}^{\infty} c_{m,n}^k \, y^k \exp(-ny), \tag{2.45}$$

$$\phi(y) = \sum_{n=0}^{\infty} \sum_{k=0}^{\infty} d_{m,n}^k \, y^k \exp(-ny), \tag{2.46}$$

in which $a_{m,n}^k, b_{m,n}^k, c_{m,n}^k$ and $d_{m,n}^k$ are series coefficients. By rule of the solution expressions along with the boundary conditions (2.30), the initial guesses f_0, h_0, θ_0 and ϕ_0 of $f(y), h(y), \theta(y)$and $\phi(y)$are selected as follow

$$f_0(y) = \frac{a}{c} y + \left(1 - \frac{a}{c}\right)(1 - \exp(-y)), \tag{2.47}$$

$$h_0(y) = y, \tag{2.48}$$

$$\theta_0(y) = \left(\frac{Bi}{1+Bi}\right)(\exp(-y)), \tag{2.49}$$

$$\phi_0(y) = \exp(-y). \tag{2.50}$$

We select the auxiliary linear operators as

$$L_f = \frac{d^3 f}{dy^3} - \frac{df}{dy}, \tag{2.51}$$

$$L_h = \frac{d^2 h}{dy^2} - h, \tag{2.52}$$

$$L_\theta = \frac{d^2 \theta}{dy^2} - \theta, \tag{2.53}$$

$$L_\phi = \frac{d^2 \phi}{dy^2} - \phi. \tag{2.54}$$

The linear operators in Eqs $(2.51)-(2.54)$ have the following properties

$$L_f\{C_1+C_2\exp(y)+C_3\exp(-y)\}=0, \quad (2.55)$$

$$L_h\{C_4\exp(y)+C_5\exp(-y)\}=0, \quad (2.56)$$

$$L_\theta\{C_6\exp(y)+C_7\exp(-y)\}=0, \quad (2.57)$$

$$L_\phi\{C_8\exp(y)+C_9\exp(-y)\}=0, \quad (2.58)$$

where C_i $(i=1-9)$ are the unknown constants.

The zeroth order homotopic deformation equations can be written as

$$(1-p)L_f\{\hat{f}(y;p)-f_0(y)\}=pc_0^f N_f\left(\hat{f}(y;p)\right), \quad (2.59)$$

$$(1-p)L_h\{\hat{h}(y;p)-h_0(y)\}=pc_0^h N_h\left(\hat{f}(y;p),\hat{h}(y;p)\right), \quad (2.60)$$

$$(1-p)L_\theta\{\hat{\theta}(y;p)-\theta_0(y)\}=pc_0^\theta N_\theta\left(\hat{f}(y;p),\hat{\theta}(y;p)\right), \quad (2.61)$$

$$(1-p)L_\phi\{\hat{\phi}(y;p)-\phi_0(y)\}=pc_0^\phi N_\phi\left(\hat{f}(y;p),\hat{\phi}(y;p)\right), \quad (2.62)$$

$$\hat{f}(0;p)=0,\hat{f}'(0;p)=0,\hat{h}(0;p)=0,\hat{\theta}'(0;p)=-Bi(1-\hat{\theta}(0;p)), \quad (2.63)$$

$$\hat{f}'(\infty;p)=0,\hat{h}'(\infty;p)=0,\hat{\theta}(\infty;p)=0,\hat{\phi}(0;p)=0,\hat{\phi}(\infty;p)=0, \quad (2.64)$$

where $p\,\epsilon\,[0,1]$ indicates the embedding parameter and c_0^f, c_0^h, c_0^θ and c_0^ϕ the nonzero auxiliary parameters. Moreover the nonlinear operators N_f, N_h, N_θ and N_ϕ are prescribed as

$$N_f\left(\hat{f}(y;p)\right)=\left(1+\frac{1}{\beta}\right)\frac{\partial^3\hat{f}(y;p)}{\partial y^3}+\hat{f}(y;p)\frac{\partial^2\hat{f}(y;p)}{\partial y^2}-\left(\frac{\partial\hat{f}(y;p)}{\partial y}\right)^2+\left(\frac{a}{c}\right)^2, \quad (2.65)$$

$$N_h\left(\hat{f}(y;p),\hat{h}(y;p)\right)=\left(1+\frac{1}{\beta}\right)\frac{\partial^2\hat{h}(y;p)}{\partial y^2}+\hat{f}(y;p)\frac{\partial\hat{h}(y;p)}{\partial y}-\frac{\partial\hat{f}(y;p)}{\partial y}\hat{h}(y;p)-A, \quad (2.66)$$

$$N_\theta\left(\hat{f}(y;p),\hat{\theta}(y;p)\right)=\frac{\partial^2\hat{\theta}(y;p)}{\partial y^2}+Pr(\hat{f}(y;p)\frac{\partial\hat{\theta}(y;p)}{\partial y}+N_b\frac{\partial\hat{\theta}(y;p)}{\partial y}\frac{\partial\hat{\phi}(y;p)}{\partial y}+N_t\left(\frac{\partial\hat{\theta}(y;p)}{\partial y}\right)^2), \quad (2.67)$$

$$N_\phi\left(\hat{f}(y;p),\hat{\phi}(y;p)\right)=\frac{\partial^2\hat{\phi}(y;p)}{\partial y^2}+Sc(\hat{f}(y;p)\frac{\partial\hat{\phi}(y;p)}{\partial y}+\frac{N_t}{N_b}\frac{\partial^2\hat{\theta}(y;p)}{\partial y^2}), \quad (2.68)$$

when p varies from 0 to 1, we have

$$\left.\begin{array}{c}\hat{f}(y;0)=f_0(y),\hat{f}(y;1)=f(y),\\ \hat{h}(y;0)=h_0(y),\hat{h}(y;1)=h(y),\\ \hat{\theta}(y;0)=\theta_0(y),\hat{\theta}(y;1)=\theta(y),\\ \hat{\phi}(y;0)=\phi_0(y),\hat{\phi}(y;1)=\phi(y),\end{array}\right\} \tag{2.69}$$

By means of Taylor's series

$$f_m(y)=\frac{1}{m!}\frac{\hat{f}(y;p)}{\partial y^m}\bigg|_{p=0},h_m(y)=\frac{1}{m!}\frac{\hat{h}(y;p)}{\partial y^m}\bigg|_{p=0},$$

$$\theta_m(y)=\frac{1}{m!}\frac{\hat{\theta}(y;p)}{\partial y^m}\bigg|_{p=0},\phi_m(y)=\frac{1}{m!}\frac{\hat{\phi}(y;p)}{\partial y^m}\bigg|_{p=0} \tag{2.70}$$

The auxiliary converging parameters are chosen in such fashion that the series (2.70) converges when $p=1$ thus we have

$$f(y)=f_0(y)+\sum_{m=1}^{\infty}f_m(y), \tag{2.71}$$

$$h(y)=h_0(y)+\sum_{m=1}^{\infty}h_m(y), \tag{2.72}$$

$$\theta(y)=\theta_0(y)+\sum_{m=1}^{\infty}\theta_m(y), \tag{2.73}$$

$$\phi(y)=\phi_0(y)+\sum_{m=1}^{\infty}\phi_m(y). \tag{2.74}$$

The resulting $mth-order$ deformation equations are

$$L_f\{f_m(y)-\chi_{m-1}f_{m-1}(y)\}=c_0^f R_m^f(y) \tag{2.75}$$

$$L_h\{h_m(y)-\chi_{m-1}h_{m-1}(y)\}=c_0^h R_m^h(y) \tag{2.76}$$

$$L_\theta\{\theta_m(y)-\chi_{m-1}\theta_{m-1}(y)\}=c_0^\theta R_m^\theta(y) \tag{2.77}$$

$$L_\phi\{\phi_m(y)-\chi_{m-1}\phi_{m-1}(y)\}=c_0^\phi R_m^\phi(y) \tag{2.78}$$

$$f_m(0) = 0,\ f'_m(0) = 0,\ f'_m(\infty) = 0,\ h_m(0) = 0,\ h'_m(\infty) = 0,$$

$$\theta'_m(0) = -Bi\big(1 - \theta_m(0)\big), \theta_m(\infty) = 0, \phi_m(0) = 0, \phi_m(\infty) = 0, \quad (2.79)$$

With the following definitions

$$R_m^f(y) = \left(1 + \frac{1}{\beta}\right) f'''_{m-1} + \sum_{k=0}^{m-1} f_k f''_{m-1-k} - \sum_{k=0}^{m-1} f'_k f'_{m-1-k} + \left(\frac{a}{c}\right)^2, \quad (2.80)$$

$$R_m^h(y) = \left(1 + \frac{1}{\beta}\right) h''_{m-1} + \sum_{k=0}^{m-1} f_k h'_{m-1-k} - \sum_{k=0}^{m-1} f'_k h_{m-1-k} - A, \quad (2.81)$$

$$R_m^\theta(y) = \theta''_{m-1} + Pr\Big(\sum_{k=0}^{m-1} f_k \theta'_{m-1-k} + Nb \sum_{k=0}^{m-1} \theta'_k \phi'_{m-1-k} + Nt \sum_{k=0}^{m-1} \theta'_k \theta'_{m-1-k}\Big), \quad (2.82)$$

$$R_m^\phi(y) = \phi''_{m-1} + Sc \sum_{k=0}^{m-1} f_k \phi'_{m-1-k} + \frac{Nt}{Nb}\, \theta''_{m-1}, \quad (2.83)$$

in which

$$\chi_m = \begin{cases} 0, m \le 1 \\ 1, m > 1 \end{cases} \quad (2.84)$$

The general solutions of Eqs $(2.75) - (2.78)$ can be written as

$$f_m(y) = f_m^*(y) + C_1 + C_2 \exp(y) + C_3 \exp(-y), \quad (2.85)$$

$$h_m(y) = h_m^*(y) + C_4 \exp(y) + C_5 \exp(-y), \quad (2.86)$$

$$\theta_m(y) = \theta_m^*(y) + C_6 \exp(y) + C_7 \exp(-y), \quad (2.87)$$

$$\phi_m(y) = \phi_m^*(y) + C_8 \exp(y) + C_9 \exp(-y), \quad (2.88)$$

in which $f_m^*(y), h_m^*(y), \theta_m^*(y)$ and $\phi_m^*(y)$ are the particular solutions of the Eqs$(2.85) - (2.88)$. Note that Eqs. $(2.75) - (2.78)$ Can be solved by Mathematica one after the other in the order $m = 1,2,3, \ldots$

2.4 Optimal convergence-control parameters

We know that our series solutions $(2.71) - (2.74)$ strongly depend upon the auxiliary parameters c_0^f, c_0^h, c_0^θ and c_0^ϕ which govern the convergence region and the Homotopy solutions in terms of series. To find out the optimal values of c_0^f, c_0^h, c_0^θ and c_0^ϕ we have utilized the idea of average residual error given by [58].

$$E_m^f = \frac{1}{k+1}\sum_{j=0}^{k}\{N_f\,(\sum_{i=0}^{m}\hat{f}(y))_{y=j\delta y}\}^2 dy, \tag{2.89}$$

$$E_m^h = \frac{1}{k+1}\sum_{j=0}^{k}\{N_h\,(\sum_{i=0}^{m}\hat{f}(y), \sum_{i=0}^{m}\hat{h}(y))_{y=j\delta y}\}^2 dy, \tag{2.90}$$

$$E_m^\theta = \frac{1}{k+1}\sum_{j=0}^{k}\{N_\theta\,(\sum_{i=0}^{m}\hat{f}(y), \sum_{i=0}^{m}\hat{\theta}(y))_{y=j\delta y}\}^2 dy, \tag{2.91}$$

$$E_m^\phi = \frac{1}{k+1}\sum_{j=0}^{k}\{N_\phi\,(\sum_{i=0}^{m}\hat{f}(y), \sum_{i=0}^{m}\hat{\phi}(y))_{y=j\delta y}\}^2 dy. \tag{2.92}$$

Following Liao [58]

$$E_m^t = E_m^f + E_m^h + E_m^\theta + E_m^\phi \tag{2.93}$$

where E_m^t is the total squared residual error, $\delta y = 0.5, k = 20$. we have considered a case where $Nt = 0.2, Nb = 0.5, Pr = 1.0 = Sc, \frac{a}{c} = 0.1 = Bi$. Total average squared residual error is

minimized by using Mathematica package $\boldsymbol{BVPh\ 2.0}$ which can be found at http://numericaltank.sjtu.edu.cn/BVPh2_0.htm. We have directly applied the command **Minimize** to obtain the corresponding local optimal convergence control parameters. $Tables$ 2.1 and 2.2 are prepared for the case of several optimal convergence control parameters. $Table$ 2.1 shows the minimum value of total averaged squared residual error, while $Tables$ 2.2 shows the individual average squared residual error at different orders of approximations using the optimal values from $Tables$ 2.1 at $m = 8$. It can be clearly seen that the averaged squared residual errors and total averaged squared residual errors continuously decreases as we increase the higher order approximation. Therefore, Optimal Homotopy Analysis Method gives absolute freedom to pick any set of local convergence control parameters to obtain convergent results.

m	c_0^f	c_0^h	c_0^θ	c_0^ϕ	E_m^t	CPU TIME[S]
2.0	-1.22	-1.05	-1.31	-1.10	2.83×10^{-4}	4.55
4.0	-1.30	-0.93	-1.37	-1.05	1.18×10^{-5}	27.75
6.0	-1.34	-1.09	-1.40	-0.96	2.23×10^{-6}	103.64
8.0	-0.67	-0.91	-1.42	-0.89	7.30×10^{-7}	370.79

$Table$ 2.1**:** Total Averaged squared residual errors using $\boldsymbol{BVPh2.0}$

m	E_m^f	E_m^h	E_m^θ	E_m^ϕ	CPU TIME[S]
2.0	2.83×10^{-6}	7.45×10^{-4}	7.84×10^{-6}	1.21×10^{-4}	1.06
8.0	2.56×10^{-10}	7.24×10^{-7}	1.61×10^{-9}	3.05×10^{-9}	17.70
12	3.23×10^{-12}	1.25×10^{-7}	3.83×10^{-10}	8.36×10^{-6}	59.87
16	9.33×10^{-14}	3.42×10^{-8}	1.02×10^{-9}	4.61×10^{-10}	147.29

20	4.56×10^{-15}	1.90×10^{-8}	9.22×10^{-9}	1.95×10^{-9}	299.0

Table 2.2**:** Individual Averaged squared residual errors using optimal values at $\boldsymbol{m = 8}$ from *Table* 2.1.

2.5 Results and discussion

The main objective here is to study the variations of emerging non-dimensional parameters of nano Casson fluid model. To provide a non-dimensional intuition into our flow governing equations, *Figs*. (2.2) to (2.21) are plotted for the velocity field, temperature field, concentration and the stream lines. *Fig*. (2.2) shows the velocity $f'(y)$when $\beta = 1$ and different values of a/c while *Fig*. (2.3) shows $f'(y)$for $\frac{a}{c} = 0.4$ and various values of β. It is noticed from *Fig* (2.2) that velocity increases as the stretching ratio a/c is increased and corresponding boundary layer is found to be inverted. Further, it is quite obvious from Fig. (2.2) that when $a/c < 1$, the flow has an inverted boundary layer structure. This results in from the fact that when $a/c < 1$, the stretching velocity cx of the surface exceeds the stagnation velocity ax of the external stream. *Fig*. (2.3) exhibits that when $\frac{a}{c} < 1$; velocity $f'(y)$ decreases with an increase in β. *Figs* (2.4) and (2.5) depict the variation of $\frac{a}{c}$ on $h'(y)$for fix β and vice versa. These figures show that initially $h'(y)$increases and after $y = 1$, $h'(y)$ decrease with an increase in $\frac{a}{c}$ and β (*See Figs* (2.4)*and Fig* (2.5)). Variation of arising non-dimensional parameters such as $\frac{a}{c}, \beta, Pr, Sc, Nt, Nb$ and Bi on the temperature profile $\theta(y)$is discussed in *Figs*. (2.6) − (2.12). It can be clearly seen from *Figs*. (2.6) *and* (2.7) that temperature $\theta(y)$ decreases with

higher values of $\frac{a}{c}$ and it increases with an increase in β. From $Fig.(2.8)$ we have found that as we increase the Prandtl number Pr, temperature profiles $\theta(y)$ and thickness of the thermal boundary layer tends to decrease which consequently increases the local heat flux. $Figs\ (2.9)\ to\ (2.12)$ show that with the increase of Schmidt number Sc, Brownian motion Nb, thermophoresis parameter Nt and Biot number Bi, the temperature profile $\theta(y)$ also increases. The effects of non-dimensional parameters Bi, $\frac{a}{c}$, β, Nt, Nb and Schmidt number Sc on concentration profile $\phi(y)$ are expressed in $Figs.(2.13)\ to\ (2.18)$. These figures suggest that concentration profile $\phi(y)$increases with an increases in $Bi, \beta$and Nt. However, it decreases for the case of $\frac{a}{c}$, Sc and Nb. The stream line patterns for the oblique flows are shown in $Figs.(2.19)\ to\ (2.21)$. The stream line $\psi = 0$ meets the wall $y = 0$, at $x = x_0$, where x_0 is the point of stagnation and zero skin friction. It can be noticed from these figures that the stagnation point is at the left of the origin for positive values of $\gamma_1 \neq 0$ whereas it is on the right of the origin for negative values of $\gamma_1 \neq 0$. The shifting of x_0 depends upon the magnitude of $\gamma_1 \neq 0$.

$Tables\ 2.3 - 2.6$ are presented for the numerical values of the skin friction coefficients, local heat flux and local mass flux for different non-dimensional parameters of interest. From $Table\ 2.3$ it can be observed that our computed resulted are in very good agreement with the available published literature. From $Table\ 2.4$ it is noticed that magnitude of normal skin friction coefficient $f''(0)$ decreases with an increase in a/c whereas the tangential skin friction component $h'(0)$ tends to increase with increasing $\frac{a}{c}$. It can be seen from $Table\ 2.4$ that when $\frac{a}{c} < 1$, magnitude of $f''(0)$ decreases with increasing $\frac{a}{c}$ for fixed β considered. But when $\frac{a}{c} > 1$, $f''(0)$ increases with increasing $\frac{a}{c}$ which is consistent with the fact that there is progressive thinning of the momentum boundary layer with increase in $\frac{a}{c}$. $Table\ 2.5$ is prepared to study the

influence of non-Newtonian Casson parameter β on skin frictions and local heat and mass flux at the stretching convective surface. We find out that when β is increased both normal and tangential components of the skin friction also increases, on the other hand it has quite contrary influence on the local heat and mass flux i.e. it causes to reduce the local heat and mass flux. $Table$ 2.6 is prepared to examine the influence of Bi, Nt, Nb, Pr and Sc for some fix values of a/c and β on the local heat flux respectively. It is obvious from these tables that the magnitude of $-\theta'(0)$ increases for large values of Pr and Bi because heat flows from surface towards the fluid providing $T_f > T_\infty$. It has been found that heat flux at the surface $-\theta'(0)$ decreases for large values of Sc, Nt and Nb. It can be seen that effects of the parameters Nb and Sc on the local mass flux are positive i.e. they causes an increase in the local mass flux. Finally we find out that Prandtl number Pr, thermophoresis parameter Nt and Biot number Bi causes a decrease in local mass flux when its values are increased.

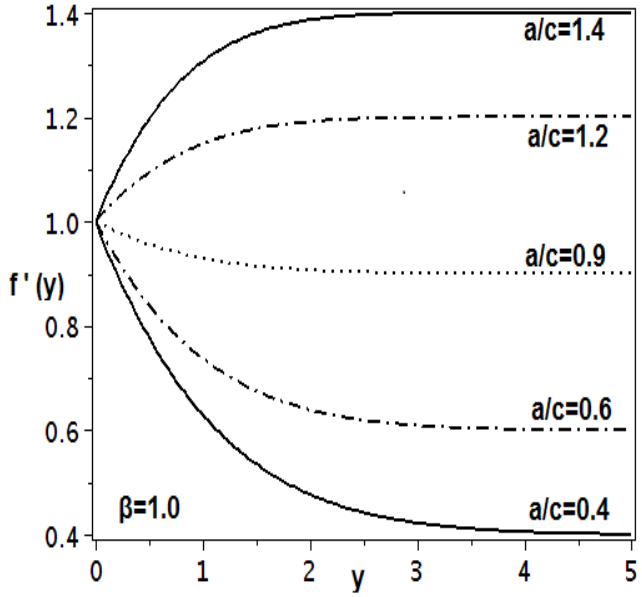

$Fig(2.2)$ Velocity profile $f'(y)$ against a/c when $\beta = 1$.

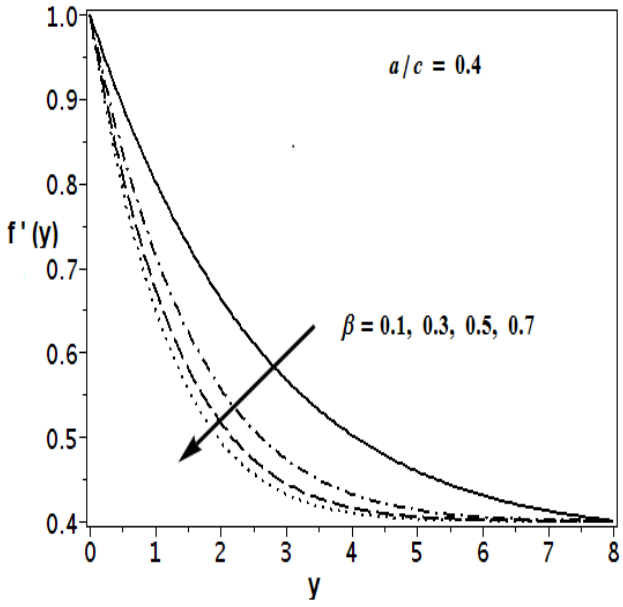

Fig (2.3) Velocity profile $f'(y)$ against β when a$/c$ $=$ 0.4.

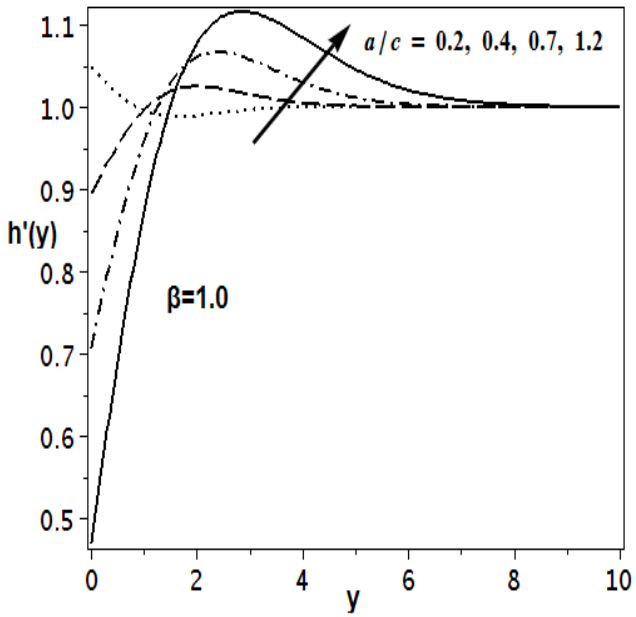

$Fig(2.4)$ Velocity profile $h'(y)$ against a/c when $\beta = 1$.

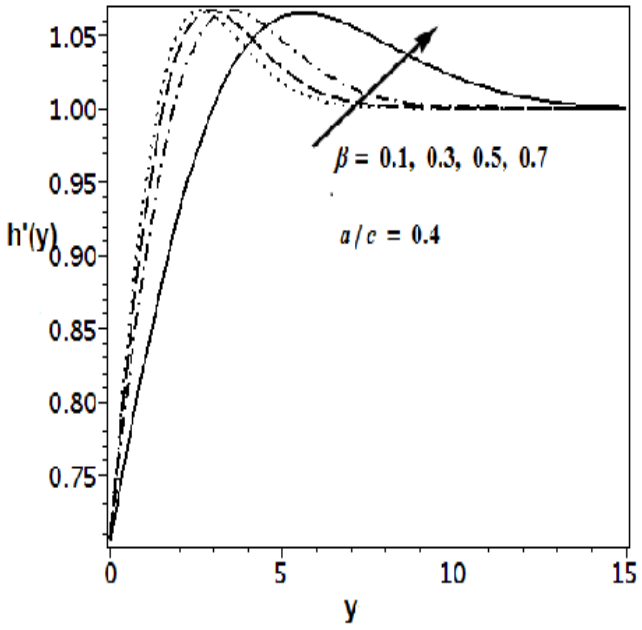

Fig (2.5) Velocity profile $h'(y)$ against β when a$/c = 0.4$.

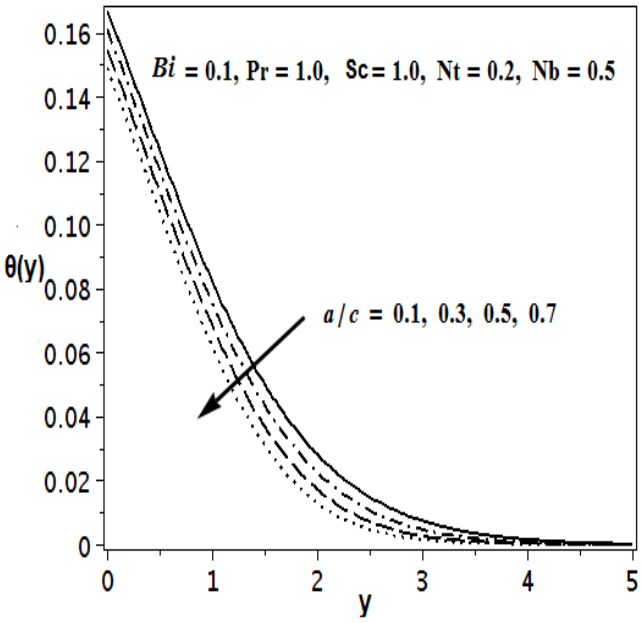

Fig (2.6) Temperature profile $\theta(y)$ against a/c.

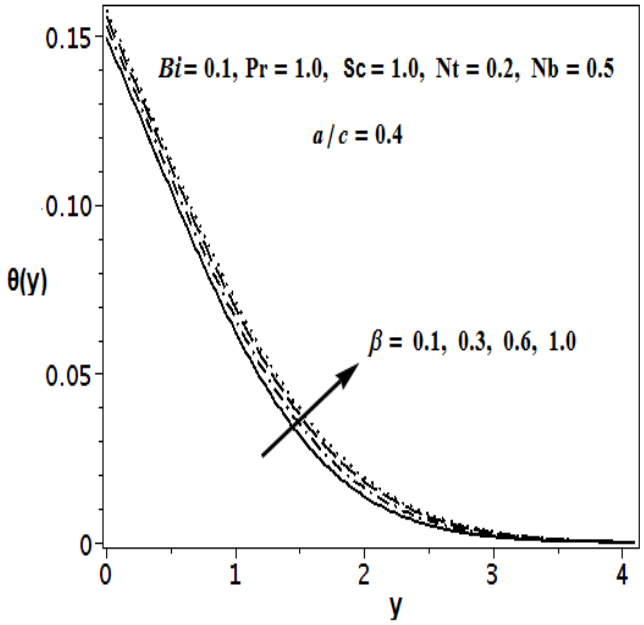

Fig (2.7) Temperature profile $\theta(y)$ against β.

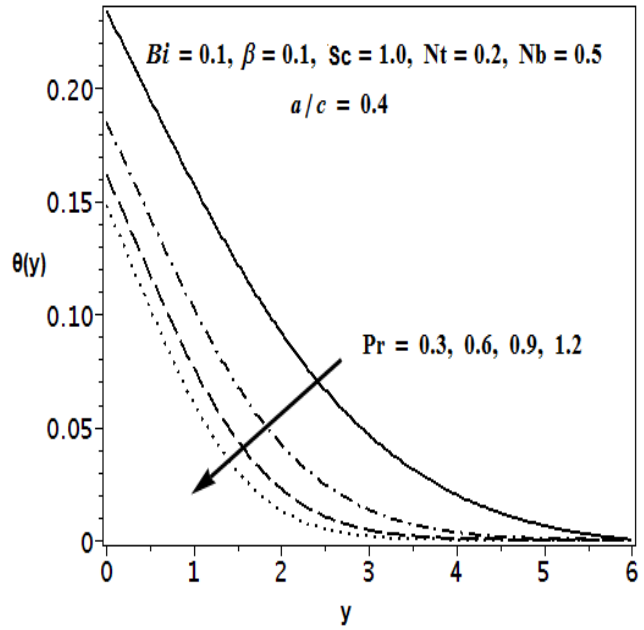

Fig (2.8) Temperature profile $\theta(y)$ against Pr.

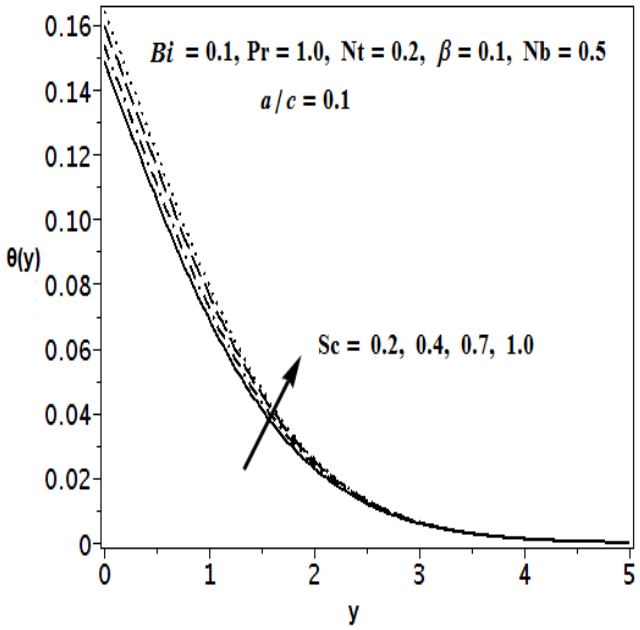

Fig (2.9) Temperature profile $\theta(y)$ against Sc.

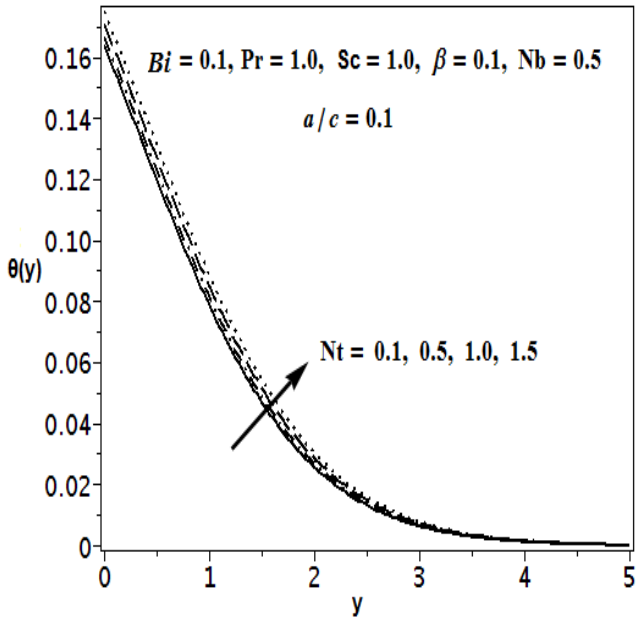

Fig (2.10) Temperature profile $\theta(y)$ against Nt.

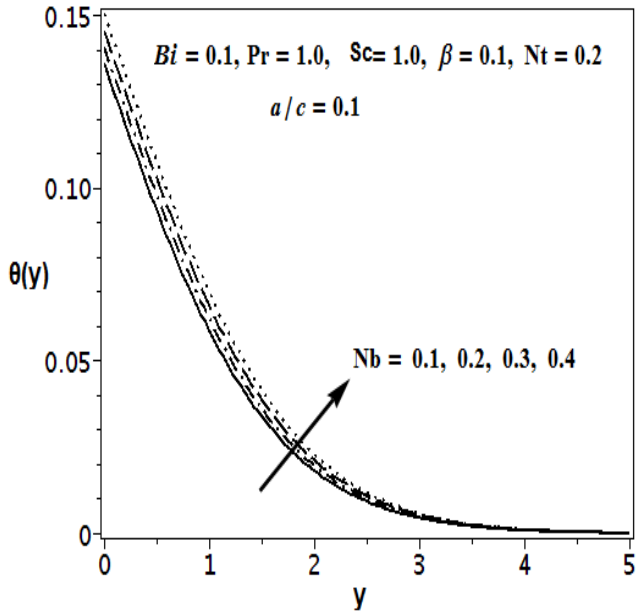

Fig (2.11) Temperature profile $\theta(y)$ against Nb.

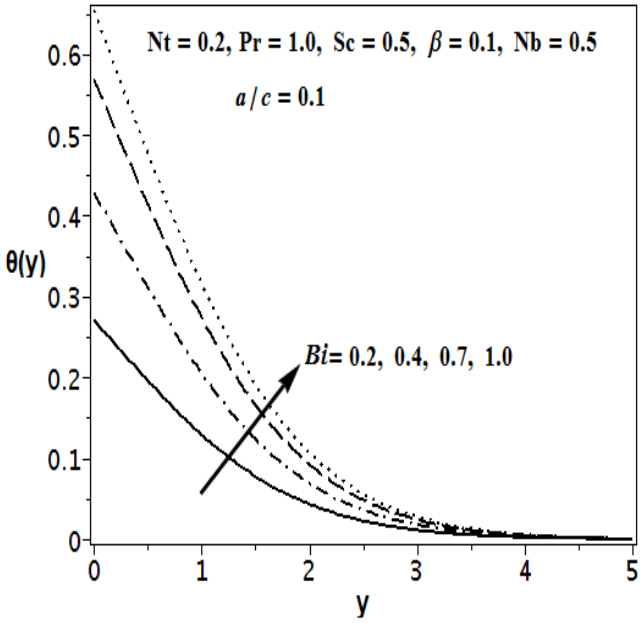

Fig (2.12) Temperature profile $\theta(y)$ against Bi.

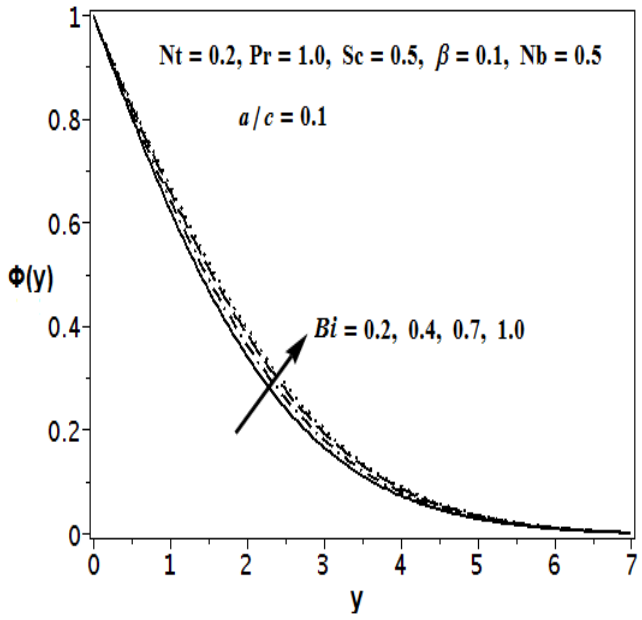

Fig (2.13) Concentration profile $\phi(y)$ against Bi.

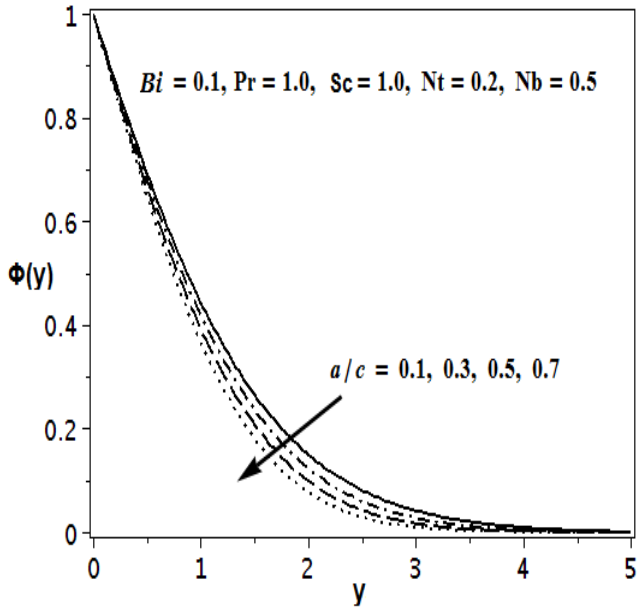

Fig (2.14) Concentration profile $\phi(y)$ against a/c.

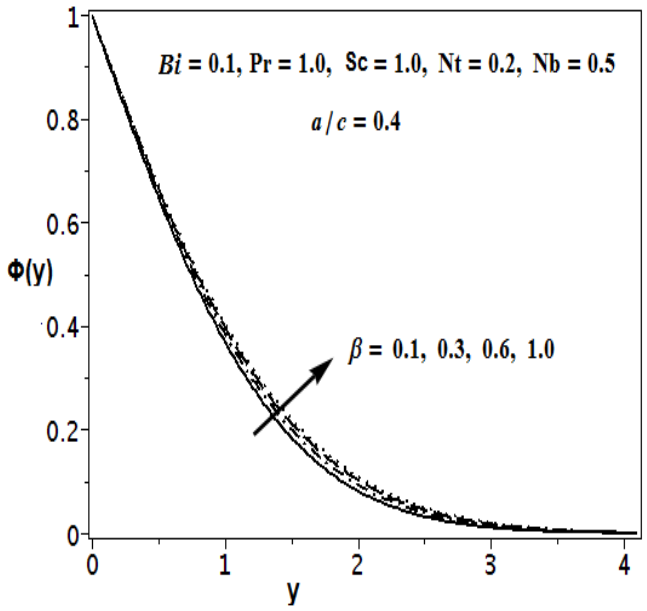

Fig (2.15) Concentration profile $\phi(y)$ against β.

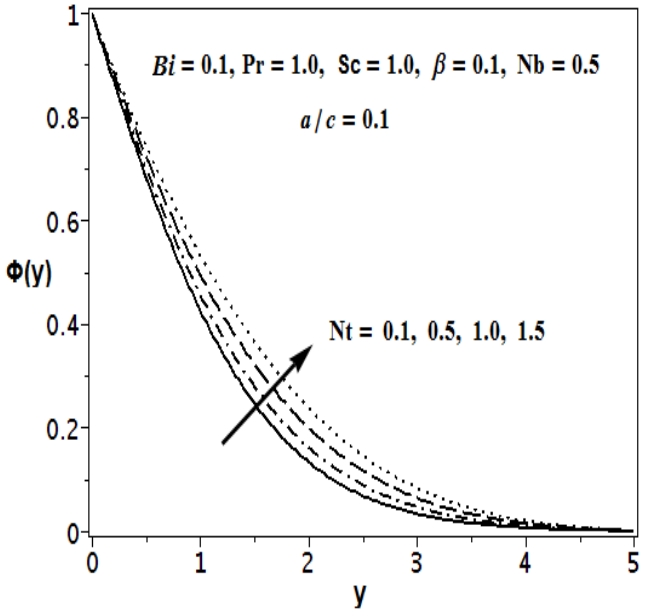

Fig (2.16) Concentration profile $\phi(y)$ against Nt.

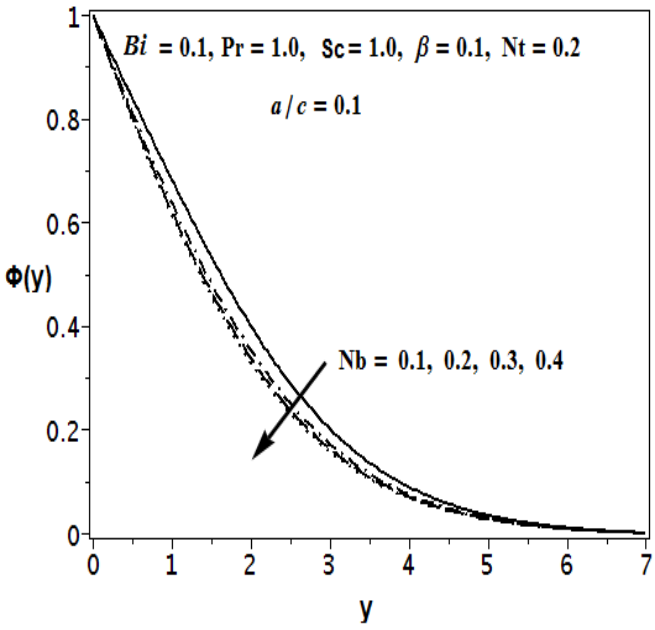

Fig (2.17) Concentration profile $\phi(y)$ against Nb.

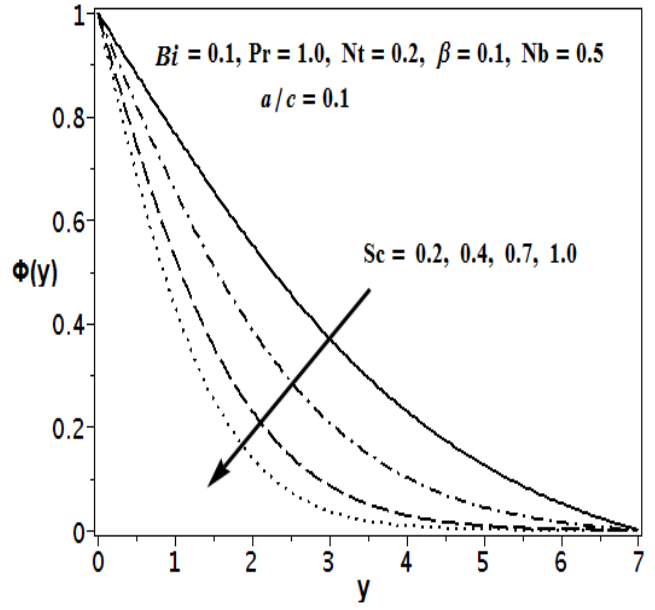

Fig (2.18) Concentration profile $\phi(y)$ against Sc.

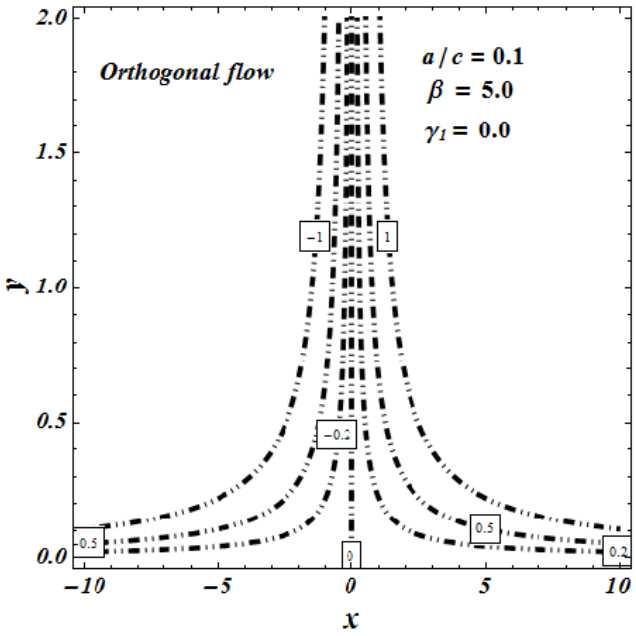

Fig (2.19) Stream line patterns for $\gamma 1 = 0$.

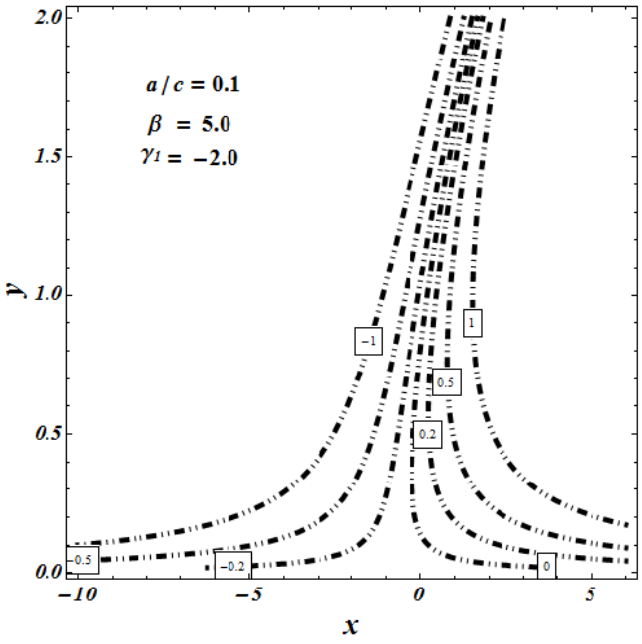

Fig (2.20) Stream line patterns for $\gamma 1 = -2$.

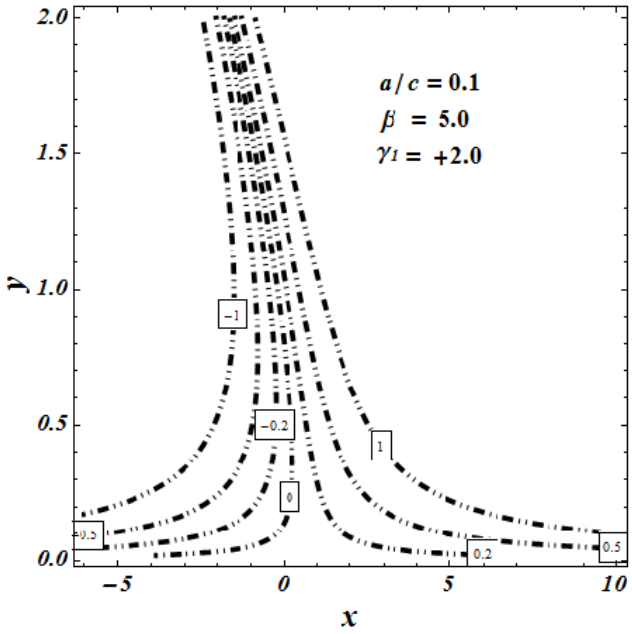

Fig (2.21) Stream line patterns for $\gamma 1 = +2$.

	$f''(0)$			$h'(0)$	
a/c	Present	Mahapatra [7]	Pop et al [14]	Present	Pop et al [14]
0.1	−0.96938	−0.9694	−0.96938	0.26341	0.26278
0.3	−0.84937		−0.84942	0.60631	0.60573
0.8	−0.29937		−0.29938	0.93472	0.93430
1.0	0.0		0.0	1.0	1.0
2.0	2.01750	2.01750	2.01750	1.16522	1.16489
3.0	4.72928	4.72930	4.72928	1.23465	1.23438

Table 2.3: Comparison with the existing literature for the limiting case

a/c	A	$f''(0)$	$h'(0)$	$-\theta'(0)$	$-\Phi'(0)$
0.1	0.867270	−0.884924	0.263417	0.239587	0.563735
0.3	0.569082	−0.775410	0.606316	0.247381	0.608679
0.7	0.196183	−0.395707	0.893288	0.262177	0.695940
1.0	0.0	0.0	1.0	0.271747	0.756380
1.3	−0.159267	0.474671	1.069512	0.280130	0.812869
1.5	−0.251620	0.830283	1.103882	0.285162	0.848616
1.9	−0.413036	1.626260	1.155037	0.294123	0.916195

Table 2.4**:** Numerical values of non-dimensional quantities when

$\beta = 5.0, Nt = 0.2, Nb = 0.5, Sc = 1.0 = Pr, Bi = 0.5.$

β	A	$-f''(0)$	$h'(0)$	$-\theta'(0)$	$-\Phi'(0)$
0.1	2.580922	0.292572	0.150654	0.261612	0.689570
0.3	1.647167	0.465684	0.252042	0.255266	0.650509
0.7	1.233767	0.622044	0.262946	0.249402	0.616403
1.0	1.196380	0.685459	0.263310	0.247015	0.603082
2.0	0.969637	0.791500	0.263410	0.243043	0.581644
3.0	0.914183	0.839513	0.263415	0.241260	0.572320
5.0	0.867270	0.884924	0.263417	0.239587	0.563735

Table 2.5**:** Numerical values of non-dimensional quantities when

$a/c = 0.1, Nt = 0.2, Nb = 0.5, Sc = 1.0 = Pr, Bi = 0.5.$

Bi	Nt	Nb	Pr	Sc	$-\theta'(0)$	$-\Phi'(0)$
0.1	0.2	0.5	1.0	1.0	0.082464	0.598529
0.3					0.182166	0.576375
0.5					0.239587	0.563735
0.1	0.2	0.5	1.0	1.0	0.082464	0.598529
	0.4				0.082298	0.580260
	0.6				0.082128	0.562244
0.1	0.2	0.1	1.0	1.0	0.085324	0.511991
		0.3			0.083968	0.584022
		0.5			0.082464	0.598529
0.1	0.2	0.5	1.0	1.0	0.082464	0.598529
			2.0		0.086120	0.596686
			4.0		0.088212	0.595771
0.1	0.2	0.5	1.0	1.0	0.082464	0.598529
				2.0	0.081463	0.928921
				3.0	0.080948	1.184097

Table 2.6**:** Numerical values of non-dimensional quantities when $\frac{a}{c} = 0.1, \beta = 5.0$.

2.6 Conclusions

Oblique flow of a Casson nano fluid is examined on a convective stretched surface. An efficient analytical technique OHAM (*BVPh* 2.0) is utilized to calculate the residual errors of the governing system of equations. Influence of the flow governing parameters is examined through

graphs and Tables. Following conclusions can be drawn from this study:

- Heat transfer rate is increasing function of stretching parameter, Prandtl number, Biot number and it decreases with an increase in Brownian motion, non-Newtonian (Casson) parameter and thermophoresis.
- Nanoparticle concentration is increasing function of stretching parameter and Brownian motion while it is decreasing function of thermophoresis, Biot number and non-Newtonian (Casson) parameter.
- Nano fluids can be used as an efficient agent to control the heat transfer rate at the stretching surface.

Chapter 3

Combined effects of magnetic field and partial slip on obliquely striking rheological fluid over a stretching surface

3.1 Introduction

This chapter explores the combined effects of transversely applied uniform magnetic field and partial slip on an oblique flow of a rheological fluid over stretched convective surface. The prevailing momentum equations are designed by manipulating Casson fluid model. By applying the suitable similarity transformations, the governing system of equations are transformed into coupled nonlinear ordinary differential equations. The resulting system is handled numerically through midpoint integration scheme together with Richardson's extrapolation. Streamlines pattern are presented to study the actual impact of slip mechanism and magnetic field on the oblique flow. A suitable comparison with the previous literature is provided to confirm the accuracy of present study for the limiting case.

3.2 Mathematical Formulation

Consider a 2D steady flow of a MHD Casson fluid which meets a stretched convective surface in a non-aligned manner. Surface is stretched along the $x-axis$ while $y-axis$ taken normal to

surface. A uniformly applied magnetic field B_0 is imposed along $y-axis$, which is normal to the surface as given in Fig (3.1). Due to small magnetic Reynolds number the effects of induced magnetic field are negligible and no electric field is considered. The constitutive equations for the Casson fluid model are same as in Chapter 2.

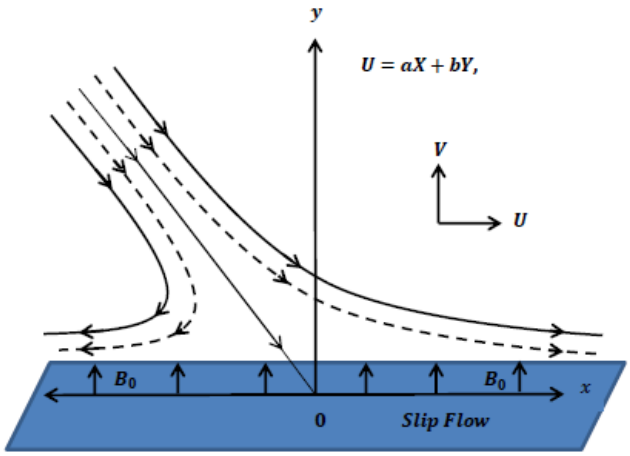

Fig (3.1) Non-dimensional description of the problem

The governing flow equations for the MHD Casson fluid model can be stated as

$$\frac{\partial u^*}{\partial x^*}+\frac{\partial v^*}{\partial y^*}=0 \tag{3.1}$$

$$u^*\frac{\partial u^*}{\partial x^*}+v^*\frac{\partial u^*}{\partial y^*}+\frac{1}{\rho}\frac{\partial p^*}{\partial x^*}=\nu\left(1+\frac{1}{\beta}\right)\nabla^{*2}u^*-\frac{\sigma}{\rho}B_0^2u^* \tag{3.2}$$

$$u^*\frac{\partial v^*}{\partial x^*}+v^*\frac{\partial v^*}{\partial y^*}+\frac{1}{\rho}\frac{\partial p^*}{\partial y^*}=\nu(1+\frac{1}{\beta})\nabla^{*2}v^* \tag{3.3}$$

where u^* and v^* are components of velocity along x and $y-axis$ respectively, ν is the effective kinematic viscosity and $\beta = \mu_B \frac{\sqrt{2\pi_c}}{p_y}$ is the Casson fluid parameter. The appropriate conditions at the surface with slip are [37].

$$u^* = cx^* + N\mu_B\left(1+\frac{1}{\beta}\right)\left(\frac{\partial u^*}{\partial y^*}+\frac{\partial v^*}{\partial x^*}\right), \quad at\ y^* = 0,$$

$$u^* = ax^* + by^*\ as\ y^* \to \infty \tag{3.4}$$

in which a, b and c are all positive constants with dimensions of inverse time and N is a slip constant.

By applying the similarity transformations

$$x = x^*\sqrt{\frac{c}{\nu}}, y = y^*\sqrt{\frac{c}{\nu}}, u = \frac{1}{\sqrt{\nu c}}u^*,$$

$$v = \tfrac{1}{\sqrt{\nu c}}v^*, p = \tfrac{1}{\sqrt{\mu c}}p^*. \tag{3.5}$$

Making use of Eq (3.5) in Eqs (3.1) – (3.4), we have

$$\frac{\partial u}{\partial x}+\frac{\partial v}{\partial y} = 0 \tag{3.6}$$

$$u\frac{\partial u}{\partial x}+v\frac{\partial u}{\partial y}+\frac{\partial p}{\partial x} = \left(1+\tfrac{1}{\beta}\right)\nabla^2 u - M^2 u \tag{3.7}$$

$$u\frac{\partial v}{\partial x}+v\frac{\partial v}{\partial y}+\frac{\partial p}{\partial y} = (1+\tfrac{1}{\beta})\nabla^2 v \tag{3.8}$$

where $M = B_0\sqrt{\frac{\sigma}{\rho c}}$ is the Hartman number.

Introducing stream function in the form

$$u = \frac{\partial \psi}{\partial y}, v = -\frac{\partial \psi}{\partial x}. \tag{3.9}$$

Eq (3.6) is identically satisfied while (3.7) − (3.8) can be written in terms of stream function as

$$\left(1+\frac{1}{\beta}\right)\nabla^4\psi+\frac{\partial(\psi,\nabla^2\psi)}{\partial(x,y)}-M^2\frac{\partial\psi}{\partial y}=0. \qquad (3.10)$$

Redefining the stream function in Eq (3.10) as [14]

$$\psi(x,y)=xf(y)+g(y). \qquad (3.11)$$

We get

$$\left(1+\frac{1}{\beta}\right)f'''+ff''-f'^2-M^2f'+C_1=0, \qquad (3.12)$$

$$\left(1+\frac{1}{\beta}\right)g'''+fg''-f'g'-M^2g'+C_2=0. \qquad (3.13)$$

Along with transformed boundary conditions

$$f(0)=0, f'(0)=1+\left(1+\frac{1}{\beta}\right)\omega f''(0), f'(\infty)=\frac{a}{c},$$

$$g(0)=0, g'(0)=\left(1+\frac{1}{\beta}\right)\omega g''(0), g''(\infty)=\frac{b}{c}=\gamma_1, \qquad (3.14)$$

where C_1 and C_2 are integral constants to be determined and $\omega=N\rho\sqrt{cv}$ the slip parameter, Since $f(y)=(\frac{a}{c})y+A$ at $y\to\infty$ in which A signifies the boundary layer displacement constant, by substituting Eq (3.14) in Eqs. (3.12) and (3.13), we get $C_1=M^2(\frac{a}{c})+(\frac{a}{c})^2$ and $C_2=-A\gamma_1$.

Introducing

$$g'(y)=\gamma_1 h(y). \qquad (3.15)$$

Eqs (3.12) to (3.14) take the form as

$$\left(1+\frac{1}{\beta}\right)f'''+ff''-f'^2+M^2(\left(\frac{a}{c}\right)-f')+(\frac{a}{c})^2=0, \qquad (3.16)$$

$$\left(1+\frac{1}{\beta}\right)h''-f'h+fh'-M^2h-A=0, \qquad (3.17)$$

$$f(0)=0,\quad f'(0)=1+\left(1+\frac{1}{\beta}\right)\omega f''(0),$$

$$f'(\infty) = \frac{a}{c},\ h(0) = \left(1 + \frac{1}{\beta}\right)\omega h'(0),\ h'(\infty) = 1. \qquad (3.18)$$

Shear stress at the stretching wall in non-dimensional form can be given as

$$\tau_w = \left(1 + \frac{1}{\beta}\right)(xf''(0) + \gamma_1 h'(0))_{y=0}. \qquad (3.19)$$

The point of stagnation x_s can be attained by zero wall shear stress, i.e.

$$x_s = \frac{-\gamma_1 h'(0)}{f''(0)} \qquad (3.20)$$

where γ_1 control the obliqueness of the flow.

3.3 Numerical Solution

The governing system of Eqs (3.16) to (3.18) are coupled and nonlinear in nature which are solved numerically using highly efficient computational software Maple. Maple uses a combination of midpoint integration as a basic scheme and Richardson's extrapolation as an enhancement scheme, as introduced in $[65 - 66]$. This procedure involves a highly stable computational process which cultivates vastly precise grid independent solutions. The scheme works by initially transforming the governing nonlinear higher order equations to a set of first order differential equations. The semi-infinite domain $[0, \infty)$ is then replaced with a proper finite domain of y i.e. $[0, y_\infty)$ where y_∞ is so properly chosen that the numerical solutions would approach the asymptotic behaviour at infinity. A mesh size of $\Delta h = 0.001$ has been supposed, which is good enough to achieve convergence condition of 10^{-6} in almost all computations. Our computed numerical results are compared with the existing published literature in order to certify the precision of current numerical scheme and are found in decent agreement.

3.4 Results and Discussion

This section helps us to explore the flow behaviour against certain non-dimensional parameters of interest. $Figs.\,(3.2) - (3.13)$ are deliberated to express the velocities and streamline patterns for several values of the presiding parameters. $Figs.\,(3.2) - (3.5)$ are plotted to find out the influence of stretching ratio $\frac{a}{c}$, Casson fluid parameter β, slip parameter ω and magnetic field parameter M on normal velocity component $f'(y)$. It is noticeable from $Fig\ (3.2)$ that normal velocity profile $f'(y)$ rises with increasing stretching ratio $\frac{a}{c}$ and it depicts an inverted boundary layer behaviour when $\frac{a}{c} > 1$. From $Fig\ (3.3)$ it is manifested that as Casson fluid parameter β is increasing; normal velocity $f'(y)$ drops away from the wall. The behaviour of $f'(y)$ against slip parameter ω is revealed through $Fig\ (3.4)$. It is evident from this figure that normal velocity $f'(y)$ is inversely related with slip parameter ω, i.e. it causes the velocity profile $f'(y)$ to decrease near the wall. $Fig\ (3.5)$ illustrates the influence of M on normal velocity profile $f'(y)$. It is found that in the presence of partial slip, magnetic field parameter M causes a reduction in the normal velocity $f'(y)$. This is because of the fact that application of magnetic field produces lorentz force which causes a resistance within the fluid and hence decreases the normal fluid velocity. On the other hand, it is quite obvious from $Figs\ (3.6)$ and (3.7) that tangential velocity profile $h'(y)$ rises with stretching ratio $\frac{a}{c}$ and Casson fluid parameter β for fixed values of partial slip parameter ω and magnetic field parameter M. It would be obligatory to mention here that this growth in the tangential velocity profile $h'(y)$ is visible near the stretching wall. Tangential velocity profile $h'(y)$ is seemed to be decreasing with an increase in

slip parameter ω and magnetic field parameter M (see $Figs$ (3.8) and (3.9)). In order to observe the actual flow behaviour in the presence of partial slip and transversely applied magnetic field, streamline patterns are sketched through $Figs$ (3.10) $-$ (3.13) for positive as well as negative shear in the flow. It is quite apparent from these graphics that the slip parameter ω and magnetic field parameter M cause a disturbance in the obliqueness of the flow. However, the effects are more conspicuous in the presence of magnetic field (see $Figs$ (3.12) and (3.13)). Moreover it is also noticed that the location of point of stagnation x_s is shifted for slip flow with transversely applied magnetic field. Numerical values of local skin friction coefficients are presented in $Tables$ 3.1 and 3.2. $Table$ 3.1 offers a suitable agreement of current study with the existing literature for the limiting case, i.e. in the absence of magnetic field and partial slip when $\beta \to \infty$. Numerical values of normal and tangential skin friction components against certain non-dimensional parameters are presented in $Table$ 3.2. It is found that stretching ratio a/c leads to a decline in both types of skin friction coefficients. Increasing the magnetic field parameter M has opposite influence on normal and tangential skin frictions. On a similar note it is also found that slip parameter ω reduces the skin friction coefficients and increase in Casson fluid parameter β causes an increase in both types of skin friction coefficients.

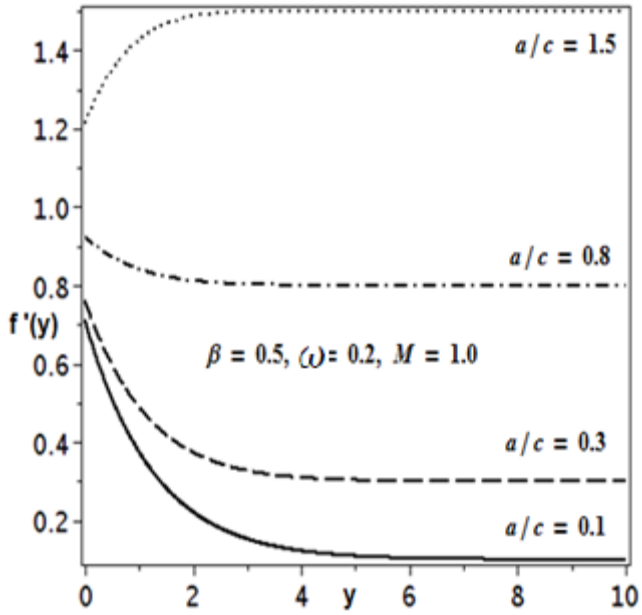

Fig (3.2) Velocity profile $f'(y)$ against a/c.

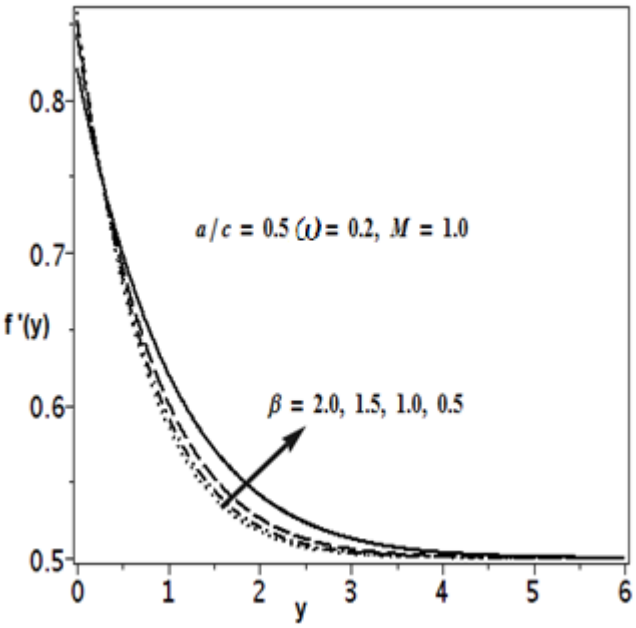

Fig (3.3) Velocity profile $f'(y)$ against β.

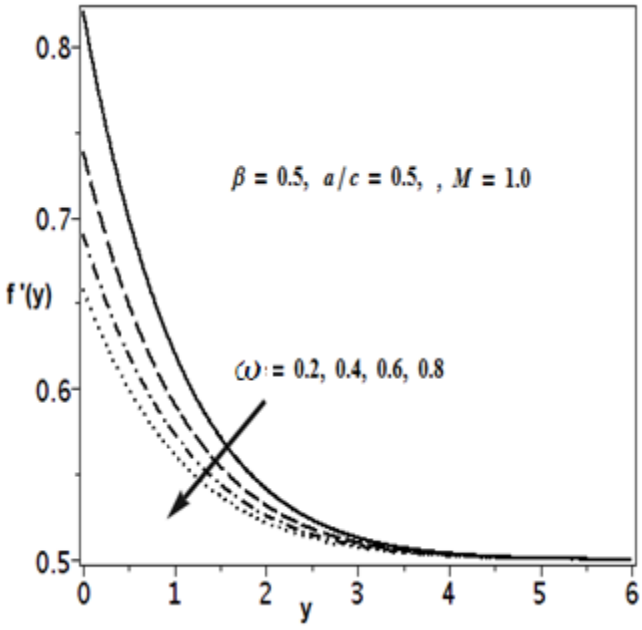

Fig (3.4) Velocity profile $f'(y)$ against ω.

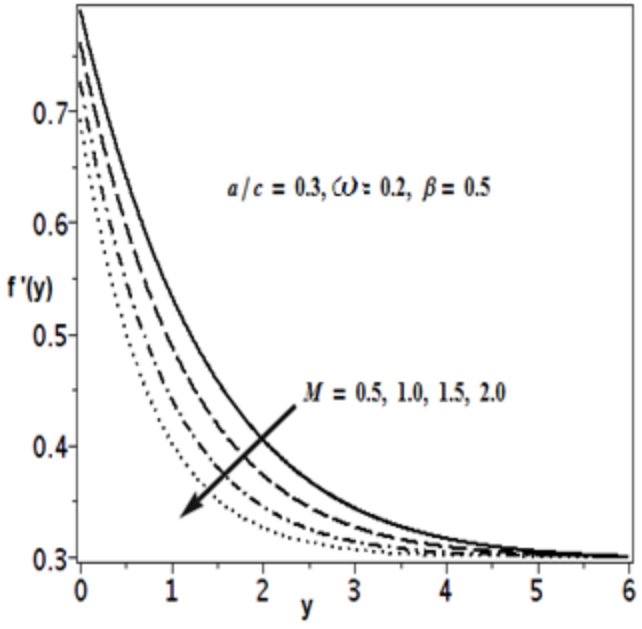

Fig (3.5) Velocity profile $f'(y)$ against M.

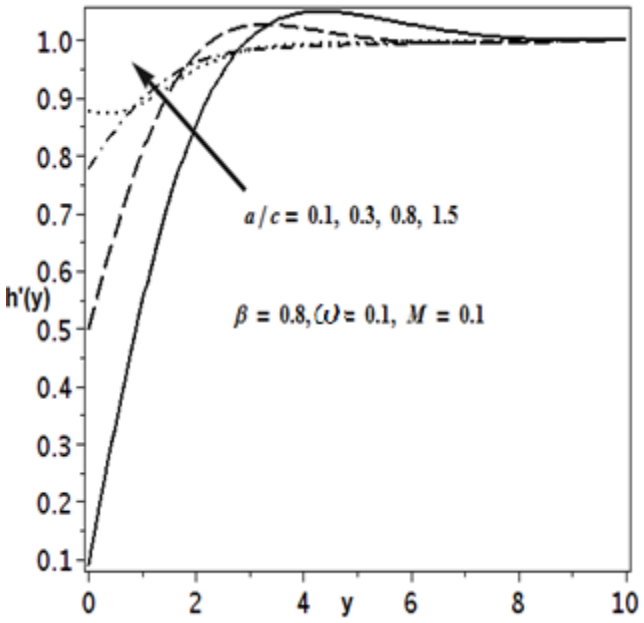

Fig (3.6) Velocity profile $h'(y)$ against a/c.

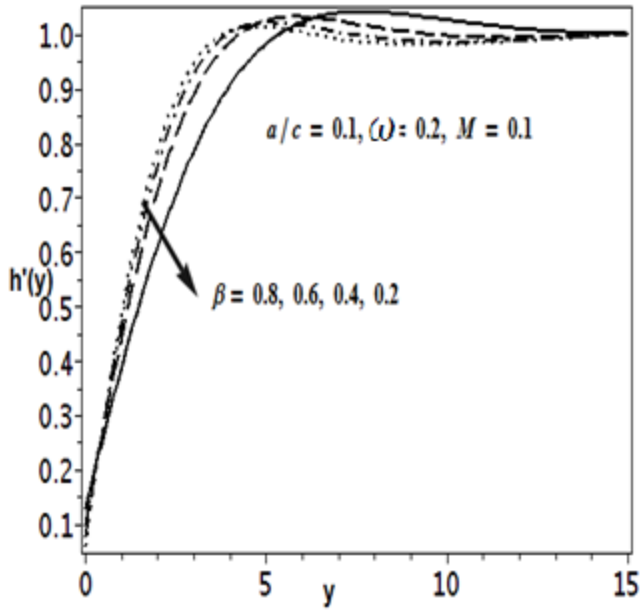

Fig (3.7) Velocity profile $h'(y)$ against β.

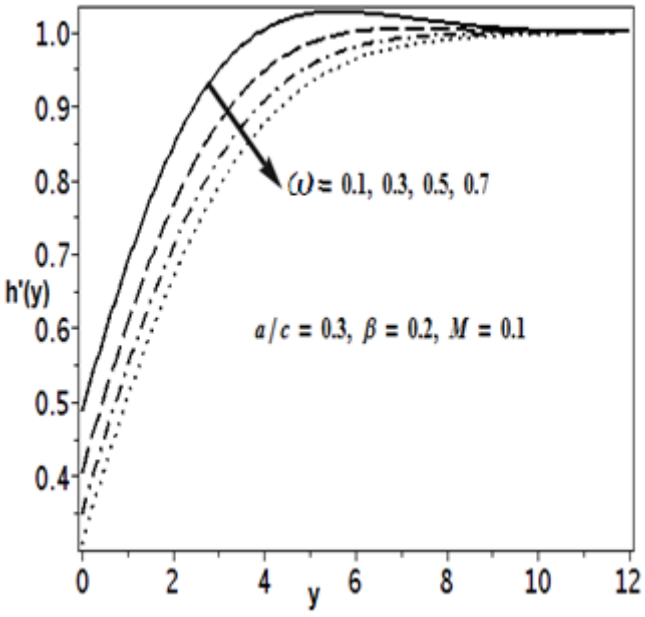

Fig (3.8) Velocity profile $h'(y)$ against ω.

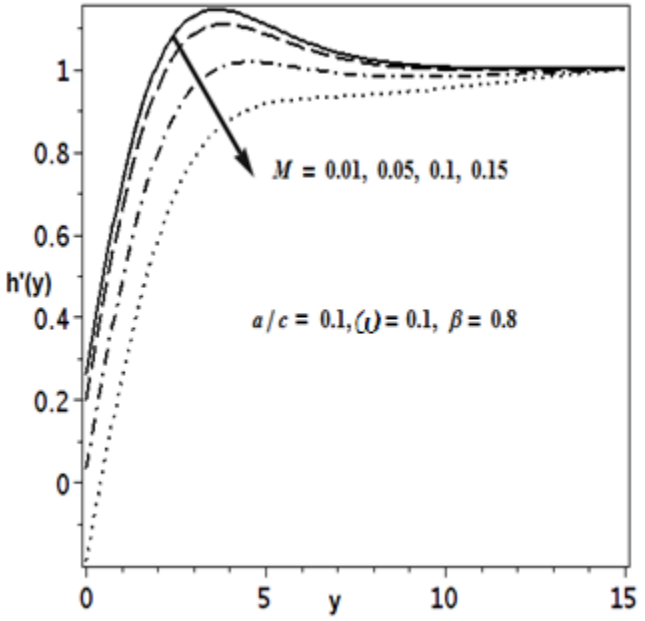

Fig (3.9) Velocity profile $h'(y)$ against M.

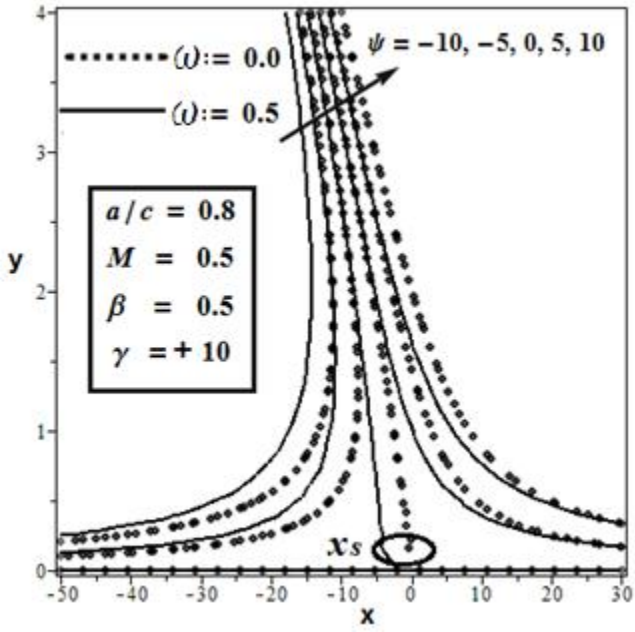

Fig (3.10) Streamlines pattern for slip parameter ω when $\gamma = +10$.

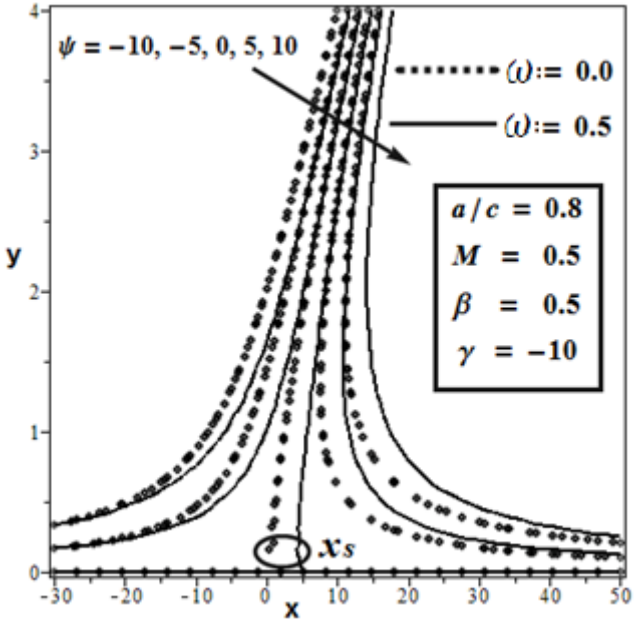

Fig (3.11) Streamlines pattern for slip parameter ω when $\gamma = -10$.

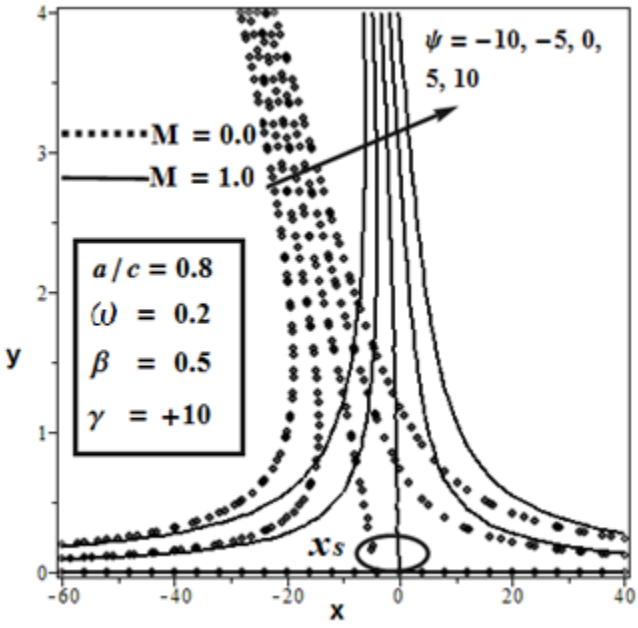

Fig (3.12) Streamlines pattern for magnetic field parameter M when $\gamma = +10$.

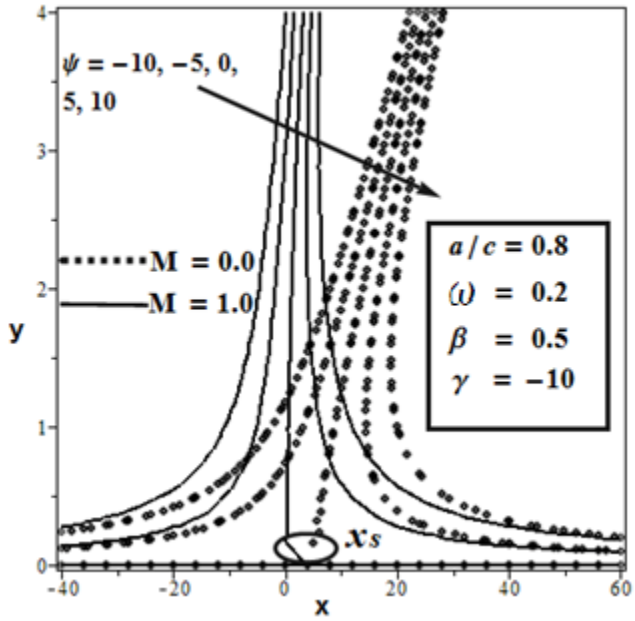

Fig (3.13) Streamlines pattern for magnetic field parameter M when $\gamma = -10$.

	$f''(0)$		$h'(0)$	
a/c	Present	Pop et al [14]	Present	Pop et al [14]
0.1	−0.96938	−0.96938	0.26341	0.26278
0.3	−0.84942	−0.84942	0.60631	0.60573
0.8	−0.29938	−0.29938	0.93472	0.93430
1.0	0.0	0.0	1.0	1.0
2.0	2.01750	2.01750	1.16521	1.16489
3.0	4.72928	4.72928	1.23465	1.23438

Table 3.1: Comparison with the existing literature when $M = 0, \omega = 0$ and $\beta \to \infty$.

a/c	M	ω	β	A	$-f''(0)$	$-h'(0)$
0.1	1.0	0.2	0.5	0.75271	0.48170	0.29380
0.2				0.61653	0.44151	0.23271
0.3				0.50153	0.39732	0.18319
0.1	1.0	0.2	0.5	0.75271	0.48170	0.29380
	1.5			0.54520	0.56612	0.13038
	2.0			0.40236	0.64582	0.06609
0.1	1.0	0.2	0.5	0.75271	0.48170	0.29380
		0.4		0.60269	0.35729	0.18178
		0.6		0.50603	0.28545	0.12530
0.1	1.0	0.2	0.5	0.75271	0.48170	0.29380
			1.0	0.64528	0.63132	0.32681
			2.0	0.57619	0.76105	0.34952

Table 3.2: Numerical values of local skin frictions against non-dimensional parameters.

3.5 Concluding Remarks

A speculative study is directed to confer the combined effects of partial slip and magnetic field on an obliquely striking Casson fluid over a stretching surface. The governing system is solved numerically through midpoint integration scheme with Richardson's extrapolation. Numerical values of normal and tangential components of wall shear stress are tabulated.

These are some of the key findings

- Both normal and tangential velocities drops by increasing slip parameter ω and magnetic parameter M.
- Application of magnetic field through parameter M has opposite influence on normal and tangential skin friction components. On the other hand partial slip parameter ω decays the skin friction coefficients.
- It is exposed from streamline patterns that the point of stagnation x_s is shifted with partial slip and magnetic field.

Chapter 4

Oblique stagnation flow of Jeffery fluid over a stretching convective surface: Optimal Solution

4.1 Introduction

This chapter is related to the steady flow of Jeffery fluid over a stretching surface with convective boundary conditions. It is supposed that fluid strikes the wall in an oblique manner. The flow governing partial differential equations of the non-dimensional problem are presented and converted to ordinary differential equations by means of suitable similarity transformations. Optimal homotopy analysis method (OHAM) is operated to deal the resulting ordinary differential equations. OHAM is found to be extremely effective analytical technique to obtain convergent series solutions of highly non-linear differential equations. Graphically, non-dimensional velocities and temperature profile are expressed. Skin friction coefficients and local heat flux are computed numerically. The comparison of results from this article with the previous existing literature validates the results of (OHAM) for the limited case.

4.2 Mathematical formulation

We considered the steady 2D oblique stagnation point flow of a Jeffery fluid over a stretching surface as shown in Fig (4.1). Further it is assumed that the surface has convective fluid temperature T_f and uniform ambient temperature T_∞ (here $(T_f \rangle T_\infty)$).

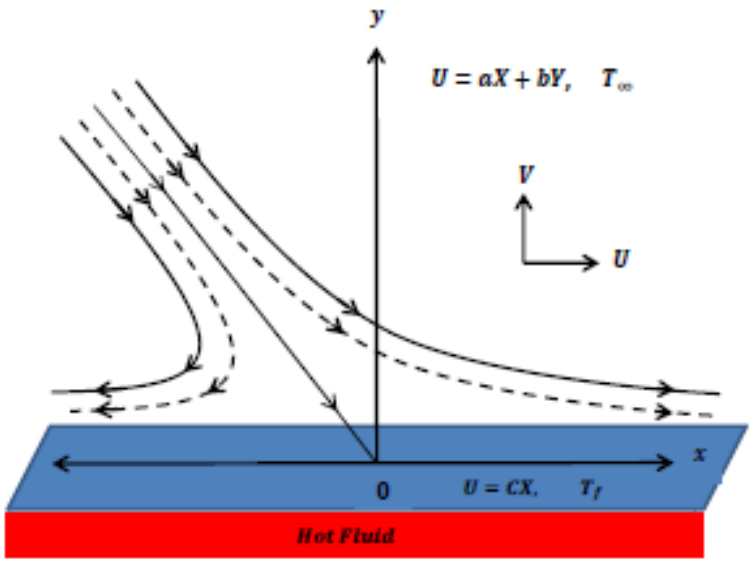

Fig (4.1): Schematic diagram of the flow problem

The expression of extra stress tensor for Jeffery fluid is

$$\boldsymbol{\tau} = -p\boldsymbol{I} + \frac{\mu}{1+\lambda_1}[\boldsymbol{A_1} + \lambda_2(\frac{\partial \boldsymbol{A_1}}{\partial t} + \boldsymbol{V}.\nabla)\boldsymbol{A_1}] \qquad (4.1)$$

Where $\boldsymbol{\tau}$ is the Cauchy stress tensor, μ is the dynamic viscosity, λ_1 and λ_2 are the material constants of the Jeffery fluid and $\boldsymbol{A_1}$ is the Rivlin-Ericksen tensor defined by $\boldsymbol{A_1} = (\nabla \boldsymbol{V}) + (\nabla \boldsymbol{V})^t$.

The flow governing equations for two dimensional flow in component form are defined as

$$\frac{\partial u^*}{\partial x^*}+\frac{\partial v^*}{\partial y^*}=0 \tag{4.2}$$

$$u^*\frac{\partial u^*}{\partial x^*}+v^*\frac{\partial u^*}{\partial y^*}+\frac{1}{\rho}\frac{\partial p^*}{\partial x^*}=\left(\frac{\nu}{1+\lambda_1}\right)[\nabla^{*2}u^*+2\lambda_2\frac{\partial}{\partial x^*}\left(u^*\frac{\partial^2 u^*}{\partial x^{*2}}+v^*\frac{\partial^2 u^*}{\partial x^*\partial y^*}\right)+\lambda_2\frac{\partial}{\partial y^*}\left\{u^*\left(\frac{\partial^2 u^*}{\partial x^*\partial y^*}+\frac{\partial^2 v^*}{\partial x^{*2}}\right)+v^*\left(\frac{\partial^2 v^*}{\partial x^*\partial y^*}+\frac{\partial^2 u^*}{\partial y^{*2}}\right)\right\}], \tag{4.3}$$

$$u^*\frac{\partial v^*}{\partial x^*}+v^*\frac{\partial v^*}{\partial y^*}+\frac{1}{\rho}\frac{\partial p^*}{\partial y^*}=\left(\frac{\nu}{1+\lambda_1}\right)[\nabla^{*2}v^*+2\lambda_2\frac{\partial}{\partial y^*}\left(v^*\frac{\partial^2 v^*}{\partial x^{*2}}+u^*\frac{\partial^2 v}{\partial x^*\partial y^*}\right)+\lambda_2\frac{\partial}{\partial x^*}\left\{u^*\left(\frac{\partial^2 u^*}{\partial x^*\partial y^*}+\frac{\partial^2 v^*}{\partial x^{*2}}\right)+v^*\left(\frac{\partial^2 v^*}{\partial x^*\partial y^*}+\frac{\partial^2 u^*}{\partial y^{*2}}\right)\right\}], \tag{4.4}$$

$$u^*\frac{\partial T^*}{\partial x^*}+v^*\frac{\partial T^*}{\partial y^*}=\alpha^*\nabla^{*2}T^* \tag{4.5}$$

with the following conditions [14]

$$u^*=cx^*, -k\frac{\partial T^*}{\partial y^*}=h_f\left(T_f-T^*\right), at\ y^*=0,$$

$$u^*=ax^*+by^*,\ T^*=T_\infty, as\ y^*\to 0 \tag{4.6}$$

Where a, b, c are positive constant having inverse time dimensions.

In above expressions u^*, v^* are the components of velocity in the x^* and y^*- directions, respectively, ρ is the fluid density, ν is the kinematic viscosity, T^* is the temperature, α^* the thermal diffusivity, k is the thermal conductivity and h_f is termed as convective heat transfer coefficient.

Introducing the following quantities

$$x=x^*\sqrt{\frac{c}{\nu}}, y=y^*\sqrt{\frac{c}{\nu}}, u=\frac{1}{\sqrt{\nu c}}u^*,$$

$$v=\frac{1}{\sqrt{\nu c}}v^*, p=\frac{1}{\mu c}p^*, T=\frac{T^*-T_\infty}{T_f-T_\infty}. \tag{4.7}$$

Making use of Eq (4.7) in Eqs (4.2) – (4.5), we get

$$\frac{\partial u}{\partial x}+\frac{\partial v}{\partial y}=0 \tag{4.8}$$

$$u\frac{\partial u}{\partial x}+v\frac{\partial u}{\partial y}+\frac{\partial p}{\partial x}=\left(\frac{1}{1+\lambda_1}\right)[\nabla^2 u+2K\frac{\partial}{\partial x}\left(v\frac{\partial^2 u}{\partial x\partial y}+u\frac{\partial^2 u}{\partial x^2}\right)+K\frac{\partial}{\partial y}\left\{u\left(\frac{\partial^2 v}{\partial x^2}+\frac{\partial^2 u}{\partial x\partial y}\right)+$$

$$v\left(\frac{\partial^2 u}{\partial y^2}+\frac{\partial^2 v}{\partial x\partial y}\right)\right\}\Big], \tag{4.9}$$

$$u\frac{\partial v}{\partial x}+v\frac{\partial v}{\partial y}+\frac{\partial p}{\partial y}=\left(\frac{1}{1+\lambda_1}\right)[\nabla^2 v+2K\frac{\partial}{\partial y}\left(v\frac{\partial^2 v}{\partial x^2}+u\frac{\partial^2 v}{\partial x\partial y}\right)+K\frac{\partial}{\partial x}\left\{u\left(\frac{\partial^2 v}{\partial x^2}+\frac{\partial^2 u}{\partial x\partial y}\right)+$$

$$v\left(\frac{\partial^2 u}{\partial y^2}+\frac{\partial^2 v}{\partial x\partial y}\right)\right\}\Big], \tag{4.10}$$

$$Pr\left(u\frac{\partial T}{\partial x}+v\frac{\partial T}{\partial y}\right)=\nabla^2 T. \tag{4.11}$$

Defining stream function relations as

$$u=\frac{\partial \psi}{\partial y}, v=-\frac{\partial \psi}{\partial x}. \tag{4.12}$$

Substituting Eq (4.12) in Eqs (4.8)– (4.11), we get

$$\nabla^4\psi+(1+\lambda_1)\frac{\partial(\psi,\nabla^2\psi)}{\partial(x,y)}=K[\left\{\left(\frac{\partial^2}{\partial x^2}-\frac{\partial^2}{\partial y^2}\right)\left(\frac{\partial\psi}{\partial y}\frac{\partial}{\partial x}-\frac{\partial\psi}{\partial x}\frac{\partial}{\partial y}\right)\left(\frac{\partial^2\psi}{\partial y^2}-\frac{\partial^2\psi}{\partial x^2}\right)\right\}+2\frac{\partial^2}{\partial x\partial y}\left(\frac{\partial\psi}{\partial x}\frac{\partial}{\partial x}\nabla^2\psi-$$

$$2\frac{\partial\psi}{\partial y}\frac{\partial}{\partial y}\frac{\partial^2\psi}{\partial x^2}\right)], \tag{4.13}$$

$$Pr\left(\frac{\partial\psi}{\partial y}\frac{\partial T}{\partial x}-\frac{\partial\psi}{\partial x}\frac{\partial T}{\partial y}\right)=\nabla^2 T. \tag{4.14}$$

Along with the boundary conditions

$$\psi=0,\frac{\partial\psi}{\partial y}=x,\frac{\partial T}{\partial y}=-\frac{h_f}{k}\sqrt{\frac{\nu}{c}}(1-T), at\ y=0,$$

$$\psi=\frac{a}{c}xy+\frac{1}{2}\gamma_1 y^2, T=0\ at\ y\to\infty, \tag{4.15}$$

Where $\gamma_1=\frac{b}{c}$ represent shear in the stream. We seek solutions of Eqs (4.13) and (4.14) as

$$\psi(x,y)=xf(y)+g(y), T=\theta(y), \tag{4.16}$$

Replacing Eq (4.16) into Eqs (4.13) – (4.15), after simplification we obtain the following ordinary differential equations along with the corresponding boundary conditions

$$f''' + (1+\lambda_1)(ff'' - f'^2) + K\left(f''^2 - ff^{iv}\right) + C_1 = 0, \quad (4.17)$$

$$g''' + (1+\lambda_1)(fg'' - f'g') + K\left(f'''g' + f''g'' - fg^{iv} - f'g'''\right) + C_2 = 0, \quad (4.18)$$

$$\theta'' + Prf\theta' = 0, \quad (4.19)$$

$$f(0) = 0, f'(0) = 1, f'(\infty) = \frac{a}{c}, g(0) = 0, g'(0) = 0,$$

$$g''(\infty) = \gamma_1, \theta'(0) = -Bi\left(1 - \theta(0)\right), \theta(\infty) = 0. \quad (4.20)$$

Here Prandtl number Pr, non-Newtonian Jeffery parameter K and Biot number Bi are defined as

$$Pr = \frac{\nu}{\alpha}, K = \lambda_2 c, Bi = \frac{h_f}{k}\sqrt{\frac{\nu}{c}}. \quad (4.21)$$

Assuming that $f(y) = \left(\frac{a}{c}\right)y + A$ as $y \to \infty$ and making use of Eq (4.20) in Eq (4.17) we get $C_1 = (1+\lambda_1)(\frac{a}{c})^2$ (Here A denotes boundary layer displacement constant). Taking the limit as $y \to \infty$ in Eq (4.18) and by using $g''(\infty) = \gamma_1$, we get $C_2 = -(1+\lambda_1)A\gamma_1$. Thus Eqs (4.17) and (4.18) become

$$f''' + (1+\lambda_1)(ff'' - f'^2 + (\frac{a}{c})^2) + K\left(f''^2 - ff^{iv}\right) = 0, \quad (4.22)$$

$$g''' + (1+\lambda_1)(fg'' - A\gamma_1 - f'g') + K\left(f'''g' + f''g'' - fg^{iv} - f'g'''\right) = 0, \quad (4.23)$$

$$\theta'' + Prf\theta' = 0. \quad (4.24)$$

Note that in above equations when $K,\ \lambda_1 \to 0$, we obtain the equations for viscous fluid.

Introducing

$$g'(y) = \gamma_1 h(y). \quad (4.25)$$

Making use of Eq (4.25) in (4.23), we have

$$h'' + (1+\lambda_1)(fh' - f'h - A) + K(f'''h + f''h' - fh''' - f'h'') = 0. \quad (4.26)$$

With the corresponding boundary conditions

$$h(0) = 0, h'(\infty) = 1. \quad (4.27)$$

Shear stress and local heat flux at the wall are given in terms of stream function as

$$\tau_w = \left(\frac{1}{1+\lambda_1}\right)\{1 + K\left(\frac{\partial\psi}{\partial y}\frac{\partial}{\partial x} - \frac{\partial\psi}{\partial x}\frac{\partial}{\partial y}\right)\left(\frac{\partial^2\psi}{\partial y^2} - \frac{\partial^2\psi}{\partial x^2}\right)\}_{y=0}, q_w = -k(\frac{\partial T}{\partial y})_{y=0}, \quad (4.28)$$

In dimensionless form above equations take the following form

$$\tau_w = \left(\frac{1}{1+\lambda_1}\right)\{x(1+K)f''(0) + \gamma_1 h'(0)\}, q_w = -\theta'(0). \quad (4.29)$$

The position x_s of attachment of the dividing stream line is determined by the point of zero wall shear stress i.e. $\tau_w = 0$ and can be calculated as

$$x_s = \frac{-\gamma_1 h^{'}(0),}{(1+K)f^{''}(0)} \quad (4.30)$$

4.3 Solution by Optimal Homotopy analysis method

We now solve the nonlinear boundary value problem analytically by OHAM. First of all, it is quite apparent that $f(y), h(y)$ and $\theta(y)$ can be written in terms of base functions [55]. The interested reader can refer to the much cited book [55] for a systematic and clear exposition on the HAM.

$$\{y^k \exp(-ny) \,|k \geq 0, n \geq 0\}. \quad (4.31)$$

The initial guesses for the governing equations are given by

$$f_0(y) = \frac{a}{c}y + \left(1 - \frac{a}{c}\right)(1 - \exp(-y)), \quad (4.32)$$

$$h_0(y) = (-1 + \exp(-y))y, \quad (4.33)$$

$$\theta_0(y) = (\frac{Bi}{1+Bi})\exp(-y), \quad (4.34)$$

and the auxiliary linear operators are

$$L_f = \frac{d^3 f}{dy^3} + \frac{df}{dy}, \tag{4.35}$$

$$L_h = \frac{d^2 h}{dy^2} + \frac{dh}{dy}, \tag{4.36}$$

$$L_\theta = \frac{d^2 \theta}{dy^2} + \frac{d\theta}{dy}, \tag{4.37}$$

4.4 Optimal convergence-control parameters

Conventional HAM involves a single convergence-control parameter say c_0 and it has a drawback that curves against the convergence controlling parameters (i.e. c_0 - curves) cannot leads towards a particular value $c_0 \, \epsilon \, R$ which gives the fastest convergent series. Recently, to fulfill this very deficiency, Liao [58] projected the idea of optimal HAM with more than one convergence-control parameters. He introduced the so-called averaged residual error to get the optimal convergence parameters efficiently. In general, the optimal HAM can improve convergence of homotopic solutions. In our problem we are dealing with three coupled non-linear differential equations, so using (OHAM) means our series solutions contain three non-zero auxiliary parameters c_0^f, c_0^h and c_0^θ to obtain convergence region. In order to find out the total error as well as the individual error we have optimized the so called local convergence control parameters c_0^f, c_0^h and c_0^θ. To find out the optimal values of c_0^f, c_0^h and c_0^θ we have used the idea of average residual error as defined by Liao [58].

$$E_m^f = \frac{1}{k+1} \sum_{j=0}^{k} \{N_f \, (\sum_{i=0}^{m} \hat{f}(y))_{y=j\delta y}\}^2 dy, \tag{4.38}$$

$$E_m^h = \frac{1}{k+1} \sum_{j=0}^{k} \{N_h \, (\sum_{i=0}^{m} \hat{f}(y), \sum_{i=0}^{m} \hat{h}(y))_{y=j\delta y}\}^2 dy, \tag{4.39}$$

$$E_m^{\theta} = \frac{1}{k+1}\sum_{j=0}^{k}\{N_{\theta}\,(\sum_{i=0}^{m}\hat{f}(y), \sum_{i=0}^{m}\hat{\theta}(y))_{y=j\delta y}\}^2 dy, \qquad (4.40)$$

Following Liao [58]

$$E_m^t = E_m^f + E_m^h + E_m^{\theta} \qquad (4.41)$$

Where E_m^t is the total squared residual error, $\delta y = 0.5, k = 20$. We have considered two cases when $Pr = 1.0$ and $Pr = 10$ while other parameters are kept fixed as $K = 0.1 = \lambda_1 = \frac{a}{c}$. Total average squared residual error is minimized by using computational highly efficient software Mathematica. We have utilized the idea of ***Minimize*** to obtain corresponding local optimal convergence parameters. Tables 4.1 and 4.2 are developed to choose the optimal values of so called optimal convergence control parameters. $Table$ 4.1 depicts the minimum value of total averaged squared residual error, while $Table$ 4.2 shows the individual average squared residual error at different orders of approximations. It can be clearly seen that the averaged squared residual errors and total averaged squared residual errors goes on decreasing as we increase the order of approximation. Therefore, one can choose better convergence control parameters through Optimal Homotopy analysis method to obtain convergent results.

	$Pr = 1.0$			$Pr = 10$		
m	2	6	10	2	6	10
c_f^0	-0.12	-0.18	-0.19	-0.12	-0.18	-0.19
c_h^0	-0.64	-0.61	-0.54	-0.64	-0.61	-0.54
c_{θ}^0	-1.10	-1.08	-0.84	-0.09	-0.11	-0.10
E_m^t	4.58×10^{-3}	4.86×10^{-4}	4.11×10^{-4}	6.26×10^{-3}	8.80×10^{-4}	5.96×10^{-4}

$Table$ 4.1 Total averaged squared residual errors for optimal convergence control parameters.

	$Pr = 1.0$			$Pr = 10$		
m	2	6	10	2	6	10
E_m^f	2.48×10^{-4}	2.48×10^{-6}	4.17×10^{-7}	2.35×10^{-4}	2.38×10^{-6}	4.25×10^{-7}
E_m^h	7.76×10^{-3}	9.54×10^{-5}	7.07×10^{-6}	7.78×10^{-3}	9.47×10^{-5}	7.14×10^{-6}
E_m^θ	1.60×10^{-7}	1.46×10^{-9}	6.87×10^{-11}	1.67×10^{-3}	3.93×10^{-4}	1.60×10^{-4}

$Table$ 4.2 Individual squared residual errors for optimal convergence control parameters.

4.5 Results and discussion

The objective here is to analyze effects of emerging non-dimensional parameters of Jeffery fluid model when the boundary conditions are assumed to be convective. $Figs$ (4.2) − (4.15) are plotted for the velocity field, temperature field and the stream lines to have a better understanding of the flow behavior. $Figs$ (4.2) and (4.3) are plotted to discover the influence of stretching ratio a/c on velocity components $f'(y)$ and $h(y)$. Fig (4.2) indicates that increasing the stretching ratio a/c results in an increase in normal component of velocity $f'(y)$. Fig (4.3) describes that when $\frac{a}{c}$ increased, tangential component of velocity $h(y)$is also increased. $Figs$ (4.4) and (4.5) depict the variation of another vital parameter λ_1 on $f'(y)$ and $h(y)$. It is found that with the increase of λ_1, normal component of the velocity $f'(y)$ decreases, whereas an increase in the tangential component $h(y)$ has been noticed. $Figs$ (4.6) and (4.7) are developed to study the influence of non-Newtonian Jeffery parameter K on $f'(y)$ and $h(y)$. The behavior was quite contrary to as it was observed for the

case of λ_1. The variation of arising non-dimensional parameters such as stretching parameter $\frac{a}{c}$, non-Newtonian Jeffery parameter K ratio of relaxation to retardation time λ_1, Prandtl number Pr and Biot number Bi on temperature profile $\theta(y)$ are expressed through $Figs\ (4.8) - (4.12)$. It is found that temperature profile $\theta(y)$ tends to increase with an increase in λ_1, and Biot number Bi, while it depicts a decreasing behavior with an increase in stretching parameter $\frac{a}{c}$, non-Newtonian Jeffery parameter K and Prandtl number Pr Since the Biot number involves the heat transfer coefficient, so a higher Biot number means larger heat transfer coefficient and which ultimately increases the fluid temperature. The stream line patterns for the oblique flows are shown in $Figs\ (4.13) - (4.15)$. The stream line $\psi = 0$ strikes the wall $y = 0$, at $x = x_0$, where x_0 is the stagnation point corresponding to zero wall shear stress. It is noticed from these figures that the stream line patterns are towards the left of the origin for positive values of $\gamma_1 \neq 0$ whereas it is on the right of the origin for negative values of $\gamma_1 \neq 0$.

$Tables\ 4.3 - 4.5$ are presented for local skin friction coefficients and heat flux against emerging non-dimensional parameters. To confirm precision of our calculated results $Table\ 4.3$ is prepared to compare our obtained results with the previous literature for the limited case. From $Table\ 4.4$ we have noticed that the magnitude of $f''(0)$ decreases with stretching parameter $\frac{a}{c}$ and K where as it exhibits an opposite behavior for the case of $h'(0)$. A contrary behavior is observed for both skin frictions $f''(0)$ and $h'(0)$ with an increase in λ_1. Moreover it is also observed that the shifting of the point of stagnation is dependent upon stretching ratio $\frac{a}{c}$, retardation time parameter λ_1 and non-Newtonian Jeffery parameter K. $Table\ 4.5$ depicts that heat transfer $-\theta'(0)$ is decreasing function of ratio of relaxation to retardation time parameter λ_1 whereas it increases with an increase in Biot number Bi, stretching ratio $\frac{a}{c}$ and non-Newtonian

Jeffery parameter K. It is also noticed that local heat flux at the stretching convective surface increases for small as well as large values of Prandtl number Pr.

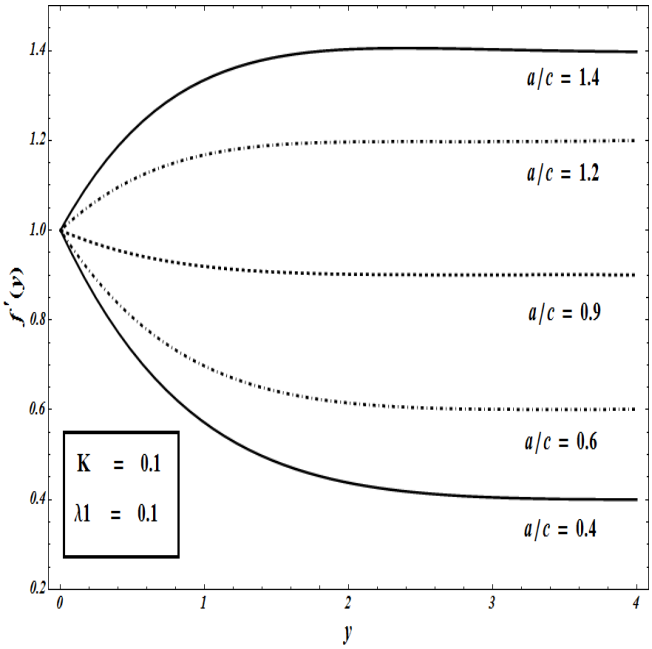

Fig (4.2): Velocity profile $f'(y)$ against a/c.

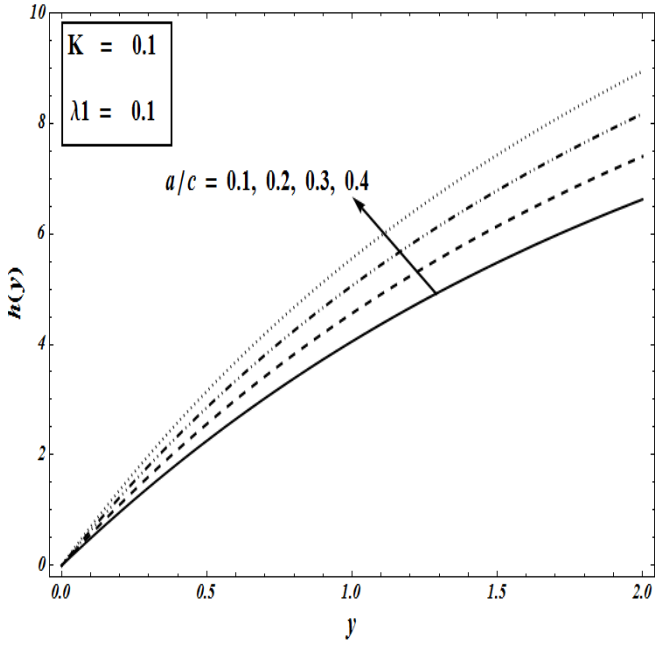

Fig (4.3): Velocity profile $h(y)$ against a/c.

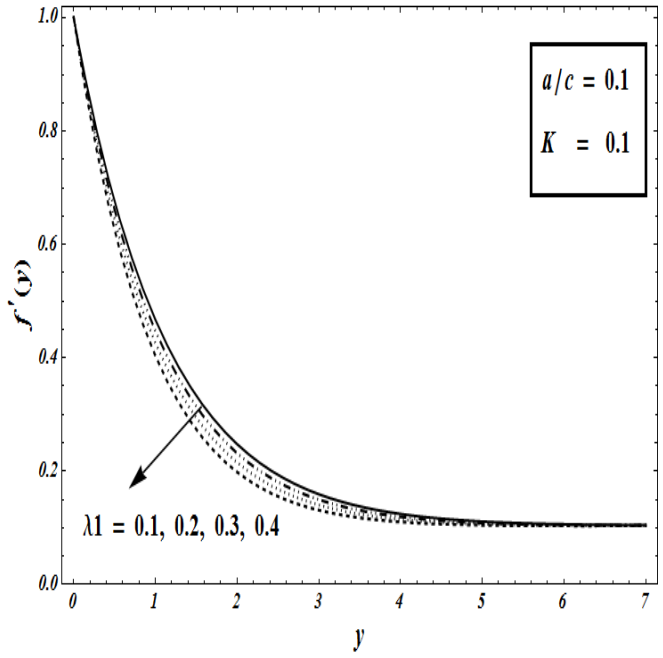

Fig (4.4): Velocity profile $f'(y)$ against λ_1.

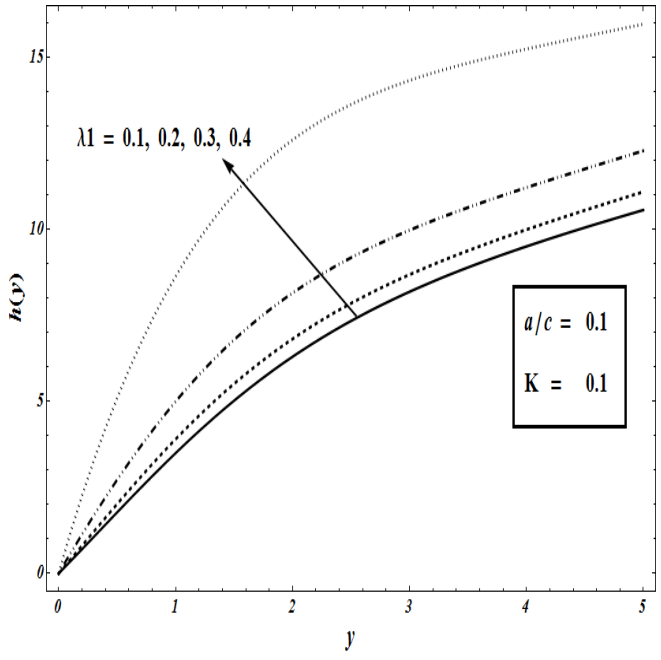

Fig (4.5): Velocity profile $h(y)$ against λ_1.

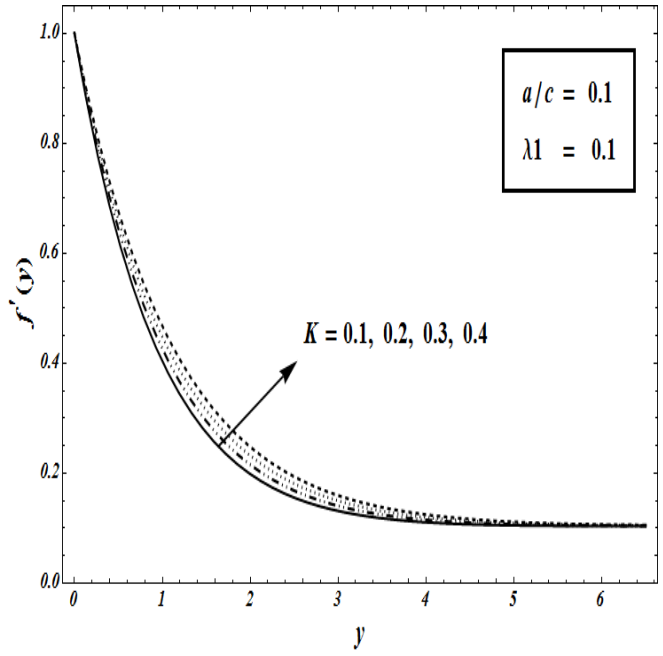

Fig (4.6): Velocity profile $f'(y)$ against K.

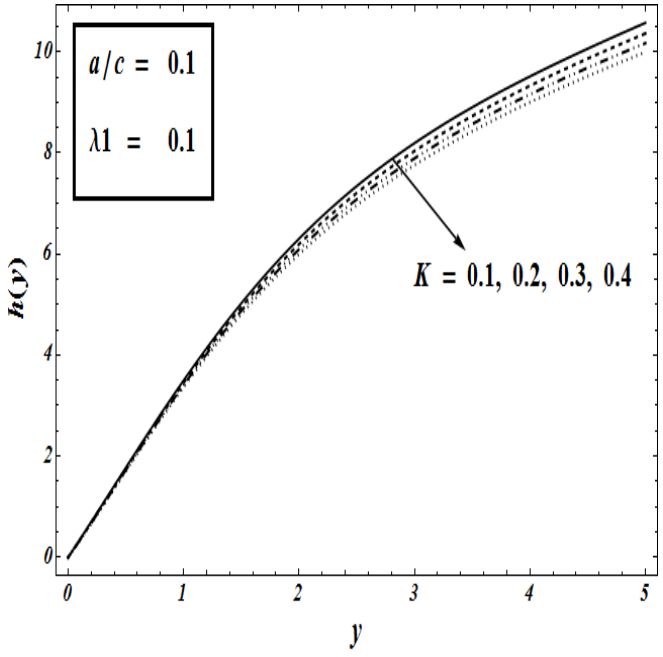

Fig (4.7): Velocity profile $h(y)$ against K.

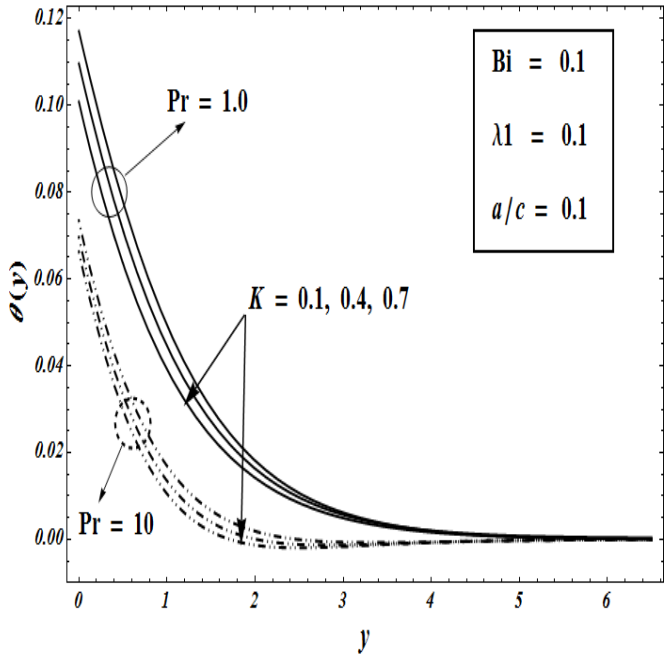

Fig (4.8): Temperature profile $\theta(y)$ against a/c.

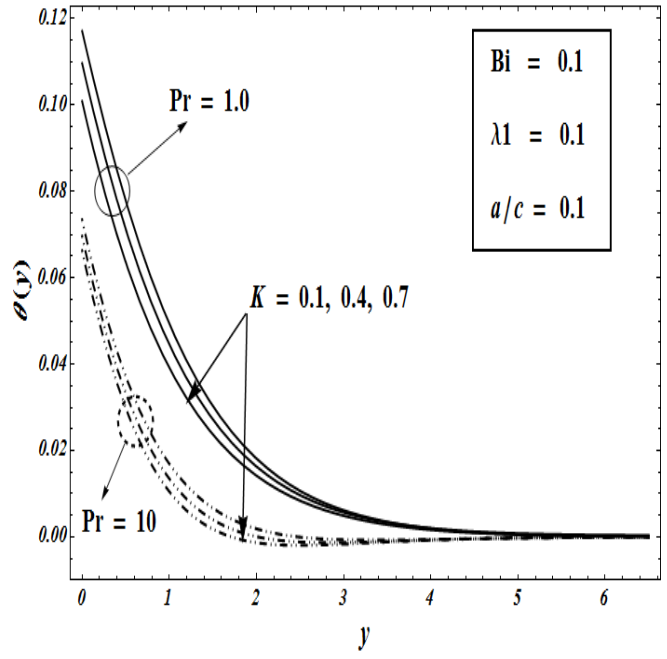

Fig (4.9): Temperature profile $\theta(y)$ against K.

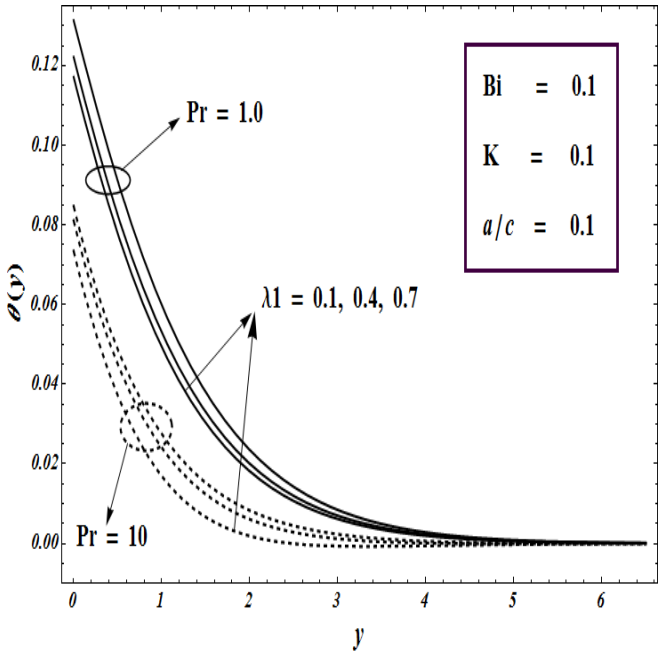

Fig (4.10): Temperature profile $\theta(y)$ against λ_1.

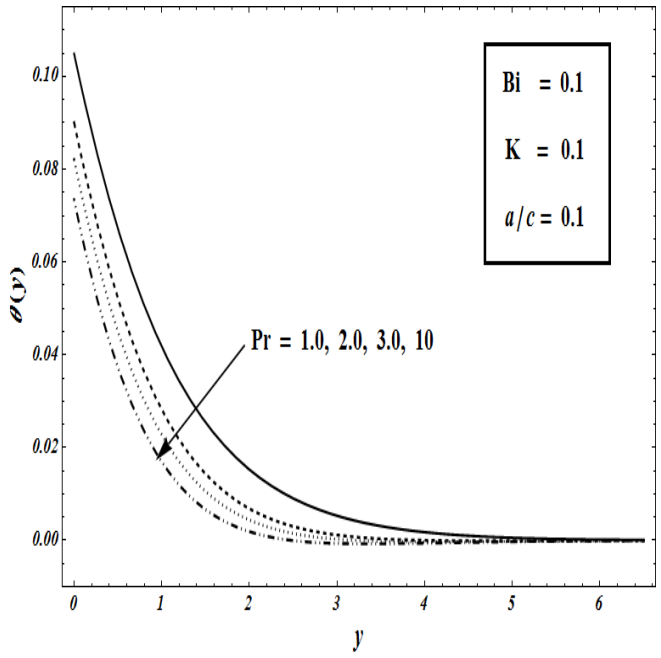

Fig (4.11): Temperature profile $\theta(y)$ against Pr.

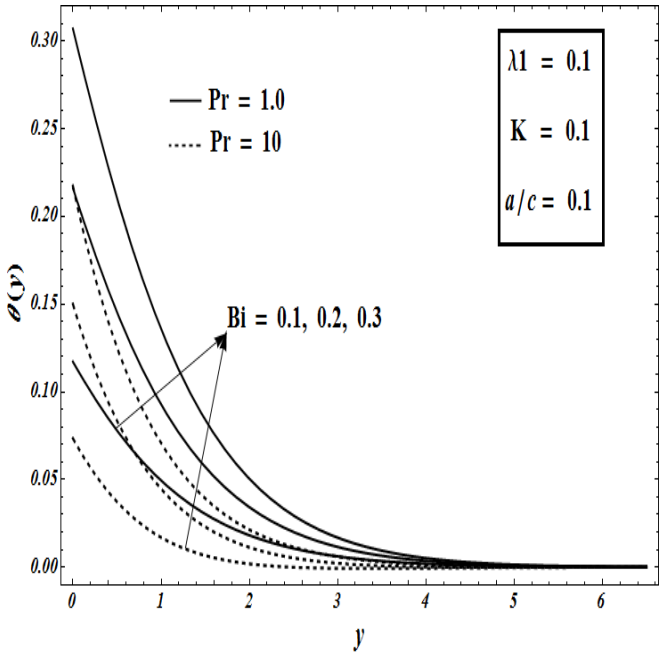

Fig (4.12): Temperature profile $\theta(y)$ againstBi.

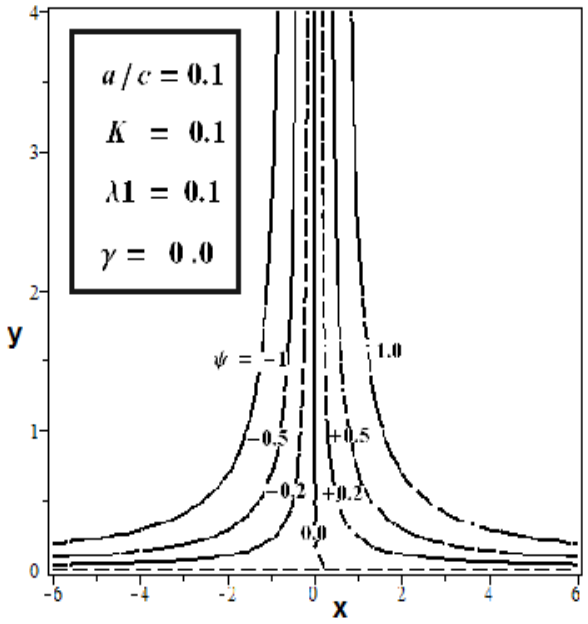

Fig (4.13): Streamlines flow pattern for $\gamma_1 = 0$.

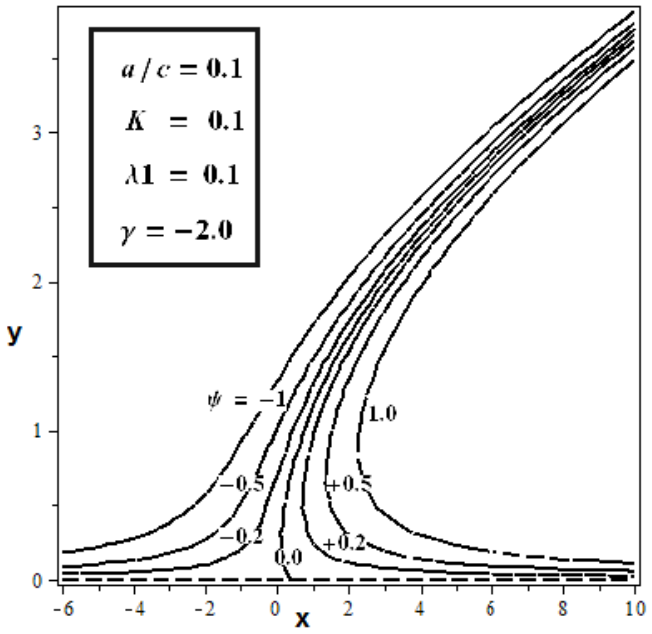

Fig (4.14): Streamlines flow pattern for $\gamma_1 = -2$.

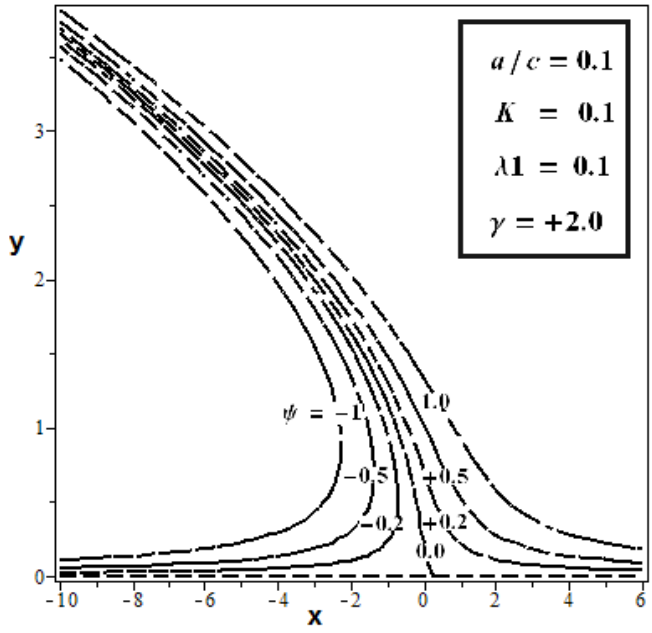

Fig (4.15): Streamlines flow pattern for $\gamma_1 = +2$.

	$f''(0)$			$h'(0)$	
a/c	Present	Mahpatra [7]	Pop et al [14]	Present	Pop et al [14]
0.1	−0.96938	−0.9694	−0.96938	0.26341	0.26278
0.3	−0.84937		−0.84942	0.60631	0.60573
0.8	−0.29937		−0.29938	0.93472	0.93430
1.0	0.0		0.0	1.0	1.0
2.0	2.01750	2.01750	2.01750	1.16522	1.16489
3.0	4.72928	4.72930	4.72928	1.23465	1.23438

$Table$ 4.3: Comparison Table against stretching ratio a/c when $K = 0 = \lambda_1$.

a/c	K	$\lambda 1$	A	$-f''(0)$	$h'(0)$	x_s
0.1	0.1	0.1	0.79501	0.97084	0.18193	0.17036
0.2			0.64524	0.92125	0.40090	0.39507
0.3			0.52440	0.85415	0.54946	0.58480
0.1	0.1	0.1	0.79501	0.97084	0.18193	0.17036
	0.2		0.83324	0.93073	0.10083	0.09028
	0.3		0.86978	0.89526	0.01989	0.01709
0.1	0.1	0.1	0.79501	0.97084	0.18193	0.17036
		0.2	0.76117	1.01401	0.18193	0.16311
		0.3	0.73131	1.05542	0.18193	0.15671

Table 4.4: Numerical values of $A, f''(0), h'(0)$ and point of stagnation x_s when$\gamma = 1$.

a/c	K	λ_1	Pr	Bi	$-\theta'(0)(Pr = 1)$	$-\theta'(0)(Pr = 10)$
0.1	0.1	0.1	1.0	0.1	0.085760	0.095855
0.2					0.086199	0.095862
0.3					0.086620	0.095914
	0.2				0.085906	0.095876
	0.3				0.086035	0.095889
		0.2			0.085610	0.095846
		0.3			0.085467	0.095831
			7.0		0.095011	0.095011
			10		0.095855	0.095855
				0.2	0.150142	0.184106
				0.3	0.200253	0.265605

Table 4.5: Numerical values of local heat flux$-\theta'(0)$.

4.6 Conclusions

We have successfully applied Optimal Homotopy analysis method (OHAM) to achieve series solutions of the considered problem. We have optimized the so called local convergence control parameters. Influence of pertinent parameters on velocities and temperature profile have been depicted graphically. Streamline patterns for several shears in the flow field are expressed graphically. Local skin friction coefficients, heat flux at the stretching convective surface and

numerical values of point of stagnation x_s are calculated and expressed in tabulated form for small and large Prandtl number Pr.

Following conclusions are drawn from this study:

- Non-Newtonian Jeffery fluid parameter K has opposite influence on normal and tangential velocity components whereas it decreases the temperature profile.
- Temperature of the fluid decreases with Prandtl number and it enhances with an increase in Biot number.
- Heat transfer increases with an increase in stretching ratio a/c, non-Newtonian Jeffery parameter K, Prandtl number Pr and Biot number Bi.
- Comparison with the previous existing literature has been made and considerable agreements have been found in the results for the limiting case.

Chapter 5

A comparative study on non-aligned Jeffery nanofluid over a stretched surface with heat transfer

5.1 Introduction

This chapter addresses the problem of oblique stagnation point flow using Jeffery nano fluid as a rheological fluid model. The effects of thermophoresis and Brownian motion are taken into account. The governing nonlinear partial differential equations of the considered problem are obtained and then transformed to ordinary differential equations by using suitable transformations. Consequential highly non-linear system of differential equations are solved numerically through mid-point integration as a basic scheme along with Richardson's extrapolation as an enhancement scheme and analytical results are also obtained using optimal homotopy analysis Method (OHAM). Non-dimensional velocities, temperature and concentration profiles are expressed graphically. Local skin friction coefficients, local heat and mass flux are tabulated numerically as well as analytically for various non-dimensional parameters emerging in our flow problem. Comparison of the numerical data is made with the previous existing literature to confirm the accuracy of present study for the case of Newtonian fluid.

5.2 Mathematical Analysis

We have considered steady oblique flow of a Jeffery nano fluid on a stretched surface. Effects of Brownian motion, thermophoresis and Schmidt number are investigated. All the assumptions are assumed to be same as considered in previous $chapter$ 4. The constitutive equations of mass and motion for Jeffery fluid model are given in Eqs (4.1)– (4.4), while the energy and nanoparticle concentration equations are given in Eqs (2.5) − (2.6). The resulting equations of flow, temperature and concentration of nanoparticles are given by

$$\frac{\partial u^*}{\partial x^*}+\frac{\partial v^*}{\partial y^*}=0 \tag{5.1}$$

$$u^*\frac{\partial u^*}{\partial x^*}+v^*\frac{\partial u^*}{\partial y^*}+\frac{1}{\rho_f}\frac{\partial p^*}{\partial x^*}=\left(\frac{\nu}{1+\lambda_1}\right)[\nabla^{*2}u^*+2\lambda_2\frac{\partial}{\partial x^*}\left(u^*\frac{\partial^2 u^*}{\partial x^{*2}}+v^*\frac{\partial^2 u^*}{\partial x^*\partial y^*}\right)+\lambda_2\frac{\partial}{\partial y^*}\left\{u^*\left(\frac{\partial^2 u^*}{\partial x^*\partial y^*}+\frac{\partial^2 v^*}{\partial x^{*2}}\right)+v^*\left(\frac{\partial^2 v^*}{\partial x^*\partial y^*}+\frac{\partial^2 u^*}{\partial y^{*2}}\right)\right\}], \tag{5.2}$$

$$u^*\frac{\partial v^*}{\partial x^*}+v^*\frac{\partial v^*}{\partial y^*}+\frac{1}{\rho_f}\frac{\partial p^*}{\partial y^*}=\left(\frac{\nu}{1+\lambda_1}\right)[\nabla^{*2}v^*+2\lambda_2\frac{\partial}{\partial y^*}\left(v^*\frac{\partial^2 v^*}{\partial x^{*2}}+u^*\frac{\partial^2 v}{\partial x^*\partial y^*}\right)+\lambda_2\frac{\partial}{\partial x^*}\left\{u^*\left(\frac{\partial^2 u^*}{\partial x^*\partial y^*}+\frac{\partial^2 v^*}{\partial x^{*2}}\right)+v^*\left(\frac{\partial^2 v^*}{\partial x^*\partial y^*}+\frac{\partial^2 u^*}{\partial y^{*2}}\right)\right\}], \tag{5.3}$$

$$u^*\frac{\partial T^*}{\partial x^*}+v^*\frac{\partial T^*}{\partial y^*}=\alpha^*\nabla^{*2}T^*+\frac{(\rho c)_p}{(\rho c)_f}(D_B\nabla^*C^*.\nabla^*T^*+\frac{D_T}{T_\infty}\nabla^*T^*.\nabla^*T^*), \tag{5.4}$$

$$u^*\frac{\partial C^*}{\partial x^*}+v^*\frac{\partial C^*}{\partial y^*}=D_B\nabla^{*2}C^*+\frac{D_T}{T_\infty}\nabla^{*2}T^*. \tag{5.5}$$

The corresponding suitable conditions are [14]

$$u^*=cx^*, v^*=0, T^*=T_w, C^*=C_w \; at \; y^*=0,$$
$$u^*=ax^*+by^*, \; T^*=T_\infty, C^*=C_\infty \; as \; y^*\to\infty \tag{5.6}$$

In above expressions u^* and v^* are the components of velocity along and perpendicular to the surface respectively, ρ_f , ρ_p are the fluid and nanoparticle mass density, ν is kinematic viscosity, T^* is the temperature, C^* is the concentration, C_p is the specific heat of the material and α^* is the thermal diffusivity of the fluid.

Introducing the following quantities

$$x = x^*\sqrt{\frac{c}{\nu}}, y = y^*\sqrt{\frac{c}{\nu}}, u = \frac{1}{\sqrt{\nu c}}u^*,$$

$$v = \frac{1}{\sqrt{\nu c}}v^*, p = \frac{1}{\mu c}p^*, T = \frac{T^*-T_\infty}{T_w-T_\infty}, C = \frac{C^*-C_\infty}{C_w-C_\infty}. \quad (5.7)$$

Eqs (5.1) $-$ (5.5) become

$$\frac{\partial u}{\partial x} + \frac{\partial v}{\partial y} = 0, \quad (5.8)$$

$$u\frac{\partial u}{\partial x} + v\frac{\partial u}{\partial y} + \frac{\partial p}{\partial x} = (\frac{1}{1+\lambda_1})[\nabla^2 u + 2K\frac{\partial}{\partial x}\left(u\frac{\partial^2 u}{\partial x^2} + v\frac{\partial^2 u}{\partial x \partial y}\right) + K\frac{\partial}{\partial y}\left\{u\left(\frac{\partial^2 u}{\partial x \partial y} + \frac{\partial^2 v}{\partial x^2}\right) + v\left(\frac{\partial^2 v}{\partial x \partial y} + \frac{\partial^2 u}{\partial y^2}\right)\right\}\Big], \quad (5.9)$$

$$u\frac{\partial v}{\partial x} + v\frac{\partial v}{\partial y} + \frac{\partial p}{\partial y} = (\frac{1}{1+\lambda_1})[\nabla^2 v + 2K\frac{\partial}{\partial y}\left(v\frac{\partial^2 v}{\partial x^2} + u\frac{\partial^2 v}{\partial x \partial y}\right) + K\frac{\partial}{\partial x}\left\{u\left(\frac{\partial^2 v}{\partial x^2} + \frac{\partial^2 u}{\partial x \partial y}\right) + v\left(\frac{\partial^2 v}{\partial x \partial y} + \frac{\partial^2 u}{\partial y^2}\right)\right\}\Big], \quad (5.10)$$

$$Pr(u\frac{\partial T}{\partial x} + v\frac{\partial T}{\partial y}) = \nabla^2 T + Pr(N_b \nabla C.\nabla T + N_t \nabla T.\nabla T), \quad (5.11)$$

$$Sc\left(u\frac{\partial C}{\partial x} + v\frac{\partial C}{\partial y}\right) = \nabla^2 C + \frac{N_t}{N_b}\nabla^2 T. \quad (5.12)$$

By applying the stream functions relations from Eq (2.20) and similarity solutions from Eq (2.25) in above, we get,

$$f''' + (1+\lambda_1)(ff'' - f'^2) + K\left(f''^2 - ff^{iv}\right) + C_1 = 0, \quad (5.13)$$

$$g''' + (1+\lambda_1)(fg'' - f'g') + K\left(f'''g' - f'g''' + f''g'' - fg^{iv}\right) + C_2 = 0, \quad (5.14)$$

$$\theta'' + Pr(f\theta' + N_b\theta'\phi' + N_t\theta'^2) = 0, \tag{5.15}$$

$$\phi'' + Scf\phi' + \frac{N_t}{N_b}\theta'' = 0, \tag{5.16}$$

$$f(0) = 0, f'(0) = 1, f'(\infty) = \frac{a}{c}, g(0) = 0,$$

$$g'(0) = 0,\ g''(\infty) = \gamma_1, \theta(0) = 1, \theta(\infty) = 0, \tag{5.17}$$

where C_1, C_2 are integral constants to be determined. Here Prandtl number Pr, the non-Newtonian Jeffery parameter K, the thermophoresis parameter N_t, the Brownian motion parameter N_b and the Schmidt number Sc are defined as

$$Pr = \frac{\nu}{\alpha}, K = \lambda_2 c,\ N_t = \frac{D_T}{T_\infty}\frac{(\rho c)_p}{(\rho c)_f}\frac{(T_f - T_\infty)}{\nu},\ N_b = D_B\frac{(\rho c)_p}{(\rho c)_f}\frac{(C_w - C_\infty)}{\nu}, Sc = \frac{\nu}{D_B}. \tag{5.18}$$

Assuming that $f(y) = \left(\frac{a}{c}\right)y + A$ as $y \to \infty$ and using Eq (5.17) we get $C_1 = (1 + \lambda_1)(\frac{a}{c})^2$ and $C_2 = -(1 + \lambda_1)A\gamma_1$, thus we get

$$f''' + (1 + \lambda_1)(ff'' - f'^2 + (\tfrac{a}{c})^2) + K\left(f''^2 - ff^{iv}\right) = 0, \tag{5.19}$$

$$g''' + (1 + \lambda_1)(fg'' - f'g' - A\gamma_1) + K\left(f'''g' - f'g''' + f''g'' - fg^{iv}\right) = 0, \tag{5.20}$$

$$\theta'' + Pr(f\theta' + N_b\theta'\phi' + N_t\theta'^2) = 0, \tag{5.21}$$

$$\phi'' + Scf\phi' + \frac{N_t}{N_b}\theta'' = 0, \tag{5.22}$$

Introducing

$$g'(y) = \gamma_1 h(y). \tag{5.23}$$

Using Eq (5.23) in (5.20), we have

$$h'' + (1 + \lambda_1)(fh' - A - f'h) + K(f'''h - f'h'' + f''h' - fh''') = 0, \tag{5.24}$$

With the boundary conditions

$$h(0) = 0, h'(\infty) = 1, \tag{5.25}$$

5.3 Non-dimensional quantities of Interest

Shear stress and local heat and mass flux at the wall are given in terms of stream function as

$$\tau_w = \left(\frac{1}{1+\lambda_1}\right)\left\{1 + K\left(\frac{\partial\psi}{\partial y}\frac{\partial}{\partial x} - \frac{\partial\psi}{\partial x}\frac{\partial}{\partial y}\right)\left(\frac{\partial^2\psi}{\partial y^2} - \frac{\partial^2\psi}{\partial x^2}\right)\right\}_{y=0},$$

$$q_w = -k\left(\frac{\partial T}{\partial y}\right)_{y=0}, q_m = -D_B\left(\frac{\partial C}{\partial y}\right)_{y=0}. \quad (5.26)$$

In transformed form above equations take the following form

$$\tau_w = \left(\frac{1}{1+\lambda_1}\right)\{x(1+K)f''(0) + \gamma_1 h'(0)\}, q_w = -\theta'(0),\ q_m = -\phi'(0). \quad (5.27)$$

The position x_s of attachment of the dividing stream line is determined by the point of zero wall shear stress i.e. $\tau_w = 0$, and can be calculated as

$$x_s = \frac{-\gamma_1 h'(0),}{(1+K)f''(0)} \quad (5.28)$$

5.4 Method of Solution

5.4.1 Numerical solution

By means of similarity transformations, the governing equations $(5.1) - (5.5)$ are converted to nonlinear differential equations $(5.19) - (5.22)$ along with their appropriate boundary conditions. This system is then solved numerically using mid-point integration approach to avoid certain singularities appearing in the flow governing equations (see for example $[65 - 66]$). The governing system is solved on a sufficiently large but finite domain of y with a mesh size of $\Delta h = 0.001$ until we achieved the desired degree of accuracy, called 10^{-6}.

5.4.2 Analytical solution by Optimal Ham

In order to verify our numerical results, the governing equations $(5.19) - (5.22)$ are also solved analytically through optimal HAM. The detailed procedure of OHAM has already been provided in $chapter$ 2. Here we will provide the total and individual averaged squared residual errors. The initial guesses f_0, h_0, θ_0 and ϕ_0 of $f(y), h(y), \theta(y)$ and $\phi(y)$ are selected as follow

$$f_0(y) = \frac{a}{c}y + \left(1 - \frac{a}{c}\right)(1 - \exp(-y)), \qquad (5.29)$$

$$h_0(y) = \alpha * (1 - \exp(-y)) + y, \qquad (5.30)$$

$$\theta_0(y) = \exp(-y), \qquad (5.31)$$

$$\phi_0(y) = \exp(-y), \qquad (5.32)$$

We select the auxiliary linear operators as

$$L_f = \frac{d^3 f}{dy^3} - \frac{df}{dy}, \qquad (5.33)$$

$$L_h = \frac{d^2 h}{dy^2} - h, \qquad (5.34)$$

$$L_\theta = \frac{d^2 \theta}{dy^2} - \theta, \qquad (5.35)$$

$$L_\phi = \frac{d^2 \phi}{dy^2} - \phi, \qquad (5.36)$$

5.4.3 Optimal convergence-control parameters

To determine suitable values of convergence parameters $c_0^f, c_0^h, c_0^\theta, c_0^\phi$ and α we have utilized the idea of so-called Average Square Residual Error defined by [58].

$$E_m^f = \frac{1}{k+1}\sum_{j=0}^{k}\{N_f\,(\sum_{i=0}^{m}\hat{f}(y))_{y=j\delta y}\}^2 dy, \qquad (5.37)$$

$$E_m^h = \frac{1}{k+1}\sum_{j=0}^{k}\{N_h\,(\sum_{i=0}^{m}\hat{f}(y), \sum_{i=0}^{m}\hat{h}(y))_{y=j\delta y}\}^2 dy, \qquad (5.38)$$

$$E_m^\theta = \frac{1}{k+1}\sum_{j=0}^{k}\{N_\theta\,(\sum_{i=0}^{m}\hat{f}(y), \sum_{i=0}^{m}\hat{\theta}(y))_{y=j\delta y}\}^2 dy, \qquad (5.39)$$

$$E_m^\phi = \frac{1}{k+1}\sum_{j=0}^{k}\{N_\phi\,(\sum_{i=0}^{m}\hat{f}(y), \sum_{i=0}^{m}\hat{\phi}(y))_{y=j\delta y}\}^2 dy, \qquad (5.40)$$

Following Liao [58]

$$E_m^t = E_m^f + E_m^h + E_m^\theta + E_m^\phi \qquad (5.41)$$

Where E_m^t is the total squared residual error, $\delta y = 0.5, k = 20$. we have considered a case where $Nt = 0.1, Nb = 0.1, Pr = 1.0 = Sc, \frac{a}{c} = 0.1 = K = \lambda_1$. Total average squared residual error is minimized by using Mathematica package $\boldsymbol{BVPh\ 2.0}$. $Tables$ 5.1 and 5.2 are prepared for the case of several optimal convergence control parameters. $Table$ 5.1 shows the minimum value of total averaged squared residual error, while $Table$ 5.2 shows the individual average squared residual error at different orders of approximations using the optimal values from $Table$ 5.1 at $m = 10$. We can observe that the averaged squared residual errors and total averaged squared residual errors goes on decreasing with higher order approximations. Besides these Tables, graphical results for velocities, temperature, concentration and averaged squared residual error are also provided through $Figs$ (5.1) and (5.2). From these figures we can see that our obtained results are very much correct and it is also noticed that the total averaged squared residual error decreases as we increase the number of iterations (see Fig 5.2).

m	c_0^f	c_0^h	c_0^θ	c_0^ϕ	α	E_m^t	$CPU\ TIME[S]$
4.0	-1.26	-0.91	-0.91	-1.15	$+0.02$	3.11×10^{-5}	31.95
6.0	-0.40	-1.19	-1.01	-1.14	-0.29	1.46×10^{-5}	116.0
8.0	-0.38	-1.01	-0.87	-1.33	-0.27	2.59×10^{-6}	415.9
10	-0.36	-0.90	-1.03	-1.31	-0.26	4.71×10^{-7}	1395.0

Table 5.1**:** Total Averaged squared residual errors using $BVPh2.0$

m	E_m^f	E_m^h	E_m^θ	E_m^ϕ	CPU TIME[S]
2.0	1.39×10^{-4}	3.38×10^{-3}	1.09×10^{-4}	2.48×10^{-3}	0.98
6.0	1.94×10^{-6}	1.10×10^{-5}	5.92×10^{-7}	1.08×10^{-6}	8.37
10	3.02×10^{-8}	6.61×10^{-6}	1.60×10^{-8}	1.18×10^{-7}	34.99
14	6.17×10^{-10}	5.94×10^{-6}	5.59×10^{-10}	7.16×10^{-9}	100.7

Table 5.2**:** Individual Averaged squared residual errors using optimal values at $m = 8$ from *Table* 5.1.

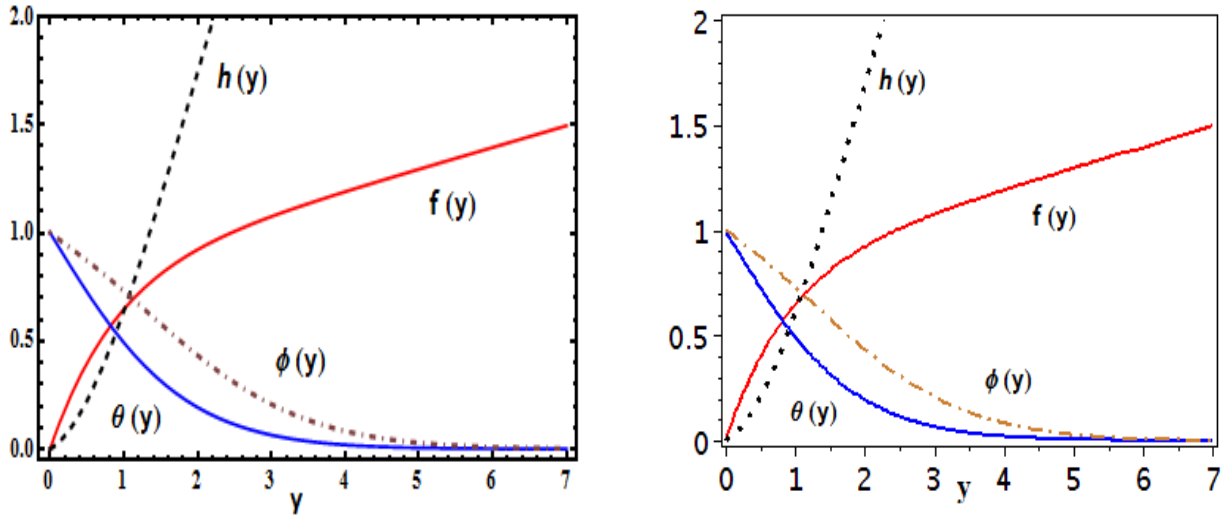

Fig (5.1) Graphical comparison for velocities, temperature and concentration profiles using Numerical scheme (Right) and OHAM (Left).

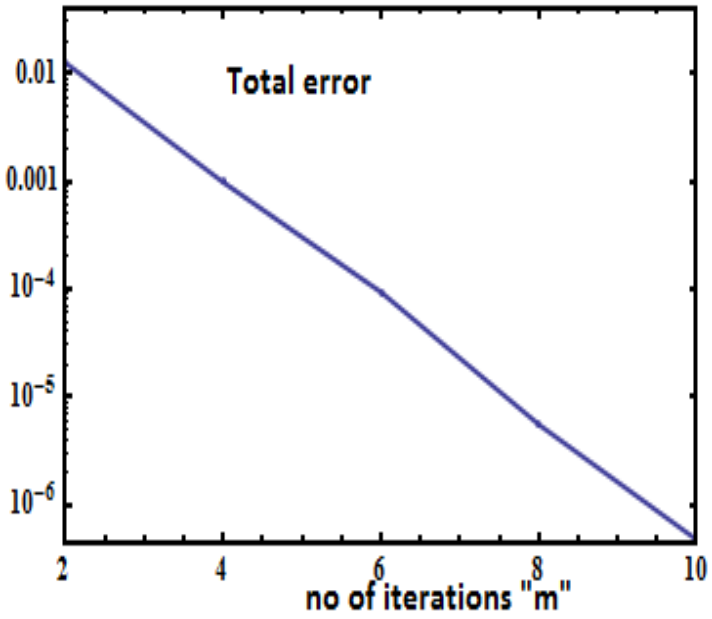

Fig (5.2) Total averaged squared Residual Error against no of iterations m.

5.5 Results and discussion

This section deals with the graphical description of velocity, temperature and concentration profiles for several emerging non-dimensional parameters in our flow problem. $Figs$ (5.3) – (5.14) are plotted for this purpose. $Figs$ (5.3) and (5.4) are plotted to discover the influence of stretching ratio $\frac{a}{c}$ and non-Newtonian Jeffery parameter K on normal and tangential velocity components i.e. $f'(y)$ and $h'(y)$. Fig (5.3) indicates that increasing the stretching ratio $\frac{a}{c}$ and non-Newtonian Jeffery parameter K results in an increase in the normal component of the velocity $f'(y)$. Fig (5.4) describes that when $\frac{a}{c}$ increases; tangential component of velocity $h'(y)$ also increases. We can also notice that when $\frac{a}{c} < 1$, increasing the non-Newtonian Jeffery parameter K decreases the tangential component of velocity $h'(y)$ until $(y > 1)$ but after that the behavior is reversed. On the other hand this behavior is found to be quite contrary when stretching ratio $\frac{a}{c} > 1$. Fig (5.5) and Fig (5.6) exhibit the influence of non-dimensional parameter λ_1 which is the ratio of relaxation to retardation time on $f'(y)$ and $h'(y)$. It is found that with increasing ratio λ_1 normal component of the velocity $f'(y)$ decreases where as an increase in the tangential component $h'(y)$ has been noticed when $\frac{a}{c} < 1$, but this tendency is reversed when $\frac{a}{c} > 1$. Influence of non-dimensional parameters such as thermophoresis parameter N_t, Brownian motion parameter N_b, Prandtl number Pr and Schmidt number Sc on the temperature profile $\theta(y)$ and concentration profile $\phi(y)$ are discussed through $Figs$ (5.7) – (5.14). It is depicted from Fig (5.7) and (5.8) that temperature profile $\theta(y)$ and concentration profile $\phi(y)$ tends to increase with an increase in thermophoresis parameter N_t. The corresponding thermal and diffusion boundary layer thickness

also increase with an increase in thermophoresis parameter N_t. It is noticed from $Figs.$ (5.9) and (5.10) that Brownian motion parameter N_b has opposite influence on the temperature profile $\theta(y)$ and concentration profile $\phi(y)$. Increasing the Brownian motion parameter N_b enhances the temperature profile $\theta(y)$ and the corresponding thermal boundary layer thickness appreciably increases but on the other hand concentration profile $\phi(y)$ as well as the related diffusive boundary layer thickness decays significantly with an increase in Brownian motion parameter N_b. This is due to the fact that an increase in the Brownian motion leads to an increase in more random collisions with in the fluid particles which consequently heats up the fluid and raises its temperature and decreases its concentration. Fig (5.11) describes that temperature profile $\theta(y)$ drops prominently and thermal boundary layer thickness rapidly decreases for large values of Prandtl number Pr, while it is quite evident from Fig (5.12) that when Prandtl number Pr is increased; concentration profile $\phi(y)$ initially increases and then goes on decreasing away from the surface. Finally the influence of Schmidt number Sc on the temperature profile $\theta(y)$ and concentration profile $\phi(y)$ are presented through $Figs$ (5.13) and (5.14). The behaviour of both these non-dimensional quantities against Schmidt number Sc is found to be opposite, i.e. it enhances the temperature profile $\theta(y)$ while decrease the concentration profile $\phi(y)$. Interestingly, it is observed from Fig (5.14) that for large values of Schmidt number Sc; diffusion boundary layer thickness decreases abruptly. $Tables$ 5.3 – 5.5 are presented for the numerical values of components of shear stress at the wall, local heat flux and mass against emerging parameters of interest. $Table$ 5.3 provides a comparison with the existing results for the limited case and it shows that our computed results are in very good agreement. From $Table$ 5.4 it is noticed that absolute values of the normal component of shear stress $f''(0)$ declines with an increase in stretching parameter $\frac{a}{c}$ and Jeffery

parameter K and increases with an increase in the ratio of relaxation to retardation time parameter λ_1, where as it exhibits an opposite behavior for the case of stretching parameter $\frac{a}{c}$ and Jeffery parameter K for the tangential skin friction coefficient $h'(0)$.We have observed that λ_1 has no substantial effect on skin friction coefficient component $h'(0)$. One can also observe very easily that local heat flux $-\theta'(0)$ and mass flux $-\phi'(0)$ are reduced with an increase of stretching ratio $\frac{a}{c}$. Local heat and mass flux are responding in an opposite manner for both non-Newtonian Jeffery parameter K and ratio of relaxation to retardation time λ_1. $Table$ 5.5 shows that local heat flux $-\theta'(0)$ is decreasing function of thermophoresis parameter N_t, Brownian motion parameter N_b and Schmidt number Sc, while it decreases with Prandtl number Pr. Local mass flux $-\phi'(0)$ at the wall increases with an increase in Brownian motion parameter N_b, Prandtl number Pr, Schmidt number Sc and thermophoresis parameter N_t.

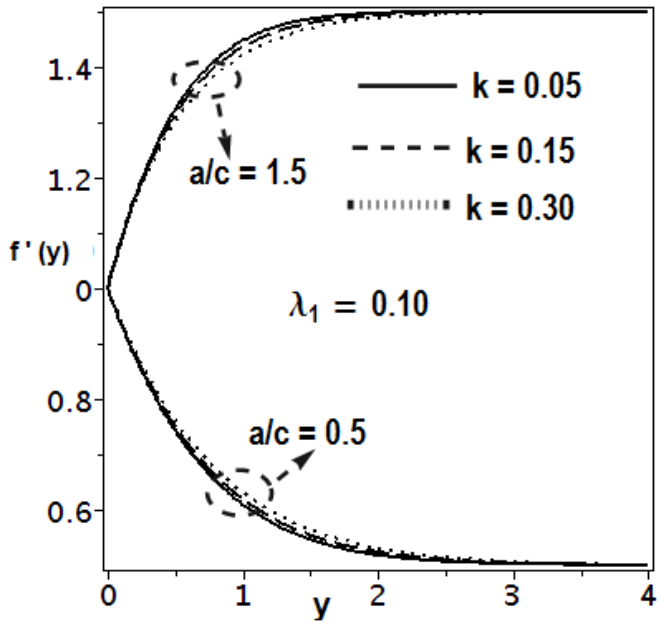

Fig (5.3): Velocity profile $f'(y)$against K.

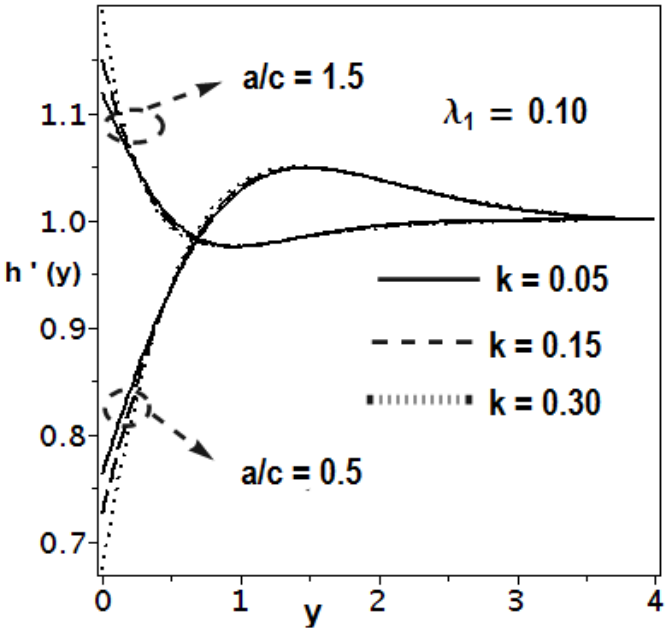

Fig (5.4): Velocity profile $h'(y)$against K.

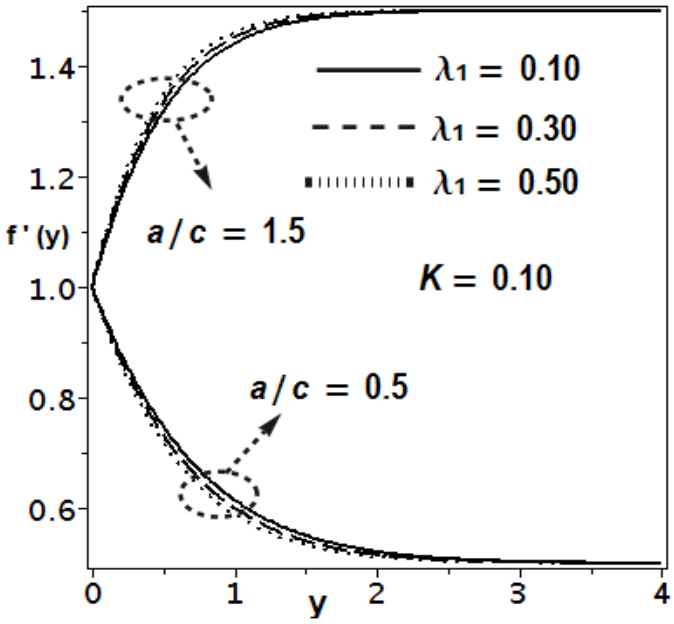

Fig (5.5): Velocity profile $f'(y)$against λ_1.

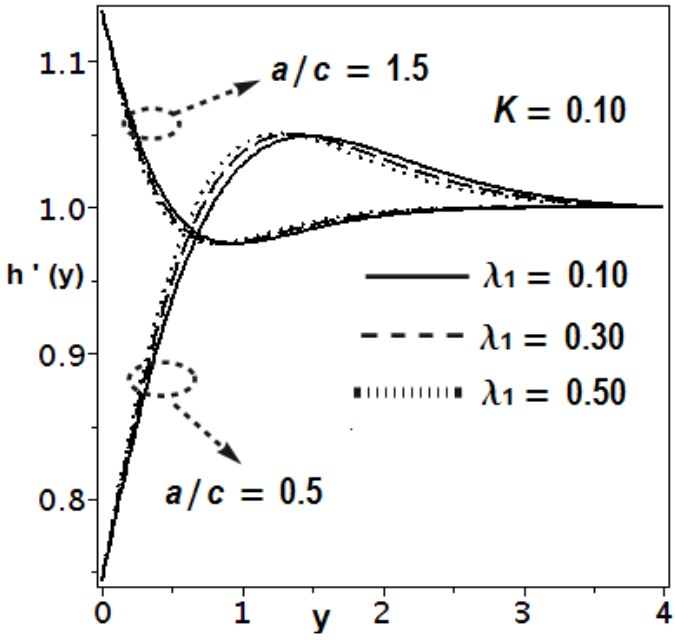

Fig (5.6): Velocity profile $h'(y)$against λ_1.

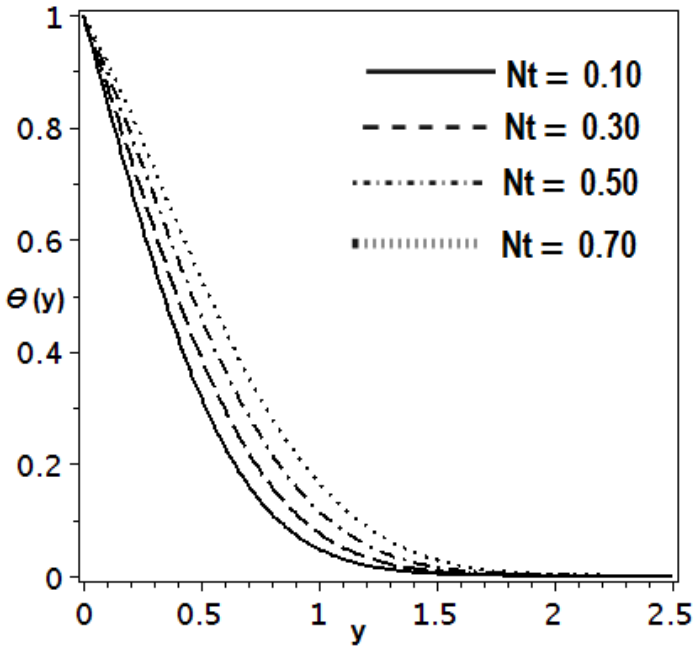

Fig (5.7): Temperature profile $\theta(y)$ against Nt.

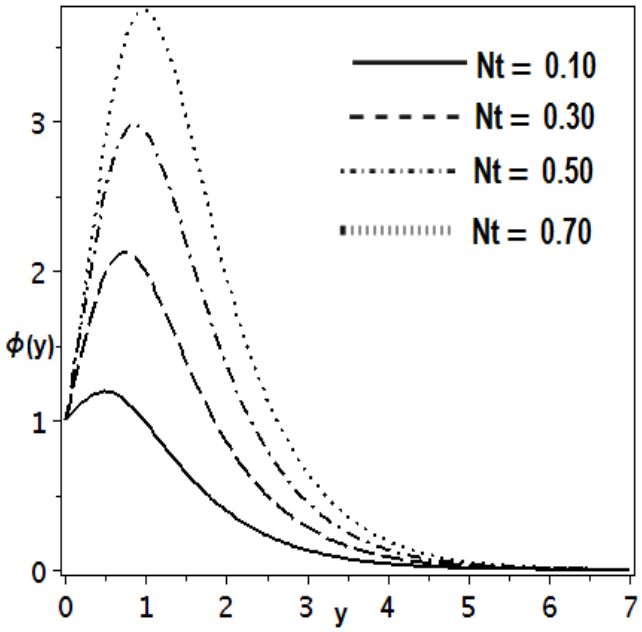

Fig (5.8): Concentration profile $\phi(y)$ against Nt.

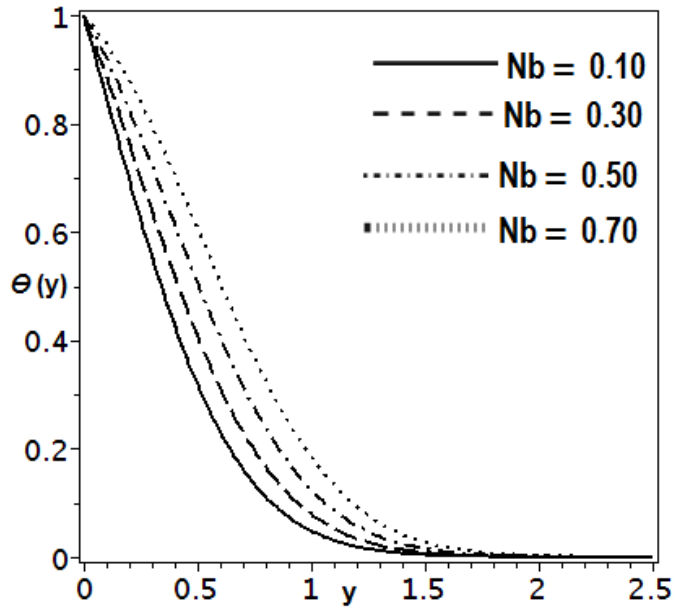

Fig (5.9): Temperature profile $\theta(y)$ against Nb.

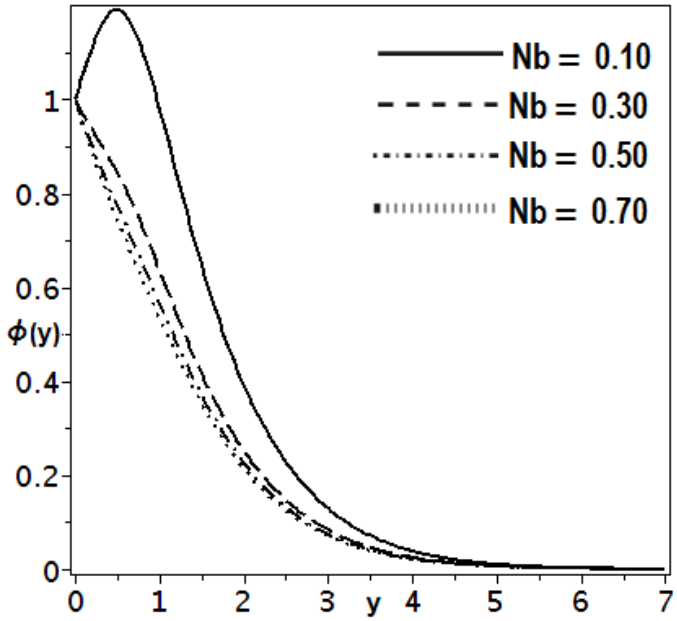

Fig (5.10): Concentration profile $\phi(y)$ against Nb.

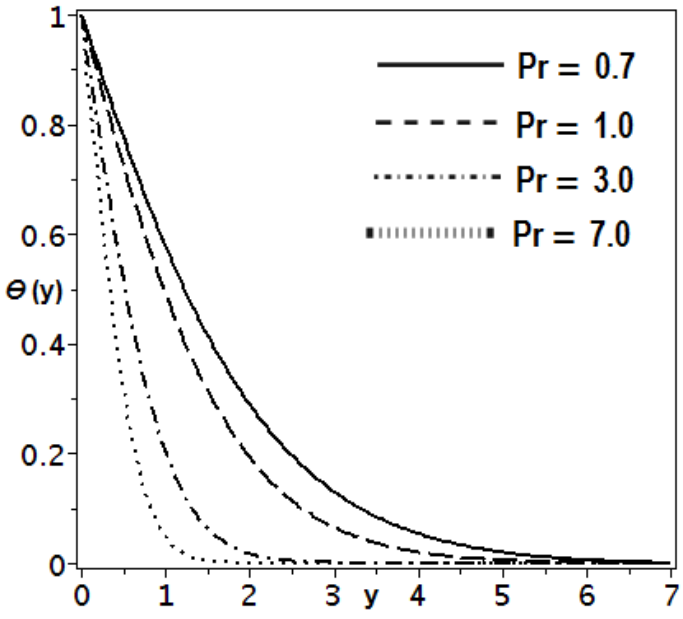

Fig (5.11): Temperature profile $\theta(y)$ against Pr.

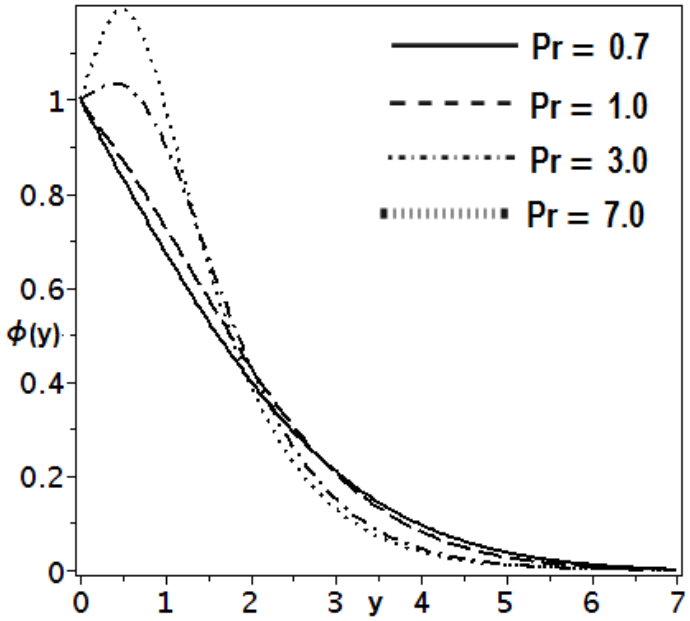

Fig (5.12): Concentration profile $\phi(y)$ against Pr.

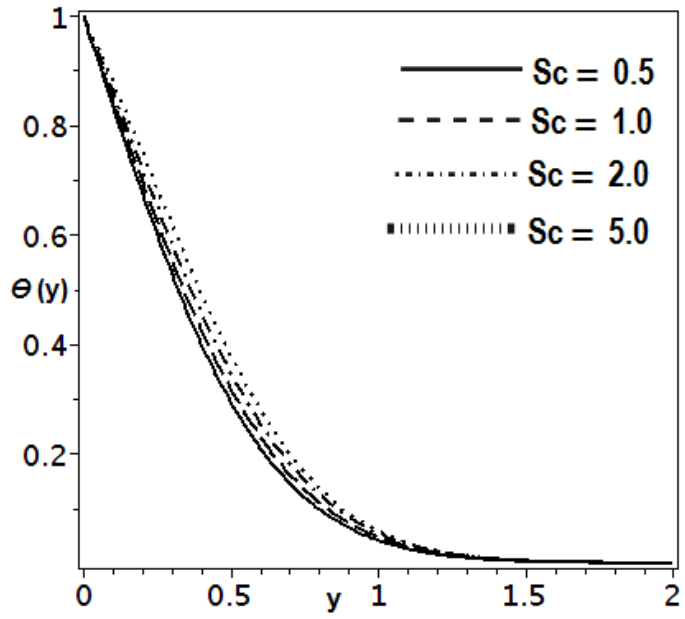

Fig (5.13): Temperature profile $\theta(y)$ against Sc.

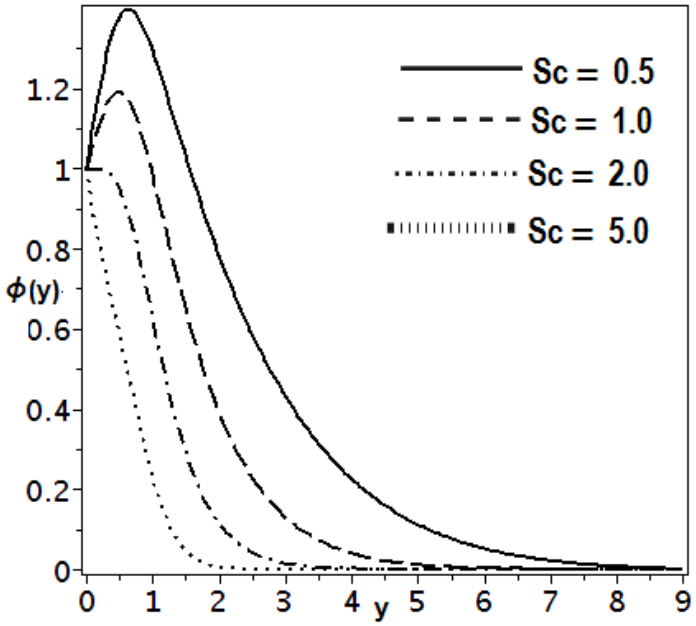

Fig (5.14): Concentration profile $\phi(y)$ against Sc.

	$f''(0)$			$h'(0)$		$-\theta'(0)$	
a/c	Present	Mahapatra [7]	Pop et al [14]	Present	Pop et al [14]	Present	Pop et al [14]
0.1	−0.96938	−0.9694	−0.96938	0.26341	0.26278	0.60215	0.60281
0.3	−0.84937		−0.84942	0.60631	0.60573	0.64728	0.64732
0.8	−0.29937		−0.29938	0.93472	0.93430	0.75709	0.75709
1.0	0.0		0.0	1.0	1.0	0.79788	0.79788
2.0	2.01750	2.01750	2.01750	1.16522	1.16489	0.97872	0.97872
3.0	4.72928	4.72930	4.72928	1.23465	1.23438	1.13209	1.13209

Table 5.3: Comparison Table for a/c when $K = \lambda_1 = 0 = Nt = Nb$.

				Numerical				*Optimal Ham*			
a/c	K	$\lambda 1$	A	$f''(0)$	$h'(0)$	$-\theta'(0)$	$-\varphi'(0)$	$f''(0)$	$h'(0)$	$-\theta'(0)$	$-\varphi'(0)$
0.1	0.1	0.1	0.79501	0.97084	0.18193	1.69700	−0.70932	0.97084	0.18190	1.69700	−0.70932
0.2			0.64524	0.92125	0.40090	1.68769	−0.65506	0.92125	0.40088	1.68769	−0.65506
0.3			0.52440	0.85415	0.54946	1.68236	−0.60428	0.85415	0.54989	1.68236	−0.60428
0.1	0.2	0.1	0.83324	0.93073	0.10083	1.69858	−0.69680	0.93073	0.10076	1.69858	−0.69680
	0.3		0.86978	0.89526	0.01988	1.69989	−0.68545	0.89526	0.01984	1.69989	−0.68545
0.1	0.1	0.2	0.76117	1.01401	0.18193	1.69486	−0.72128	1.01401	0.18193	1.69486	−0.72128
		0.3	0.73131	1.05542	0.18193	1.69265	−0.73226	1.05542	0.18193	1.69265	−0.73226

Table 5.4: Numerical values of non-dimensional constant $f''(0)$, $h'(0)$ and $-\theta'(0)$, $-\phi'(0)$ when $Pr = 10$.

				Numerical		*Optimal Ham*	
Nt	Nb	Sc	Pr	$-\theta'(0)$	$-\varphi'(0)$	$-\theta'(0)$	$-\varphi'(0)$
0.1	0.1	1.0	10	1.69700	−0.70932	1.69700	−0.70932
0.2				1.47233	−1.59697	1.47233	−1.59697
0.3				1.27444	−2.1417	1.27444	−2.1417
	0.2			1.39095	0.09166	1.39095	0.09166
	0.3			1.11882	0.34706	1.11882	0.34706
		2.0		1.46223	−0.02179	1.46223	−0.02179
		3.0		1.31974	0.44769	1.31974	0.44769
			1.0	0.55531	0.25746	0.55531	0.25746
			7.0	1.47603	−0.51180	1.47603	−0.51180

10	1.69700	−0.70932	1.69700	−0.70932

$Table$ 5.5: Numerical values of local heat flux $-\theta'(0)$ and local mass flux $-\phi'(0)$ when $Pr = 10$.

5.6 Conclusions

This numerical study is conducted to highlight the problem of oblique flow of a rheological Jeffery fluid model under the influence of nanoparticles. Normal and tangential components of local shear stress, local heat and mass flux are calculated and expressed in tabulated form.

These are few of the key findings.

- Local skin friction coefficients exhibits a contrary behavior with an increase in stretching ratio $\frac{a}{c}$, while local heat flux as well as local mass flux reduces by an increase in stretching ratio $\frac{a}{c}$.
- It is found that heat flux $-\theta'(0)$ is increasing function of non-Newtonian Jeffery parameter K and Prandtl number Pr.
- Thermophoresis Nt and Brownian motion Nb decays heat flux $-\theta'(0)$ at the wall.
- The effects of Brownian motion Nb and thermophoresis Nt on the local mass flux $-\phi'(0)$ are opposing each other.
- Comparison with the previous existing literature has been made and considerable agreement has been found in the results for the limiting case.

Chapter 6

MHD second grade oblique flow over a convective surface with soret and dufour effects

6.1 **Introduction**

This chapter addresses the soret dufour effects on a steady, 2-D magneto hydrodynamic (MHD) flow of an obliquely striking second grade fluid over a convective surface. The governing systems of equations are extremely complicated and non-linear in nature which are tackled by midpoint integration scheme with Richardson's extrapolation. The results for normal and tangential velocities, temperature and concentration are analysed. Numerical computations are performed to discover the influence of pertinent non-dimensional parameters on normal and tangential components of local shear stress, local heat flux and local mass flux. It is found that magnetic field disturbs obliqueness of the flow, decreases the normal skin friction co-efficient whereas it enhances the tangential skin friction co-efficient. Influences of soret number and dufour number on temperature and concentration are found to be quite opposite. A suitable agreement with the existing literature is shown to endorse the current study for the limiting case.

6.2 Mathematical Formulation

Consider a steady, 2D MHD oblique viscoelastic fluid which meets stretched convective surface in a non-aligned manner. Surface is made to keep stretched along the $x-axis$. Magnetic field of uniform strength B_0 is imposed along $y-axis$, which is normal to the surface which is presented through Fig (6.1).

The Cauchy stress tensor for second grade viscoelastic fluid is given by

$$\boldsymbol{\tau} = -p\boldsymbol{I} + \mu\boldsymbol{A_1} + \alpha_1\boldsymbol{A_2} + \alpha_2(\boldsymbol{A_1})^2$$

Where $\boldsymbol{A_1}$ and $\boldsymbol{A_2}$ are first and second Rivlin-Ericksen tensors given by $\boldsymbol{A_1} = (\nabla \boldsymbol{V}) + (\nabla \boldsymbol{V})^t$ and $\boldsymbol{A_2} = \frac{d\boldsymbol{A_1}}{dt} + \boldsymbol{A_1}(\nabla \boldsymbol{V}) + (\nabla \boldsymbol{V})^t\boldsymbol{A_1}$.

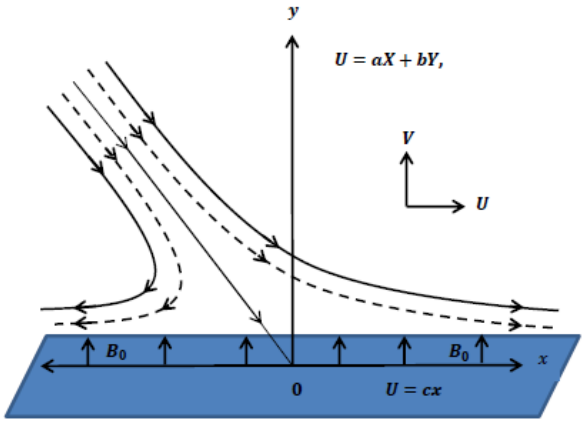

Fig (6.1): Non-dimensional description of the problem

The equations which govern the flow problem are [14]

$$\frac{\partial u^*}{\partial x^*} + \frac{\partial v^*}{\partial y^*} = 0 \tag{6.1}$$

$$u^*\frac{\partial u^*}{\partial x^*} + v^*\frac{\partial u^*}{\partial y^*} + \frac{1}{\rho}\frac{\partial p^*}{\partial x^*} = \nu\nabla^{*2}u^* + \frac{\alpha_1}{\rho}\left\{\frac{\partial}{\partial x^*}\left[2u^*\frac{\partial^2 u^*}{\partial x^{*2}} + 2v^*\frac{\partial^2 u^*}{\partial x^*\partial y^*} + 4\left(\frac{\partial u^*}{\partial x^*}\right)^2 + 2\frac{\partial v^*}{\partial x^*}\left(\frac{\partial u^*}{\partial y^*} + \frac{\partial v^*}{\partial x^*}\right)\right] + \frac{\partial}{\partial y^*}\left[\left(u^*\frac{\partial}{\partial x^*} + v^*\frac{\partial}{\partial y^*}\right)\left(\frac{\partial u^*}{\partial y^*} + \frac{\partial v^*}{\partial x^*}\right) + 2\frac{\partial u^*}{\partial x^*}\frac{\partial u^*}{\partial y^*} + 2\frac{\partial v^*}{\partial x^*}\frac{\partial v^*}{\partial y^*}\right]\right\} + \frac{\alpha_2}{\rho}\frac{\partial}{\partial x^*}\left[4\left(\frac{\partial u^*}{\partial x^*}\right)^2 + \left(\frac{\partial u^*}{\partial y^*} + \frac{\partial v^*}{\partial x^*}\right)^2\right] - \frac{\sigma}{\rho}B_0^2u^* \tag{6.2}$$

$$u^*\frac{\partial v^*}{\partial x^*} + v^*\frac{\partial v^*}{\partial y^*} + \frac{1}{\rho}\frac{\partial p^*}{\partial y^*} = \nu\nabla^{*2}v^* + \frac{\alpha_1}{\rho}\left\{\frac{\partial}{\partial x^*}\left[\left(u^*\frac{\partial}{\partial x^*} + v^*\frac{\partial}{\partial y^*}\right)\left(\frac{\partial u^*}{\partial y^*} + \frac{\partial v^*}{\partial x^*}\right) + 2\frac{\partial u^*}{\partial x^*}\frac{\partial u^*}{\partial y^*} + 2\frac{\partial v^*}{\partial x^*}\frac{\partial v^*}{\partial y^*}\right] + \frac{\partial}{\partial y^*}\left[2u^*\frac{\partial^2 v^*}{\partial x^*\partial y^*} + 4\left(\frac{\partial v^*}{\partial y^*}\right)^2 + 2v^*\frac{\partial^2 v^*}{\partial x^{*2}} + 2\frac{\partial u^*}{\partial y^*}\left(\frac{\partial u^*}{\partial y^*} + \frac{\partial v^*}{\partial x^*}\right)\right]\right\} + \frac{\alpha_2}{\rho}\frac{\partial}{\partial y^*}\left[4\left(\frac{\partial v^*}{\partial y^*}\right)^2 +$$

$$\left(\frac{\partial u^*}{\partial y^*}+\frac{\partial v^*}{\partial x^*}\right)^2\Bigg] \tag{6.3}$$

$$u^*\frac{\partial T^*}{\partial x^*}+v^*\frac{\partial T^*}{\partial y^*}=\alpha^*\nabla^{*2}T^*+\frac{DK_T}{C_sC_p}\nabla^{*2}C^*, \tag{6.4}$$

$$u^*\frac{\partial C^*}{\partial x^*}+v^*\frac{\partial C^*}{\partial y^*}=D\nabla^{*2}C^*+\frac{DK_T}{T_m}\nabla^{*2}T^*. \tag{6.5}$$

where u^*, v^* are x and y components of the velocity respectively, T^* is the temperature, C^* is the concentration, D is the mass diffusivity, ν is the effective kinematic viscosity, K_T is the thermal diffusion, C_p is the specific heat, C_s is the concentration Susceptibility, B_0 is the constant applied magnetic field, T_m is the fluid mean temperature and $\alpha^*$is the effective thermal diffusivity of the MHD viscoelastic fluid.

The boundary conditions of the problem are [14].

$$u^*=cx^*, v^*=0, -k\frac{\partial T^*}{\partial y^*}=h_f\left(T_f-T^*\right), C^*=C_w \; at \; y^*=0,$$

$$u^*=ax^*+by^*, \; T^*=T_\infty, C^*=C_\infty \; as \; y^*\to 0 \tag{6.6}$$

in which $a, b, c>0$ are all constants having inverse time dimension, h_f is the convective heat transfer coefficient, C_w is the constant concentration at the wall whereas T_∞ , C_∞ are the ambient temperature and concentration respectively.

By applying the similarity transformations [14]

$$x=x^*\sqrt{\frac{c}{\nu}}, y=y^*\sqrt{\frac{c}{\nu}}, u=\frac{1}{\sqrt{\nu c}}u^*,$$

$$v=\frac{1}{\sqrt{\nu c}}v^*, p=\frac{1}{\sqrt{\mu c}}p^*, T=\frac{T^*-T_\infty}{T_f-T_\infty}, C=\frac{C^*-C_\infty}{C_w-C_\infty}. \tag{6.7}$$

Eqs (6.1) $-$ (6.5) give

$$\frac{\partial u}{\partial x}+\frac{\partial v}{\partial y}=0 \tag{6.8}$$

$$u\frac{\partial u}{\partial x}+v\frac{\partial u}{\partial y}+\frac{\partial p}{\partial x}=\nabla^2u+We\left\{\frac{\partial}{\partial x}\left[2u\frac{\partial^2u}{\partial x^2}+2v\frac{\partial^2u}{\partial x\partial y}+4\left(\frac{\partial u}{\partial x}\right)^2+2\frac{\partial v}{\partial x}\left(\frac{\partial u}{\partial y}+\frac{\partial v}{\partial x}\right)\right]+\right.$$

$$\frac{\partial}{\partial y}\left[\left(u\frac{\partial}{\partial x}+v\frac{\partial}{\partial y}\right)\left(\frac{\partial u}{\partial y}+\frac{\partial v}{\partial x}\right)+2\frac{\partial u}{\partial x}\frac{\partial u}{\partial y}+2\frac{\partial v}{\partial x}\frac{\partial v}{\partial y}\right]\Big\}+\lambda_m\frac{\partial}{\partial x}\left[4\left(\frac{\partial u}{\partial x}\right)^2+\left(\frac{\partial u}{\partial y}+\frac{\partial v}{\partial x}\right)^2\right]-M^2u \quad (6.9)$$

$$u\frac{\partial v}{\partial x}+v\frac{\partial v}{\partial y}+\frac{\partial p}{\partial y}=\nabla^2 v+We\Big\{\frac{\partial}{\partial x}\left[\left(u\frac{\partial}{\partial x}+v\frac{\partial}{\partial y}\right)\left(\frac{\partial u}{\partial y}+\frac{\partial v}{\partial x}\right)+2\frac{\partial u}{\partial x}\frac{\partial u}{\partial y}+2\frac{\partial v}{\partial x}\frac{\partial v}{\partial y}\right]+\frac{\partial}{\partial y}\Big[2v\frac{\partial^2 v}{\partial x^2}+$$

$$2u\frac{\partial^2 v}{\partial x\partial y}+4\left(\frac{\partial v}{\partial y}\right)^2+2\frac{\partial u}{\partial y}\left(\frac{\partial u}{\partial y}+\frac{\partial v}{\partial x}\right)\Big]\Big\}+\lambda_m\frac{\partial}{\partial y}\left[4\left(\frac{\partial v}{\partial y}\right)^2+\left(\frac{\partial u}{\partial y}+\frac{\partial v}{\partial x}\right)^2\right] \quad (6.10)$$

$$u\frac{\partial T}{\partial x}+v\frac{\partial T}{\partial y}=\frac{1}{Pr}\nabla^2 T+D_f\nabla^2 C, \quad (6.11)$$

$$u\frac{\partial C}{\partial x}+v\frac{\partial C}{\partial y}=\frac{1}{Sc}\nabla^2 C+S_r\nabla^2 T. \quad (6.12)$$

where $We=\frac{\alpha_1 c}{\rho\nu}$ is the Weissenberg number, $M=B_0\sqrt{\frac{\sigma}{\rho c}}$ is the Hartman number, $Pr=\frac{\mu C_p}{k}$ is the Prandtl number, $S_r=\frac{DK_T}{\nu T_m}\frac{T_f-T_\infty}{C_w-C_\infty}$ is the Soret number, $D_f=\frac{DK_T}{\nu C_s C_p}\frac{C_w-C_\infty}{T_f-T_\infty}$ is the Dufour number, $Sc=\frac{\nu}{D}$ is the Schmidt number, $Bi=\frac{h_f}{k}\sqrt{\frac{\nu}{c}}$ is the Biot number and $\lambda_m=\frac{\alpha_2 c}{\rho\nu}$.

Introducing the stream function relations

$$u=\frac{\partial\psi}{\partial y}, v=-\frac{\partial\psi}{\partial x}. \quad (6.13)$$

Using Eq (6.13), Eqs (6.8) $-$ (6.12) can be written in terms of stream function as

$$\nabla^4\psi-We\frac{\partial(\psi,\nabla^4\psi)}{\partial(x,y)}+\frac{\partial(\psi,\nabla^2\psi)}{\partial(x,y)}-M^2\frac{\partial\psi}{\partial y}=0, \quad (6.14)$$

$$\frac{\partial\psi}{\partial y}\frac{\partial T}{\partial x}-\frac{\partial\psi}{\partial x}\frac{\partial T}{\partial y}=\frac{1}{Pr}\nabla^2 T+D_f\nabla^2 C, \quad (6.15)$$

$$\frac{\partial\psi}{\partial y}\frac{\partial C}{\partial x}-\frac{\partial\psi}{\partial x}\frac{\partial C}{\partial y}=\frac{1}{Sc}\nabla^2 C+S_r\nabla^2 T. \quad (6.16)$$

We search for solution of Eqs (6.14) $-$ (6.16) of the form

$$\psi(x,y)=xf(y)+g(y), T=\theta(y), C=\phi(y), \quad (6.17)$$

This gives

$$f'''-f'^2+ff''-We\left(ff^{iv}+f''^2-2f'f'''\right)-M^2f'+C_1=0, \quad (6.18)$$

$$g''' - f'g' + fg'' - We\left(fg^{iv} + f''g'' - f'g''' - f'''g'\right) - M^2g' + C_2 = 0, \quad (6.19)$$

$$\theta'' + Pr\left(f\theta' + D_f\phi''\right) = 0, \quad (6.20)$$

$$\phi'' + Sc(f\phi' + S_r\theta'') = 0. \quad (6.21)$$

Along with the transformed boundary conditions

$$f(0) = 0, f'(0) = 1, f'(\infty) = \frac{a}{c}, g(0) = 0, g'(0) = 0, g''(\infty) = \gamma_1,$$

$$\theta'(0) = -Bi\left(1 - \theta(0)\right), \theta(\infty) = 0, \phi(0) = 1, \phi(\infty) = 0. \quad (6.22)$$

Since $f(y) = \frac{a}{c}y + A$ at $y \to \infty$, in which A signifies the boundary layer displacement constant. Substituting Eq (6.22) in above, we get $C_1 = M^2(\frac{a}{c}) + (\frac{a}{c})^2$ and $C_2 = -A\gamma_1$.

Introducing

$$g'(y) = \gamma_1 h(y). \quad (6.23)$$

Equations (6.18) $-$ (6.22) take the form

$$f''' - f'^2 + ff'' - We\left(ff^{iv} + f''^2 - 2f'f'''\right) + M^2((\frac{a}{c}) - f') + (\frac{a}{c})^2 = 0, \quad (6.24)$$

$$h'' - f'h + fh' - We(fh''' + f''h' - f'h'' - f'''h) - M^2h - A = 0, \quad (6.25)$$

$$\theta'' + Pr\left(f\theta' + D_f\phi''\right) = 0, \quad (6.26)$$

$$\phi'' + Sc(f\phi' + S_r\theta'') = 0, \quad (6.27)$$

$$f(0) = 0, f'(0) = 1, f'(\infty) = \frac{a}{c}, h(0) = 0, h'(\infty) = 1,$$

$$\theta'(0) = -Bi\left(1 - \theta(0)\right), \theta(\infty) = 0, \phi(0) = 1, \phi(\infty) = 0, \quad (6.28)$$

The local shear stress, local heat flux and local mass flux at the stretching convective surface, are given as [14]

$$\tau_w = [\frac{\partial^2\psi}{\partial y^2} - \frac{\partial^2\psi}{\partial x^2} + We\{\left(\frac{\partial^3\psi}{\partial y^2\partial x} - \frac{\partial^3\psi}{\partial x^3}\right)\frac{\partial\psi}{\partial y} - \left(\frac{\partial^3\psi}{\partial y^3} - \frac{\partial^3\psi}{\partial x^2\partial y}\right)\frac{\partial\psi}{\partial x} + 2\frac{\partial^2\psi}{\partial y\partial x}\frac{\partial^2\psi}{\partial y^2} + 2\frac{\partial^2\psi}{\partial y\partial x}\frac{\partial^2\psi}{\partial x^2}\}]_{y=0},$$

$$q_w = -k\left(\frac{\partial T}{\partial y}\right)_{y=0}, q_m = -j\left(\frac{\partial C}{\partial y}\right)_{y=0}. \quad (6.29)$$

Employing Eq (6.17), above quantities finally take the form as,

$$\tau_w = x\{(1+3We)\}f''(0) + \{(1+2We)\}\gamma_1 h'(0),$$

$$q_w = -\theta'(0),\ q_m = -\phi'(0). \tag{6.30}$$

The point of stagnation x_s can be attained by zero wall shear stress, i.e.

$$x_s = \frac{-\{(1+2We)\}\gamma_1 h'(0)}{\{(1+3We)\}f''(0)} \tag{6.31}$$

6.3 Numerical Solution

The systems of equations (6.24) – (6.28) are solved numerically utilizing midpoint integration scheme coupled with Richardson's extrapolation. Midpoint technique is an extremely stable computational process which when merged with Richardson's extrapolation develops highly accurate grid independent solutions. The problem of semi-infinite domain $[0, \infty)$ is generously transformed into such appropriate finite domain of y i.e. $[0, y_\infty)$ where y_∞ should be so large that the numerical solutions would approach the asymptotic behaviour at the infinite boundaries. A mesh size of $\Delta h = 0.001$ has been selected to achieve convergence up to 10^{-6} in our computations. Numerical computations are performed on a symbolic highly efficient software Maple.

6.4 Results and Discussion

This segment illuminates the flow behaviour against pertinent non-dimensional parameters appearing in the governing system. Figs. (6.2)– (6.19) are plotted to express the velocity, temperature and concentration profile of the system. Stream line patterns are sketched to find out

the impact of applied magnetic force through parameter M on oblique flow. Figs (6.2) – (6.5) are portrayed to find out the effect of magnetic field M, stretching ratio a/c and Weissenberg number We on velocity profiles $f'(y)$ and $h'(y)$. It is found that the Hartman number M causes to decrease both types of velocity profiles, which is obvious from Figs (6.2) and (6.4). We can notice from Fig (6.2) that when $a/c < 1$, increase in magnetic field M causes to decrease the normal component of the velocity $f'(y)$. This is because Lorentz force which is developed through the application of uniform magnetic strength executes a retarding force on velocity profiles and hence causes a reduction in the velocities. On the other hand, it is quite evident that stretching ratio a/c and viscoelastic parameter We has positive impact on the velocities. From Fig (6.3), we observe that when the magnetic field parameter M is kept fixed and as the viscoelastic parameter We increases, normal component of velocity $f'(y)$ also increases. Similar kind of behaviour is noticed in the case of tangential component of velocity $h'(y)$ (see Fig (6.5)). The behaviour of temperature profile $\theta(y)$ against certain non-dimensional parameters is expressed through Figs. (6.6) – (6.11). Fig (6.6) exhibit that with an increase in magnetic field M, temperature profile $\theta(y)$ rises extensively. This behaviour is observed because of the resistive force which consequently heats up the fluid and rises its temperature. On the other hand, it is observed from Fig (6.7) that increasing the viscoelastic parameter We results in an increase in the temperature profile $\theta(y)$. From Fig (6.8), it is noticed that when Biot number Bi increases, temperature profile $\theta(y)$ also increases. This is because Biot number Bi involves the heat transfer coefficient so an increase in Biot number leads to an increase in heat transfer coefficient which consequently enhances the fluid temperature $\theta(y)$. Effects of Soret number S_r and Dufour number D_f on the temperature profile $\theta(y)$ are depicted through Figs (6.9) and (6.10). These parameters have shown an opposite effect on temperature profile $\theta(y)$ for fix

values of Hartman number M. It is found that with an increase in Soret number S_r, temperature profile $\theta(y)$ decreases near the wall (see Fig (6.9)). Soret number is the ratio of temperature to the concentration difference so an increase in it leads to a higher temperature difference at the wall and the ambient fluid temperature compared to the corresponding concentration difference, due to which temperature drops down. Similarly we can observe from Fig (6.10) that Dufour number D_f causes to increase temperature profile $\theta(y)$ significantly. Dufour number is the ratio of concentration to temperature difference. Higher values of Dufour number D_f implies lower temperature difference, which results in an enhancement in the temperature profile $\theta(y)$. Similarly, Fig (6.11) reveals that when we increase the value of Schmidt number Sc, temperature rises under the influence of uniform magnetic force. The influence of important parameters like magnetic field parameter M, viscoelastic parameter We, Biot number Bi, Dufour number D_f, Soret number S_r and Schmidt number Sc on $\Phi(y)$ is presented through Figs (6.12) – (6.17). One can perceive from Fig (6.12) that magnetic field parameter M increases the concentration profile $\Phi(y)$. Increasing the viscoelastic parameter We leads to a decrease in concentration profile $\Phi(y)$which is visible from Fig (6.13). Effect of Biot number Bi on the concentration profile $\Phi(y)$ is depicted through Fig (6.14). We can see that concentration profile $\Phi(y)$ is increasing with Biot number Bi. It is interesting to note here that Biot number has similar kind of influence on the concentration profile $\Phi(y)$, which it have on the temperature profile $\theta(y)$ but the effects are more prominent in temperature profile $\theta(y)$ when compared with the concentration profile $\Phi(y)$. Impact of pertinent parameters such as Soret S_r and Dufour number D_f on the concentration profile $\Phi(y)$ is presented through Figs (6.15) and (6.16). Both these parameters have opposite influence on the concentration profile $\Phi(y)$ near the wall. Similarly, we can notice from Fig (6.17) that for fixed magnetic field, concentration profile

$\Phi(y)$ drops with Schmidt number Sc. Stream line patterns for oblique flow under applied magnetic field are traced through Figs (6.18) and (6.19). It is easily detectable from these stream lines that the magnetic field parameter M caused the obliqueness of the flow to slightly straighten up. This is because normal shear flow is disturbed through the application of magnetic force of uniform strength. Comparison of present study with the previously existing literature when ($M = 0$) is given in $Table$ 6.1. The computed results are found to be in decent agreement with those given by Pop et al [14]. Variations of local skin frictions co-efficient $f''(0)$ and $h'(0)$, local heat flux $-\theta'(0)$ and local mass flux at the surface $-\Phi'(0)$ against magnetic field parameter M, stretching ratio a/c and Weissenberg number We are presented through $Table$ 6.2. It is found that normal component of the local skin frictions co-efficient $f''(0)$ as well as tangential component of the local skin friction co-efficient $h'(0)$ decreases with an increase in stretching ratio a/c. An increase in stretching parameter consequently favours the stretch flow which ultimately reduces the skin friction at the wall. On the other hand it is also noticed that heat flux at the convective surface as well as the local mass flux increases when stretching ratio $\frac{a}{c}$ is increased. This is in good agreement with the non-dimensional situation because increasing the stretching ratio a/c decreases the corresponding surface temperature due to which heat diffuses quickly at the surface and the corresponding mass flux increases. Viscoelastic parameter We has an opposite influence on normal skin friction co-efficient $f''(0)$ and tangential skin-frictions $h'(0)$ respectively. It is observed that increasing the viscoelasticity parameter We, causes an increase in local heat flux $-\theta'(0)$ and mass flux $-\Phi'(0)$. The effect of magnetic field M on normal and tangential skin friction co-efficient, i.e. $f''(0)$ and $h'(0)$ is not very similar. The obtained numerical data indicates that with increasing the magnetic field strength through parameter M, normal component of the skin friction $f''(0)$ rises, while

tangential skin friction $h'(0)$ gradually drops. As we have noticed earlier that magnetic field M raises the fluid temperature and concentration profiles so consequently local heat and mass flux at the wall decays which is quite obvious from the obtained numerical results in $Table$ 6.2. $Table$ 6.3 is presented to find out the influence of relevant non-dimensional parameters such as Soret number S_r, Prandtl number Pr, Dufour number D_f, Schmidt number Sc and Biot number Bi on local heat $-\theta'(0)$ as well as mass flux at the surface $-\Phi'(0)$. One can easily observe from the tabulated results that Biot number Bi, Soret number S_r and Prandtl number Pr caused an increase in the local heat flux$-\theta'(0)$, while they lead to a reduction in the local mass flux$-\Phi'(0)$. Similarly for large values of Dufour number D_f and Schmidt number Sc, local heat flux rate $-\theta'(0)$ declines whereas local mass flux rate $-\Phi'(0)$ at the stretching convective surface improves in a quantitative sense.

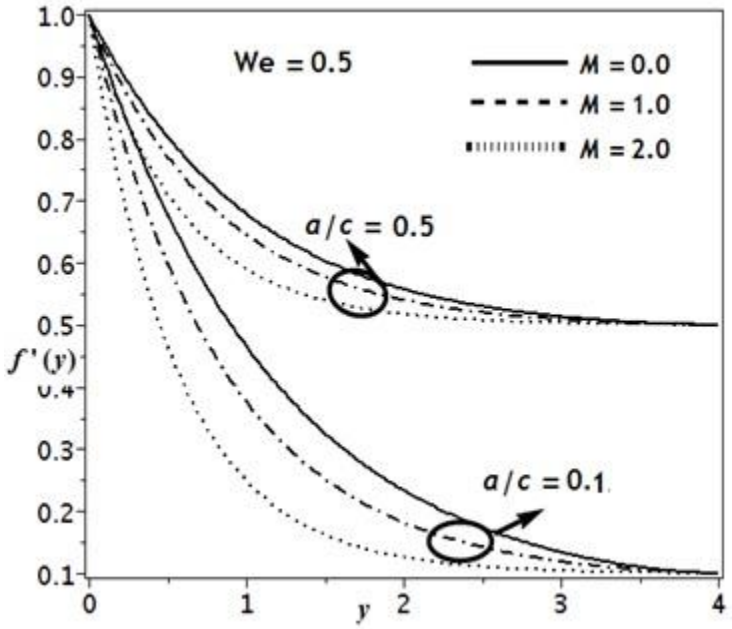

Fig (6.2): Velocity profile $f'(y)$ against M.

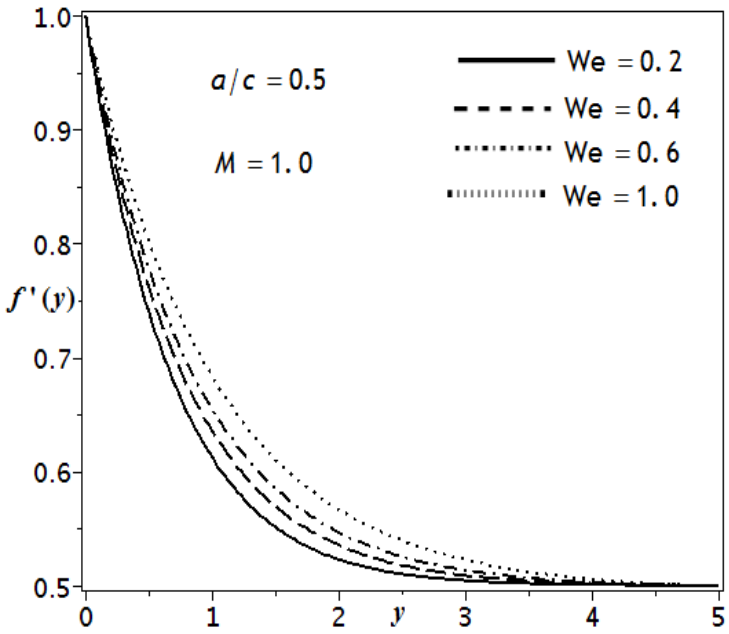

Fig (6.3): Velocity profile $f'(y)$ against We.

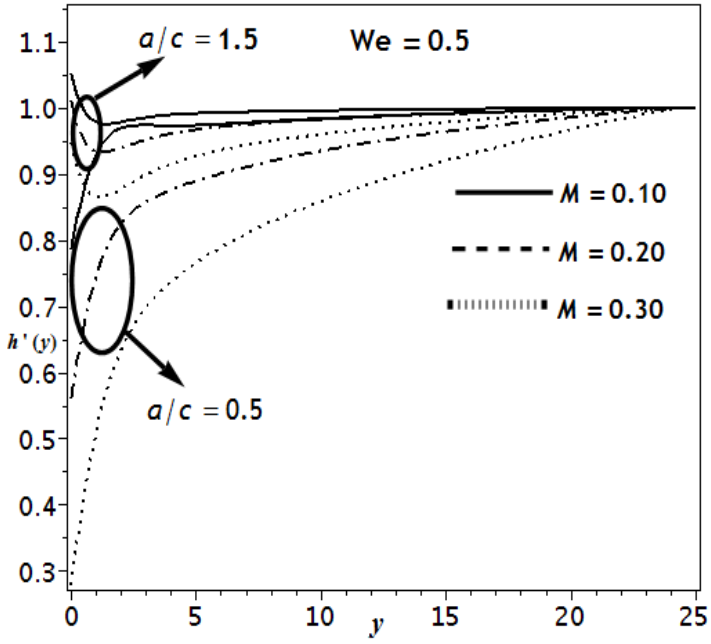

Fig (6.4): Velocity profile $h'(y)$ against M.

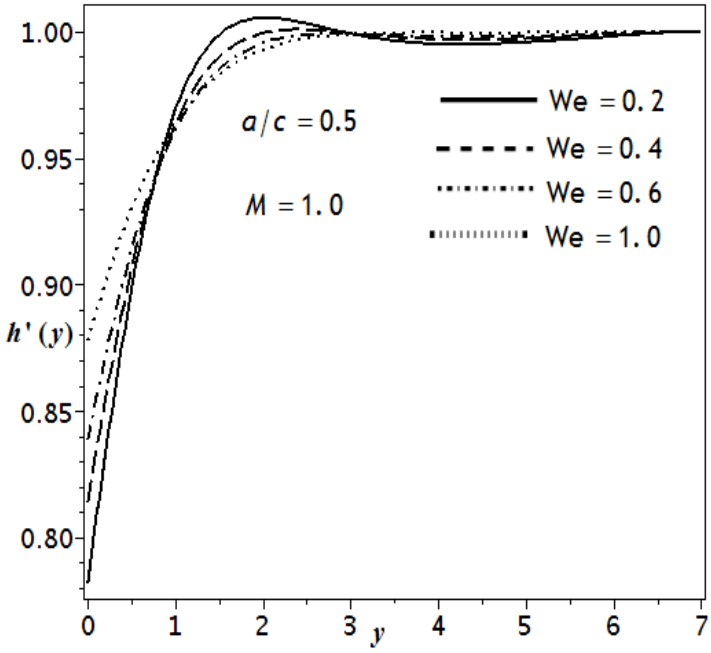

Fig (6.5): Velocity profile $h'(y)$ against We.

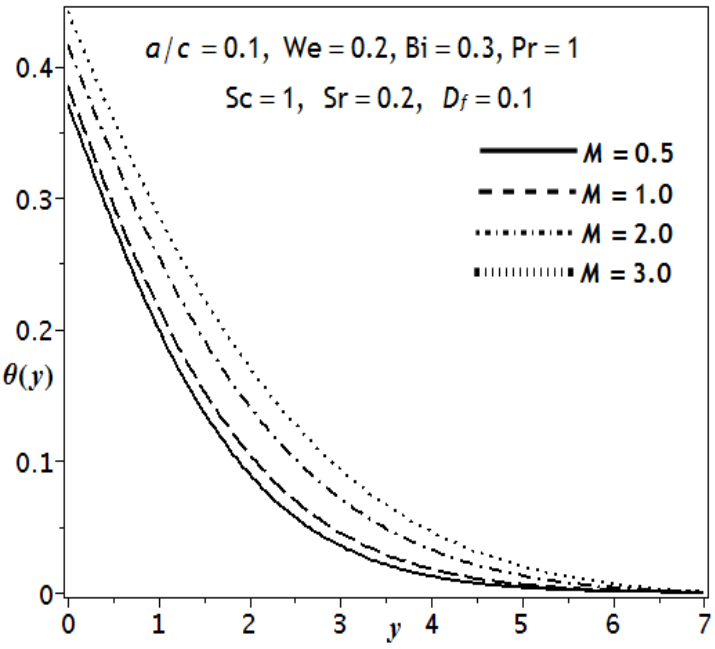

Fig(6.6): Temperature profile $\theta(y)$ against M.

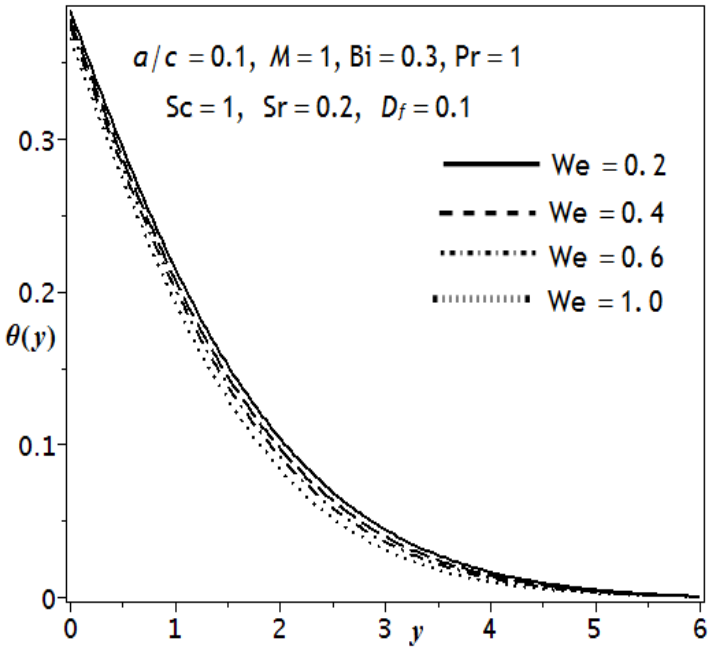

Fig(6.7): Temperature profile $\theta(y)$ against We.

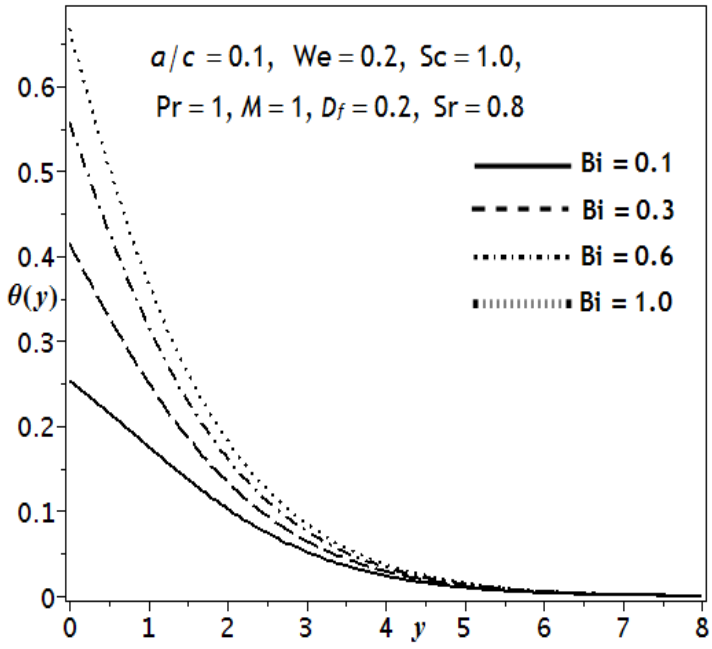

Fig(6.8): Temperature profile $\theta(y)$ against Bi.

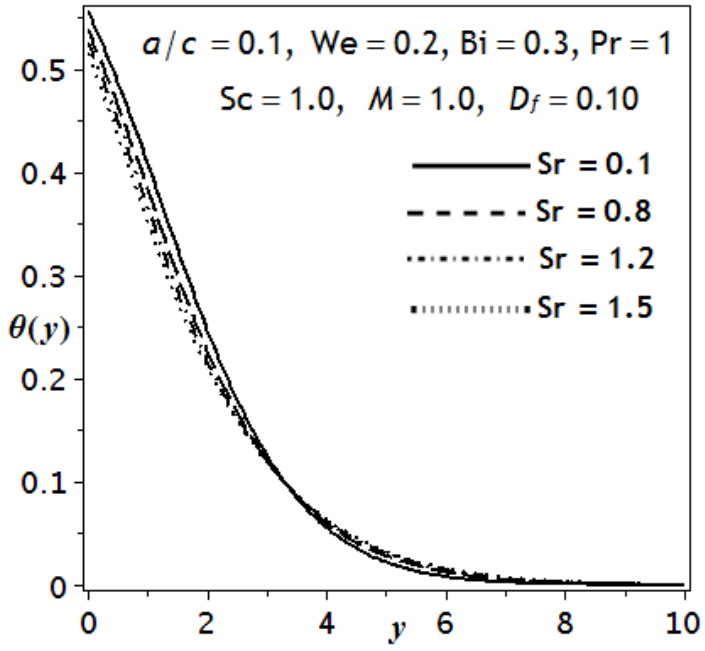

Fig(6.9): Temperature profile $\theta(y)$ against S_r.

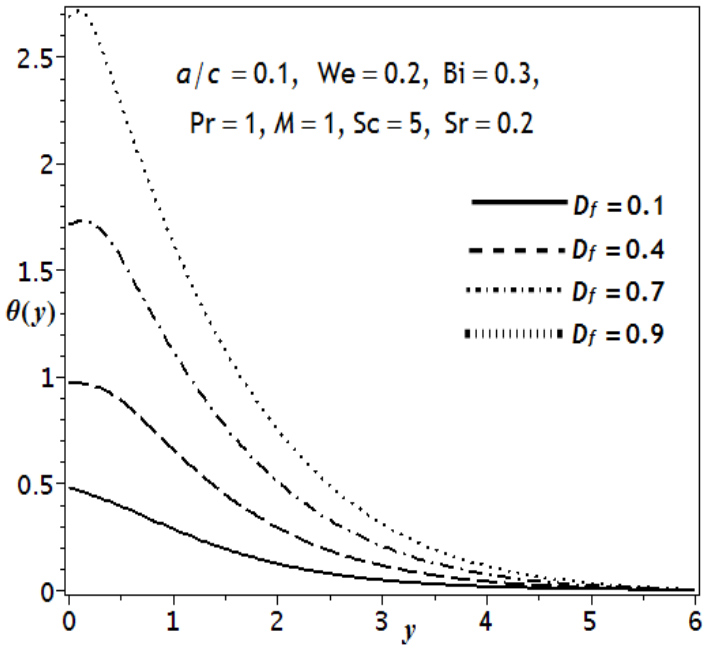

Fig(6.10): Temperature profile $\theta(y)$ against D_f.

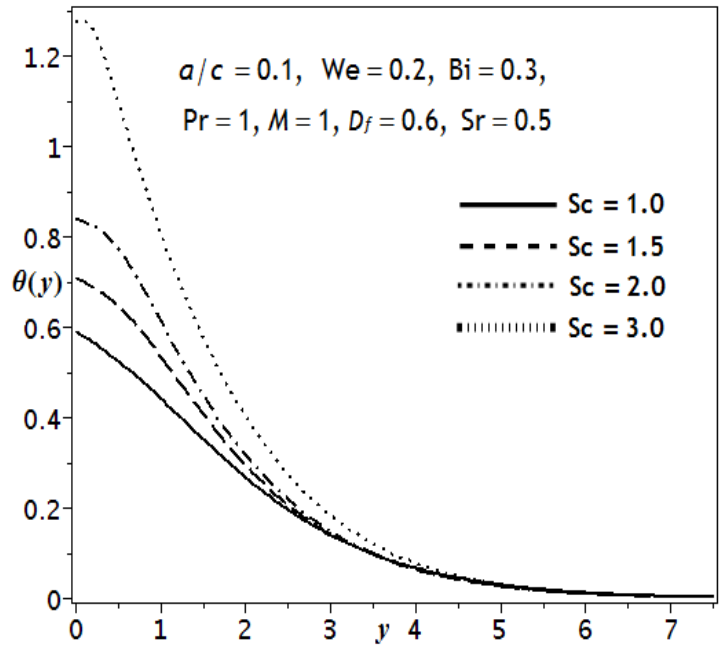

Fig(6.11): Temperature profile $\theta(y)$ against Sc.

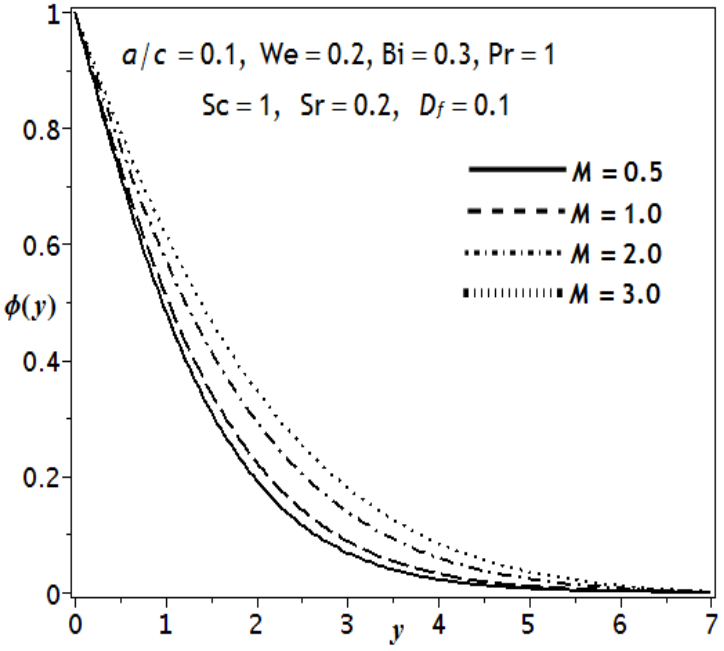

Fig (6.12): Concentration profile $\phi(y)$ against M.

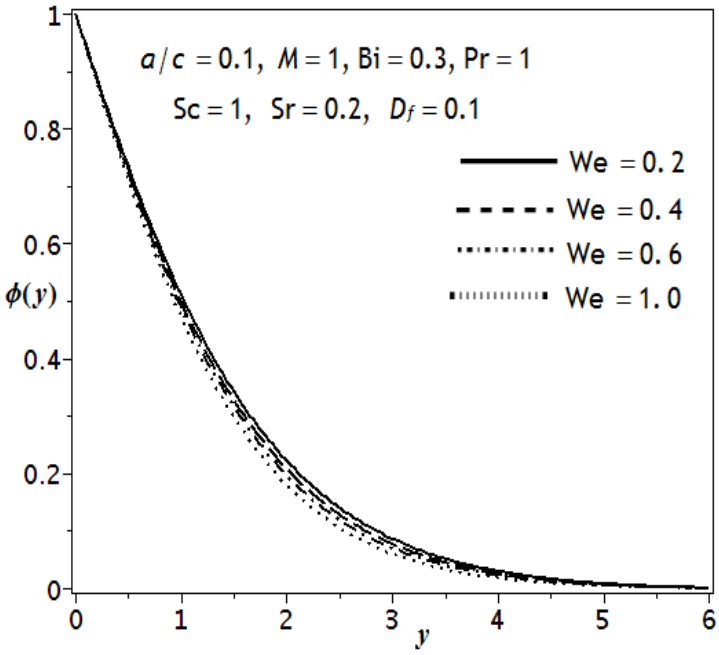

Fig (6.13): Concentration profile $\phi(y)$ against We.

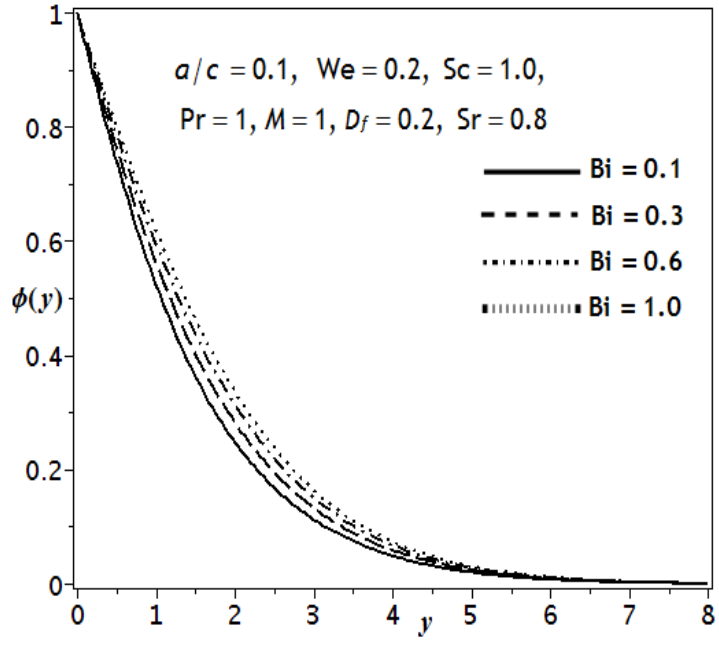

Fig (6.14): Concentration profile $\phi(y)$ against Bi.

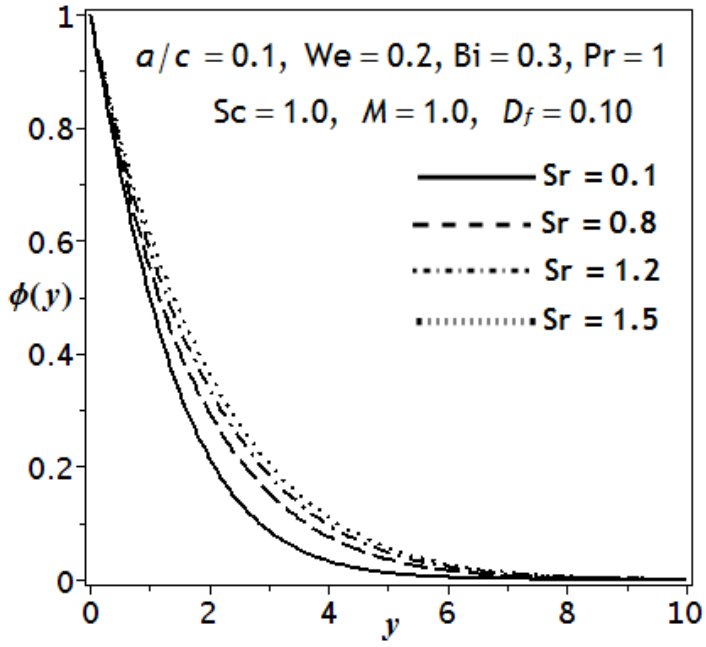

Fig (6.15): Concentration profile $\phi(y)$ against S_r.

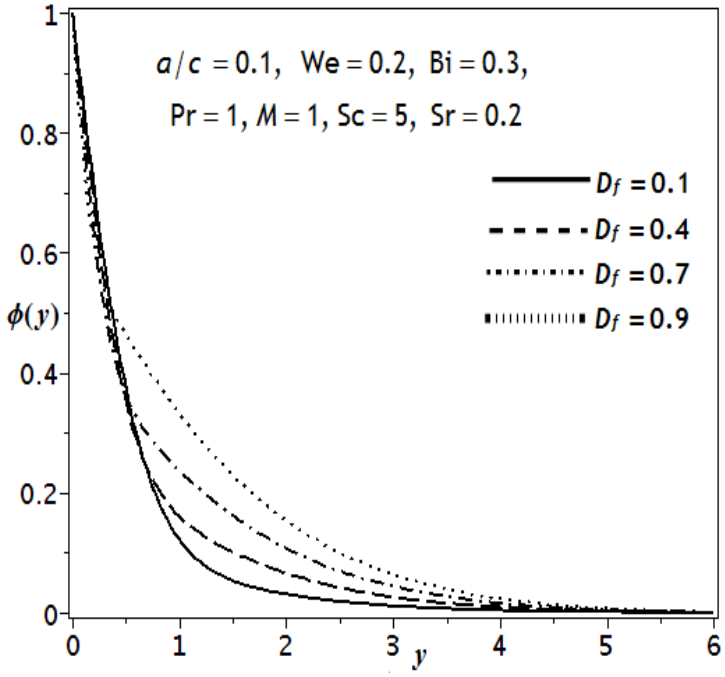

Fig (6.16): Concentration profile $\phi(y)$ against D_f.

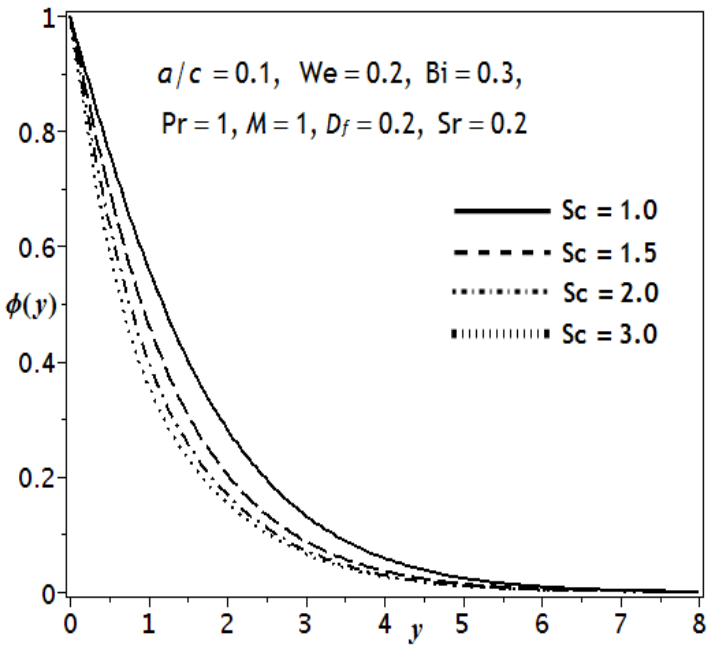

Fig (6.17): Concentration profile $\phi(y)$ against Sc.

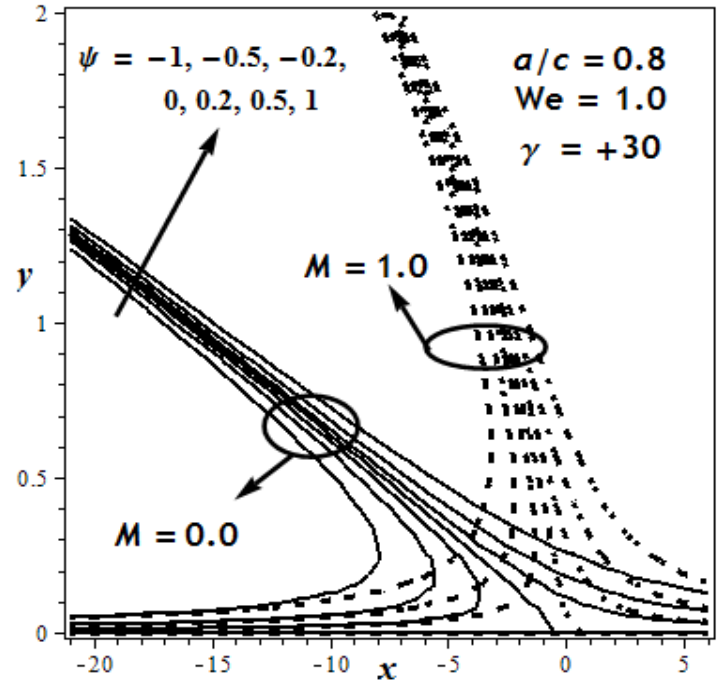

Fig (6.18): Stream line flow pattern for $M = 0, 1$ and $\gamma_1 = +30$.

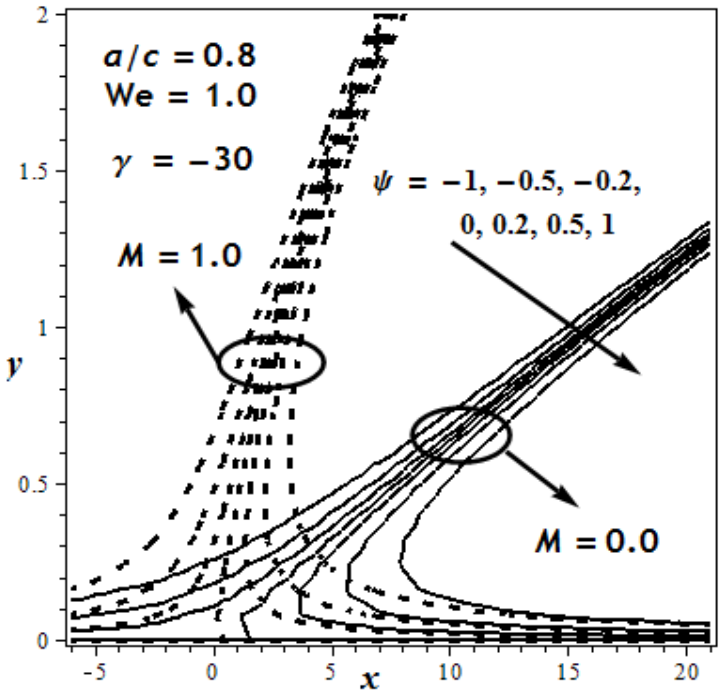

Fig (6.19): Stream line flow pattern for $M = 0, 1$ and $\gamma_1 = -30$.

	$f''(0)$		$h'(0)$		$-\theta'(0)$	
a/c	Present	Pop et al [14]	Present	Pop et al [14]	Present	Pop et al [14]
0.1	−0.87659	−0.87659	0.36384	0.36206	0.61941	0.61941
0.3	−0.75114	−0.75114	0.67908	0.67763	0.66189	0.66189
0.8	−0.24971	−0.24971	0.95292	0.95176	0.76193	0.76193
1.0	0.0	0.0	1.0	1.0	0.79788	0.79788
2.0	1.48903	1.48903	1.10357	1.10251	0.95031	0.95031
3.0	3.21326	3.21326	1.13120	1.13014	1.07196	1.07196

Table 6.1**:** Comparison with the existing literature when $We = 0.2, Bi = \infty$.

a/c	We	M	A	$-f''(0)$	$-h'(0)$	$-\theta'(0)$	$-\Phi'(0)$
0.1	0.1	1.0	0.63371	1.25212	0.63418	0.17081	0.54045
0.3			0.45450	1.02813	0.42135	0.18025	0.61166
0.5			0.30505	0.76872	0.25867	0.18651	0.66824
0.1	0.1	1.0	0.63371	1.25212	0.63418	0.17081	0.54045
	0.2		0.66831	1.19248	0.66801	0.17192	0.54960
	0.5		0.76322	1.05332	0.74350	0.17460	0.57199
0.1	0.1	1.0	0.63371	1.25212	0.63418	0.17081	0.54045
		2.0	0.41637	1.93492	0.20630	0.16133	0.46466
		4.0	0.22985	3.52939	0.05689	0.14888	0.37531

Table 6.2: Numerical values of local skin frictions and heat and mass flux against $\frac{a}{c}, We$ and M.

Sr	Df	Pr	Sc	Bi	$-\theta'(0)$	$-\Phi'(0)$
0.1	0.2	1.0	1.0	0.3	0.17025	0.55080
0.3					0.17137	0.52997
0.5					0.17253	0.50860
0.2	0.1	1.0	1.0	0.3	0.18322	0.53783
	0.3				0.15822	0.54312
	0.5				0.13253	0.54861
0.1	0.1	1.0	1.0	0.3	0.18322	0.53783
		7.0			0.23942	0.52371
		10			0.24554	0.52165
0.1	0.1	1.0	1.0	0.3	0.18322	0.53783
			3.0		0.16713	1.08419
			5.0		0.15453	1.48560
0.1	0.1	1.0	1.0	0.3	0.18322	0.53783
				0.7	0.29255	0.52338
				1.0	0.33792	0.51738

Table 6.3: Numerical values of local heat and mass flux against Sr, Df, Pr, Sc and Bi.

6.5 Concluding Remarks

A theoretical study is conducted to discuss the MHD oblique viscoelastic fluid over a stretching convective surface. The governing system of equations is integrated by midpoint scheme along with Richardson's extrapolation. Numerical quantities such as local shear stress, local heat as well as mass flux are tabulated.

The key points of study can be stated as.

i. Impact of uniform magnetic strength through non-dimensional parameter M on normal and tangential velocity components has been observed similar. I.e. it causes a reduction in both types of velocities.

ii. Both types of velocities exhibit an increasing behaviour with increasing stretching ratio a/c and viscoelastic parameter We.

iii. Temperature and concentration profiles substantially grow with an enhancement in magnetic field parameter M.

iv. Soret and Dufour numbers has an opposite impact on temperature as well as concentration profile for fixed magnetic strength.

v. Application of magnetic field through Hartman number M leads to a disturbance in the obliqueness of the flow.

Chapter 7

Numerical investigation on MHD oblique flow of Walter's B nano fluid over a convective surface

7.1 Introduction

The objective of this chapter is to numerically investigate the oblique flow of a Walter-B nano fluid over a convective surface. Effects of transversely applied magnetic field are also taken into account. The governing system is presented in the form of coupled differential equations by means of suitable similarity transformations which are then solved by using Spectral Quasilinearization Method (QLM) and the Spectral Local Linearization Method (LLM). The results for velocities temperature as well as nano particle concentration are plotted against pertinent flow parameters. It is found that applied magnetic field M has opposite influence on normal and tangential components of local shear stress and it decays the local heat flux and mass flux rate at the stretching convective surface. Thermophoresis and Brownian diffusion effects on the local heat and mass flux rate are found to be non-similar in a quantitative sense. In order to signify the validity of current numerical scheme, a remarkable agreement is presented with the previous literature for the limiting case.

7.2 Mathematical Formulation

Let us consider oblique flow of a Walter-B nanofluid which strikes a convective surface. A magnetic field of uniform strength B_0 is executed in the direction of $y-axis$. Moreover, surface is kept stretched by applying two equal and opposite forces making the origin fixed (as shown in Fig (7.1)). We further assume that the surface has convective fluid temperature T_f and uniform ambient temperature T_∞ (here $(T_f \rangle T_\infty)$). The constitutive equations for the present problem are the same as $(2.1) - (2.6)$. The stress tensor τ for Walter B type fluid can be written as [16]

$$\boldsymbol{\tau} = 2\mu\boldsymbol{D} - 2k_0\frac{\delta \boldsymbol{D}}{\delta t} \qquad (7.1)$$

Where k_0 the short memory co-efficient, $\boldsymbol{D}$ is the deformation rate tensor and $\frac{\delta \boldsymbol{d}}{\delta t}$ is upper convected derivative of a tensor and can be obtained by $\frac{\delta \boldsymbol{D}}{\delta t} = \frac{\partial \boldsymbol{D}}{\partial t} + (\boldsymbol{V}.\nabla)\boldsymbol{D} - \nabla \boldsymbol{V}.\boldsymbol{D} - \boldsymbol{D}.\nabla \boldsymbol{V}^{\,t}$

Using the constitutive equations $(2.1) - (2.6)$ and the extra stress tensor for Walter B type fluid from equation (7.1), the flow governing equations are given as [40]

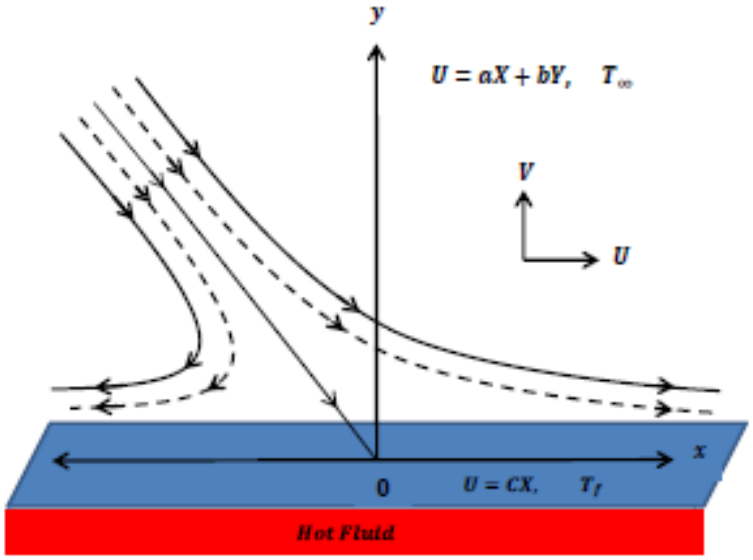

Fig (7.1): A non-dimensional description of the problem

$$\frac{\partial u^*}{\partial x^*}+\frac{\partial v^*}{\partial y^*}=0 \tag{7.2}$$

$$u^*\frac{\partial u^*}{\partial x^*}+v^*\frac{\partial u^*}{\partial y^*}+\frac{1}{\rho_f}\frac{\partial p^*}{\partial x^*}=\nu\nabla^{*2}u^*-\frac{k_0}{\rho_f}\left\{\left(u^*\frac{\partial}{\partial x^*}+v^*\frac{\partial}{\partial y^*}\right)\nabla^{*2}u^*-\frac{\partial u^*}{\partial x^*}\nabla^{*2}u^*-\frac{\partial u^*}{\partial y^*}\nabla^{*2}v^*-$$

$$2\left[\frac{\partial u^*}{\partial x^*}\frac{\partial^2 u^*}{\partial x^{*2}}+\frac{\partial v^*}{\partial y^*}\frac{\partial^2 u^*}{\partial y^{*2}}+\left(\frac{\partial u^*}{\partial y^*}+\frac{\partial v^*}{\partial x^*}\right)\frac{\partial^2 u^*}{\partial x^*\partial y^*}\right]\right\}-\frac{\sigma}{\rho_f}B_0^2u^* \tag{7.3}$$

$$u^*\frac{\partial v^*}{\partial x^*}+v^*\frac{\partial v^*}{\partial y^*}+\frac{1}{\rho_f}\frac{\partial p^*}{\partial y^*}=\nu\nabla^{*2}v^*-\frac{k_0}{\rho_f}\left\{\left(u^*\frac{\partial}{\partial x^*}+v^*\frac{\partial}{\partial y^*}\right)\nabla^{*2}v^*-\frac{\partial v^*}{\partial x^*}\nabla^{*2}u^*-\frac{\partial v^*}{\partial y^*}\nabla^{*2}v^*-$$

$$2\left[\frac{\partial u^*}{\partial x^*}\frac{\partial^2 v^*}{\partial x^{*2}}+\frac{\partial v^*}{\partial y^*}\frac{\partial^2 v^*}{\partial y^{*2}}+\left(\frac{\partial u^*}{\partial y^*}+\frac{\partial v^*}{\partial x^*}\right)\frac{\partial^2 v^*}{\partial x^*\partial y^*}\right]\right\} \tag{7.4}$$

$$u^*\frac{\partial T^*}{\partial x^*}+v^*\frac{\partial T^*}{\partial y^*}=\alpha^*\nabla^{*2}T^*+\frac{(\rho c)_p}{(\rho c)_f}\left(D_B\nabla^*C^*.\nabla^*T^*+\frac{D_T}{T_\infty}\nabla^*T^*.\nabla^*T^*\right), \tag{7.5}$$

$$u^*\frac{\partial C^*}{\partial x^*}+v^*\frac{\partial C^*}{\partial y^*}=D_B\nabla^{*2}C^*+\frac{D_T}{T_\infty}\nabla^{*2}T^*, \tag{7.6}$$

where u^*, v^* are the components of velocity along co-ordinate axis, ν is the effective kinematic viscosity , T^* is the temperature, $C^*$is the concentration, α^* is the effective thermal diffusivity, D_B is the Brownian diffusion co-efficient and D_T is the thermophoresis co-efficient. The appropriate boundary conditions for the problem under consideration are [14].

$$u^*=cx^*,-k\frac{\partial T^*}{\partial y^*}=h_f\left(T_f-T^*\right),C^*=C_w\ at\ y^*=0,$$

$$u^*=ax^*+by^*,\ T^*=T_\infty,C^*=C_\infty\ as\ y^*\to 0 \tag{7.7}$$

in which $a,b,c>0$ are all constants having inverse time dimension, h_f is the convective heat transfer coefficient, C_w is the constant concentration at the wall whereas T_∞ and C_∞ are ambient fluid temperature and concentration.

By applying

$$x=x^*\sqrt{\frac{c}{\nu}},y=y^*\sqrt{\frac{c}{\nu}},u=\frac{1}{\sqrt{\nu c}}u^*,$$

$$v=\frac{1}{\sqrt{\nu c}}v^*,p=\frac{1}{\sqrt{\mu c}}p^*,T=\frac{T^*-T_\infty}{T_f-T_\infty},C=\frac{C^*-C_\infty}{C_w-C_\infty}. \tag{7.8}$$

Eqs (7.2) − (7.6) give

$$\frac{\partial u}{\partial x}+\frac{\partial v}{\partial y}=0 \tag{7.9}$$

$$u\frac{\partial u}{\partial x}+v\frac{\partial u}{\partial y}+\frac{\partial p}{\partial x}=\nabla^2 u-K_w\left\{\left(u\frac{\partial}{\partial x}+v\frac{\partial}{\partial y}\right)\nabla^2 u-\frac{\partial u}{\partial x}\nabla^2 u-\frac{\partial u}{\partial y}\nabla^2 v-2\left[\frac{\partial u}{\partial x}\frac{\partial^2 u}{\partial x^2}+\frac{\partial v}{\partial y}\frac{\partial^2 u}{\partial y^2}+\right.\right.$$

$$\left.\left.\left(\frac{\partial u}{\partial y}+\frac{\partial v}{\partial x}\right)\frac{\partial^2 u}{\partial x\partial y}\right]\right\}-M^2 u \tag{7.10}$$

$$u\frac{\partial v}{\partial x}+v\frac{\partial v}{\partial y}+\frac{\partial p}{\partial y}=\nabla^2 v-K_w\left\{\left(u\frac{\partial}{\partial x}+v\frac{\partial}{\partial y}\right)\nabla^2 v-\frac{\partial v}{\partial x}\nabla^2 u-\frac{\partial v}{\partial y}\nabla^2 v-2\left[\frac{\partial u}{\partial x}\frac{\partial^2 v}{\partial x^2}+\frac{\partial v}{\partial y}\frac{\partial^2 v}{\partial y^2}+\right.\right.$$

$$\left.\left.\left(\frac{\partial u}{\partial y}+\frac{\partial v}{\partial x}\right)\frac{\partial^2 v}{\partial x\partial y}\right]\right\} \tag{7.11}$$

$$Pr\left(u\frac{\partial T}{\partial x}+v\frac{\partial T}{\partial y}\right)=\nabla^2 T+Pr(N_b\nabla C.\nabla T+N_t\nabla T.\nabla T), \tag{7.12}$$

$$Sc\left(u\frac{\partial C}{\partial x}+v\frac{\partial C}{\partial y}\right)=\nabla^2 C+\frac{N_t}{N_b}\nabla^2 T \tag{7.13}$$

Where $K_w=\frac{k_0 c}{\rho\nu}$ is the local Weissenberg number, $M=B_0\sqrt{\frac{\sigma}{\rho c}}$ is the Hartman number, $Pr=\frac{\nu}{\alpha}$ is the Prandtl number, the thermophoresis parameter $N_t=\frac{D_T}{T_\infty}\frac{(\rho c)_p}{(\rho c)_f}\frac{(T_f-T_\infty)}{\nu}$, the Brownian motion parameter $N_b=D_B\frac{(\rho c)_p}{(\rho c)_f}\frac{(C_w-C_\infty)}{\nu}$ and $Sc=\frac{\nu}{D_B}$ is the Schmidt number.

Introducing the stream function relations

$$u=\frac{\partial\psi}{\partial y},v=-\frac{\partial\psi}{\partial x}. \tag{7.14}$$

Eqs (7.9) − (7.13) can be written in terms of stream function as

$$\nabla^4\psi+K_w\frac{\partial(\psi,\nabla^4\psi)}{\partial(x,y)}+\frac{\partial(\psi,\nabla^2\psi)}{\partial(x,y)}-M^2\frac{\partial\psi}{\partial y}=0, \tag{7.15}$$

$$\Pr\left(\frac{\partial\psi}{\partial y}\frac{\partial T}{\partial x}-\frac{\partial\psi}{\partial x}\frac{\partial T}{\partial y}\right)=\nabla^2 T+Pr(N_b\nabla C.\nabla T+N_t\nabla T.\nabla T), \tag{7.16}$$

$$Sc\left(\frac{\partial\psi}{\partial y}\frac{\partial C}{\partial x}-\frac{\partial\psi}{\partial x}\frac{\partial C}{\partial y}\right)=\nabla^2 C+\frac{N_t}{N_b}\nabla^2 T \tag{7.17}$$

We search for solution of Eqs (7.15) − (7.17) of the form

$$\psi(x,y) = xf(y) + g(y), T = \theta(y), C = \phi(y), \tag{7.18}$$

This gives

$$f''' - f'^2 + ff'' + K_w\left(ff^{iv} + f''^2 - 2f'f'''\right) - M^2 f' + C_1 = 0, \tag{7.19}$$

$$g''' - f'g' + fg'' + K_w\left(fg^{iv} + f''g'' - f'g''' - f'''g'\right) - M^2 g' + C_2 = 0, \tag{7.20}$$

$$\theta'' + Pr(f\theta' + N_b\theta'\phi' + N_t\theta'^2) = 0, \tag{7.21}$$

$$\phi'' + Scf\phi' + \frac{N_t}{N_b}\theta'' = 0. \tag{7.22}$$

Along with the transformed boundary conditions

$$f(0) = 0, f'(0) = 1, f'(\infty) = \frac{a}{c}, g(0) = 0, g'(0) = 0, g''(\infty) = \gamma_1,$$

$$\theta'(0) = -Bi\left(1 - \theta(0)\right), \theta(\infty) = 0, \phi(0) = 1, \phi(\infty) = 0. \tag{7.23}$$

Since $f(y) = \frac{a}{c}y + A$ at $y \to \infty$, here A signifies the boundary layer displacement constant and $Bi = \frac{h_f}{k}\sqrt{\frac{\nu}{c}}$, is the Biot number. Substituting Eq (7.23) in above, we get $C_1 = M^2(\frac{a}{c}) + (\frac{a}{c})^2$ and $C_2 = -A\gamma_1$.

Introducing

$$g'(y) = \gamma_1 h(y). \tag{7.24}$$

Equations (7.19) − (7.22) along with the boundary conditions (7.23) take the form

$$f''' + ff'' - f'^2 + K_w\left(ff^{iv} + f''^2 - 2f'f'''\right) + M^2(\left(\frac{a}{c}\right) - f') + (\frac{a}{c})^2 = 0, \tag{7.25}$$

$$h'' - f'h + fh' + K_w(fh''' + f''h' - f'h'' - f'''h) - M^2 h - A = 0, \tag{7.26}$$

$$\theta'' + Pr(f\theta' + N_b\theta'\phi' + N_t\theta'^2) = 0, \tag{7.27}$$

$$\phi'' + Scf\phi' + \frac{N_t}{N_b}\theta'' = 0, \tag{7.28}$$

$$f(0) = 0, f'(0) = 1, f'(\infty) = \frac{a}{c}, h(0) = 0, h'(\infty) = 1,$$

$$\theta'(0) = -Bi\big(1-\theta(0)\big), \theta(\infty) = 0, \phi(0) = 1, \phi(\infty) = 0, \tag{7.29}$$

Local Shear stress and heat, mass flux at the stretching convective surface in non-dimensional form are given by

$$\tau_w = x(1-3K_w)f''(0) + (1-2K_w)\gamma_1 h'(0),$$

$$q_w = -\theta'(0),\ q_m = -\phi'(0). \tag{7.30}$$

The point of stagnation x_s can be attained by zero wall shear stress, i.e.

$$x_s = \frac{-(1-2K_w)\gamma_1 h'(0),}{(1-3K_w)f''(0)} \tag{7.31}$$

Where γ_1 control the obliqueness of the flow.

7.3 Numerical Solution

Equations $(7.25) - (7.28)$ with the boundary conditions (7.29) constitute a system of nonlinear, non-homogeneous differential equations for which closed form solution cannot be found. Hence, these equations are tackled through Spectral Quasilinearization Method (QLM) and the Spectral Local Linearization Method (LLM). The Quasilinearization technique (QLM) is essentially a generalized Newton-Raphson Method that was originally used by Bellman and Kalaba [62] for solving functional equations. Considering that the momentum equation (7.25) is decoupled from the rest of the equations in the system, this equation is solved for $f(y)$ first using the QLM. When the approximate solution for $f(y)$ is substituted in equation (7.26), the equation becomes linear and is solved directly by the Chebyshev spectral collocation scheme. Applying the QLM on $(7.25) - (7.28)$ we obtain the following iterative sequence of linear equations;

$$a_{1,r}f^{iv}_{r+1} + a_{2,r}f'''_{r+1} + a_{3,r}f''_{r+1} + a_{4,r}f'_{r+1} + a_{5,r}f_{r+1} = R_{1,r,} \tag{7.32}$$

$$b_{1,r}h'''_{r+1} + b_{2,r}h''_{r+1} + b_{3,r}h'_{r+1} + b_{4,r}h_{r+1} = R_{2,r,} \tag{7.33}$$

$$\theta''_{r+1} + c_{1,r}\theta'_{r+1} + c_{2,r}\phi'_{r+1} = R_{3,r,} \tag{7.34}$$

$$\phi''_{r+1} + c_{3,r}\phi'_{r+1} + \frac{N_t}{N_b}\theta'' = 0, \tag{7.35}$$

Subject to

$$f_{r+1}(0) = 0, f'_{r+1}(0) = 1, h_{r+1}(0) = 0, \theta'_{r+1}(0) = -Bi\big(1 - \theta_{r+1}(0)\big), \tag{7.36}$$

$$f'_{r+1}(\infty) = a/c, h'_{r+1}(\infty) = 1, \theta_{r+1}(\infty) = 0, \phi_{r+1}(0) = 1, \phi_{r+1}(\infty) = 0, \tag{7.37}$$

Where

$a_{1,r} = K_w f_r, a_{2,r} = 1 - 2K_w f'_r, a_{3,r} = f_r + 2K_w f''_r, a_{4,r} = -2f'_r - 2K_w f'''_r - M^2, a_{5,r} = f''_r + K_w f_r^{iv}, R_{1,r} = f_r f''_r - (f'_r)^2 + K_w\big(f_r f_r^{iv} - 2f'_r f'''_r + (f''_r)^2\big) - M^2\left(\frac{a}{c}\right) - \left(\frac{a}{c}\right), b_{1,r} = K_w f_{r+1}, b_{2,r} = 1 - K_w f'_{r+1}, b_{3,r} = f'_{r+1} + K_w f''_{r+1}, b_{4,r} = -f'_{r+1} - K_w f'''_{r+1} - M^2, R_{2,r} = A, c_{1,r} = Pr f_{r+1} + PrNb f'_r + 2PrNt\theta'_r, c_{2,r} = PrNb\theta'_r, c_{3,r} = Scf_{r+1}, R_{3,r} = Pr(Nb\theta'_r f'_r + Nt(\theta'_r)^2)$

Equations (7.25) and (7.26) can be solved independently for $f(y)$ and $h(y)$. However, (7.27) and (7.28) constitute a linear system of coupled differential equations with variable coefficients and must be solved simultaneously. The entirely system can be solved iteratively using any numerical method for $r = 1, 2, 3 \ldots$ In this work, the Chebyshev spectral collocation method approach will be utilized as describe in [63]. Starting from a given set of initial approximations $f_0, h_0, \theta_0, \phi_0$, the iteration schemes $(7.32) - (7.35)$ can be solved iteratively for $f_{r+1}(y), h_{r+1}(y), \theta_{r+1}(y)$ and $\phi_{r+1}(y)$ when $r = 1, 2, 3 \ldots$ before applying the spectral

collocation method, the domain in y is transformed to the interval $[-1, 1]$ so that spectral method can be applied. For the convenience of the numerical computations, the semi-infinite domain in y is approximated by the truncated domain $[0, L]$, where L is a finite number selected to be large enough to represent the behaviour of the flow properties when y is very large. We use the transformation $y = L\,(\eta + 1)/2$ to map the interval $[0, L]$ to $[-1, 1]$. The basic idea behind the spectral collocation method is the introduction of a differentiation matrix D which is used to approximate unknown derivatives of variables $f(y)$ at the grid points as the matrix vector product

$$\left.\frac{df(1)}{dy}\right|_{y_j} = \sum_{k=0}^{n} D_{jk}\, f(\eta k) = \mathbf{D}F, \;\; j = 0,1, \dots, N \qquad (7.38)$$

Where $N + 1$ is the number of collocation points, $\mathbf{D} = \frac{2D}{L}$

$$F = [F(\eta_0), F(\eta_1), \dots, F(\eta_N)]^T$$

Is the vector function at the collocation points. Similar vector functions corresponding to h, θ and ϕ are denoted by H, θ and Φ, respectively. Higher order derivatives are obtained as powers of *D*, that is

$$f^{(p)} = D^{(p)}F, h^{(p)} = D^{(p)}H, \theta^{(p)} = D^{(p)}\theta, \phi^{(p)} = D^{(p)}\Phi, \quad (7.39)$$

Where p is the order of the derivative. The matrix D have the size $(N + 1) \times (N + 1)$. The grid points on y are defined as

$$\eta_j = \frac{cos\pi_j}{N}, \quad j = 0,1,2, \dots, N \qquad (7.40)$$

Where $N+1$, represents total grid points in $y-$ direction. Thus, applying the spectral method on equations $(7.32) - (7.35)$ give

$$A_1 F_{r+1} = R_{1,r}, \tag{7.41}$$

$$A_2 H_{r+1} = R_{2,r}, \tag{7.42}$$

$$\begin{bmatrix} A_{11} & A_{12} \\ A_{21} & A_{22} \end{bmatrix} \begin{bmatrix} \theta \\ \Phi \end{bmatrix} = \begin{bmatrix} R_{3,r} \\ R_{4,r} \end{bmatrix} \tag{7.43}$$

Where A_i and $A_{ij}, (i,j = 1,2)$ are $(N+1) \times (N+1)$ matrices defined as:

$$A_1 = a_{1,r} D^4 + a_{2,r} D^3 + a_{3,r} D^2 + a_{4,r} D + a_{5,r}, \tag{7.44}$$

$$A_2 = b_{1,r} D^3 + b_{2,r} D^2 + b_{3,r} D + b_{4,r}, \tag{7.45}$$

$$A_{11} = D^2 + c_{1,r} D, A_{12} = c_{2,r} D, \tag{7.46}$$

$$A_{21} = \frac{Nt}{Nb} D^2, A_{22} = D^2 + c_{3,r} D, \tag{7.47}$$

and $R_{i,r}$ $(1,2,3,4)$ are $(N+1) \times 1$ vectors obtained by evaluating the right hand sides of $(7.32) - (7.35)$ at the collocation points.

7.4 Graphical Results and Analysis

To find out the impact of certain emerging flow parameters on the normal and tangential velocities, temperature and concentration, Figs $(7.2) - (7.18)$ are plotted. The influence of applied magnetic field through parameter M on normal component of flow $f(y)$ and velocity profiles $f'(y)$ is shown through Figs (7.2) and (7.3). It is quite obvious from these two figures that when $M = 0$, flow and velocity profiles are higher near the wall and it continuously drops

down with increasing magnetic field M. These is because of upward direction of applied force which opposes the normal flow and velocity profiles, consequently leads to a significant drop in normal component of flow and velocity profiles. From Figs (7.4) and (7.5) we can perceive that tangential component of the flow $h(y)$ as well as magnitude of the tangential velocity profile $h'(y)$ declines with Magnetic field M. With this, we can come up to the conclusion that application of Magnetic field causes the normal as well as tangential flow and velocity profiles to decrease near the convective surface. The effect of applied magnetic field M on temperature $\theta(y)$ and concentration profiles $\Phi(y)$ is depicted through Figs (7.6) and (7.7). We can see that the influence of magnetic field on the temperature profile $\theta(y)$ is positive. It significantly rises with increasing magnetic field. While on the other hand, the behaviour of the concentration profile $\Phi(y)$ against M can be seen from Fig (7.7). It is observed that concentration profile $\Phi(y)$ increases with M. Figs (7.8) and (7.9) are plotted to discover the influence of thermophoresis parameter Nt on the temperature $\theta(y)$ and concentration profile $\Phi(y)$ respectively. It can be noticed here that with increasing Nt, temperature profile $\theta(y)$ rises within the boundary layer region (see Fig (7.8)). Impact of thermophoresis Nt on the concentration profile $\Phi(y)$ is different from as it was on temperature. We can see that it slightly drops down very close to the wall, and then depicts an increasing behaviour with increasing Nt. Similarly the effects of Brownian motion Nb, on the temperature $\theta(y)$ and concentration profile $\Phi(y)$ is revealed through Figs (7.10) and (7.11). It is quite evident from these graphs that Brownian motion has opposite influence on temperature $\theta(y)$ and concentration profile $\Phi(y)$, i.e. it causes the temperature to rise down while leads to a significant drop in the concentration profile. This is perhaps due to the reason that the random motion of the particles results in continuous collisions of the fluid particles which consequently heats up the fluid and drops the concentration profile.

Figs (7.12) and (7.13) are constructed to examine temperature $\theta(y)$ and concentration profile $\Phi(y)$ versus Prandtl number Pr respectively. We can see that temperature decreases with Prandtl number Pr (see Fig (7.12)). On the other hand, concentration profile $\Phi(y)$ gives an increasing behaviour with Pr within the boundary layer region (See Fig (7.13)). We can notice from Fig (7.14) that temperature profile $\theta(y)$ rises with an increase in Schmidt number Sc. But when we look at the graph of concentration profile $\Phi(y)$ through Fig (7.15), it is quite apparent that concentration profile $\Phi(y)$ significantly drops down with Sc. Finally, effects of Biot number Bi, on the temperature and concentration profiles are presented through Figs (7.16) and (7.17). One can certainly realise that influence of Biot number Bi on these two quantities is positive, i.e. it causes an increase in temperature $\theta(y)$ and concentration profile $\Phi(y)$ near the stretching surface. Finally, Fig (7.18) is plotted to discover the stream line patterns when $M = 0$ and $M = 0.5$. It can be seen that application of magnetic field causes a disturbance in the obliqueness of the flow. $Table$ 7.1 gives the numerical values of $f''(0)$ obtained by Pop et al [14] and are compared with our numerical results when $K_w = 0$ and they are in very good agreement. $Table$ 7.2 gives the variations in boundary layer displacement constant A with M and K_w. Similarly $Table$ 7.3 and 7.4 are prepared to compute the normal $f''(0)$ and tangential $h'(0)$ components of local shear stress respectively. It is observed from $Table$ 7.3 that with an increase in magnetic parameter M, $f''(0)$ also increases. It is found from $Table$ 7.4 that magnetic field parameter causes to reduce the tangential skin friction component $h'(0)$. This is perhaps because of the upward direction of the constantly applied magnetic field which favours the shear flow and ultimately reduces the tangential skin friction $h'(0)$. $Table$ 7.5 shows that with an increase in the magnetic field through parameter M, local heat flux $-\theta'(0)$ at the wall decreases. It can also be noticed from this table that increasing the viscoelasticity through

parameter K_w, causes a reduction in local heat flux $-\theta'(0)$ at the wall. The influence of thermophoresis parameter Nt, Prandtl number Pr, Brownian motion Nb and Schmidt number Sc on the local heat flux $-\theta'(0)$ is presented through $Tables$ 7.6 and 7.7. It is noticed from $Table$ 7.6 that local heat flux drops with Brownian motion Nb as well as thermophoresis parameter Nt. Similar kind of behaviour is observed for the local heat flux with increasing Prandtl number Pr as well as Schmidt number Sc see e.g. ($Table$ 7.7). The main reason behind it is that a larger Prandtl number fluid means lower thermal conductivity which consequently decreases heat transfer rate at the surface. Influence of viscoelasticity through parameter K_w, magnetic field parameter M, thermophoresis parameter Nt, Prandtl number Pr, Brownian motion Nb and Schmidt number Sc on the local mass flux $-\phi'(0)$ are presented through $Tables$ $7.8 - 7.10$. We can easily see from $Table$ 7.8 that when $K_w = 0.1$ and increasing the magnetic field parameter M, the local mass flux $-\phi'(0)$ decreases. But for all other larger values of K_w, magnetic field M causes the local mass flux$-\phi'(0)$ to rise at the stretching convective surface. Similarly from $Table$ 7.9 it can be perceived that for fixed values of Brownian motion parameter Nb, local mass flux rate $-\phi'(0)$ decreases with thermophoresis parameter Nt. Finally, it is found from $Table$ 7.10 that local mass flux $-\phi'(0)$ also increases with Sc, when Prandtl number Pr is fixed.

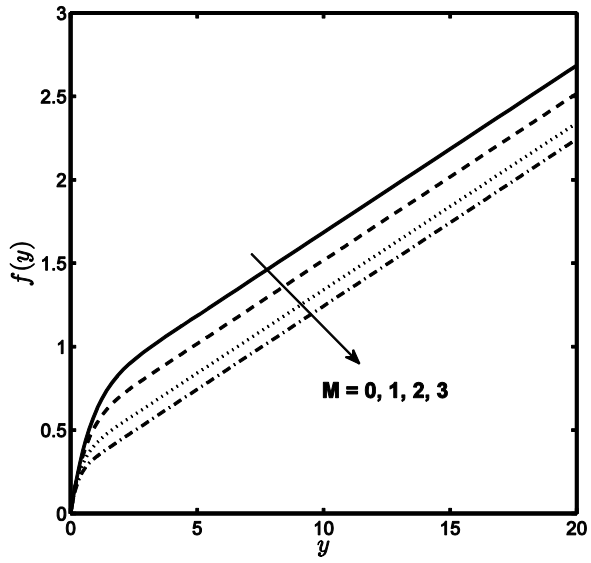

Fig (7.2): Flow profile $f(y)$ against M when $\frac{a}{c} = 0.1, K_w = 0.2$.

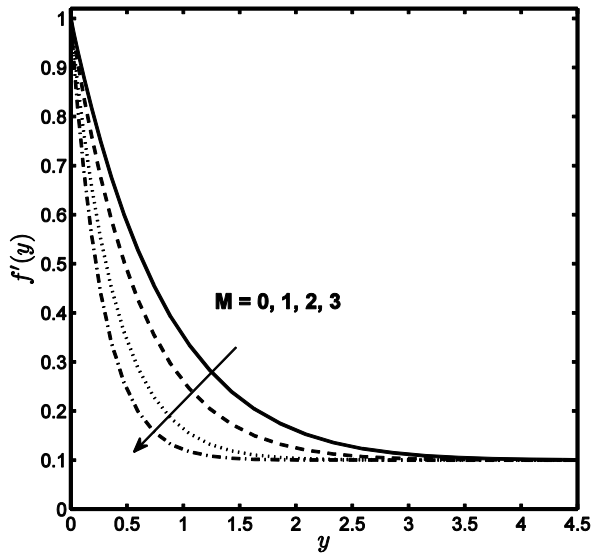

Fig (7.3): Velocity profile $f'(y)$ against M when $\frac{a}{c} = 0.1, K_w = 0.2$.

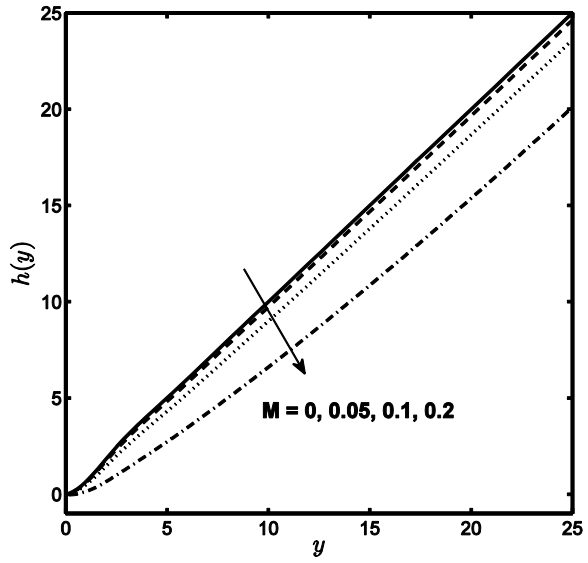

Fig (7.4): Flow profile $h(y)$ against M when

$$\frac{a}{c} = 0.2, K_w = 0.5.$$

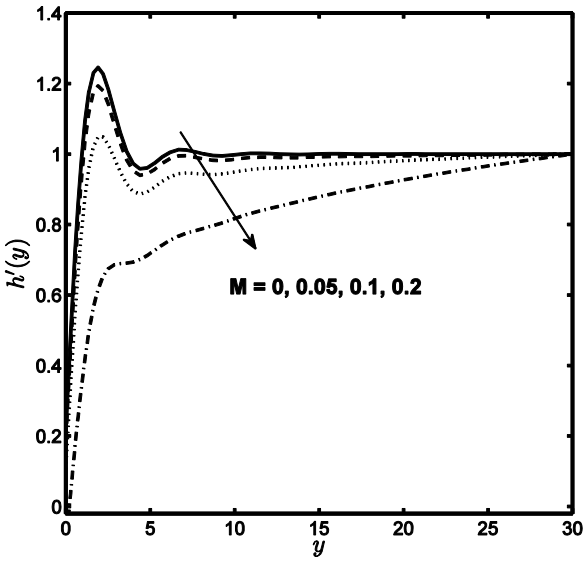

Fig (7.5): Velocity profile $h'(y)$ against M when $\frac{a}{c} = 0.2, K_w = 0.5$.

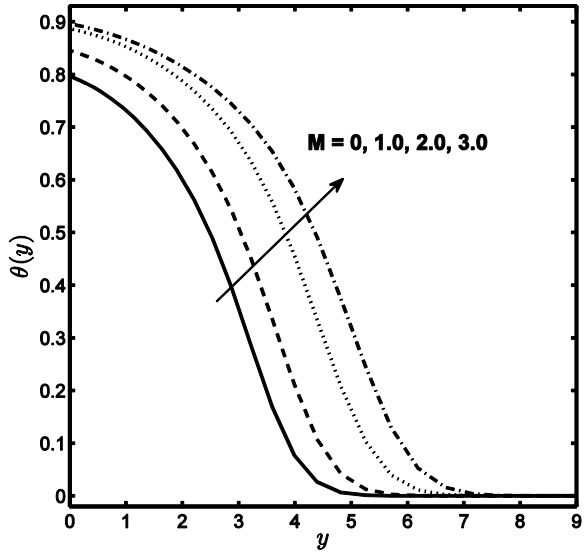

Fig (7.6): Temperature profile $\theta(y)$ against M when

$\frac{a}{c} = 0.1, K_w = 0.2, Pr = 7, Sc = 3, Nb = Nt = 0.1, Bi = 0.2.$

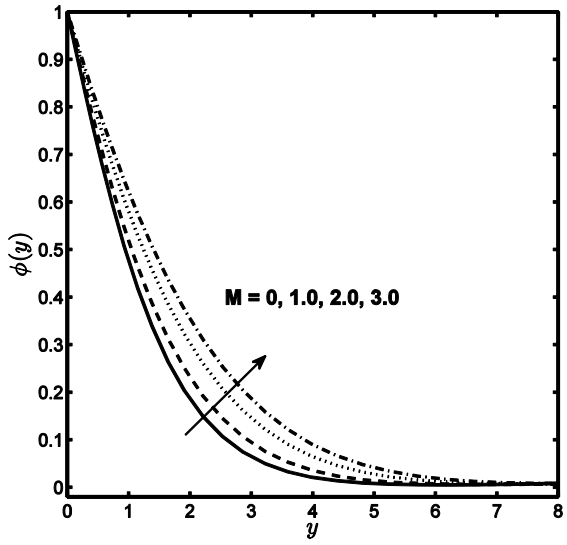

Fig (7.7): Concentration profile $\Phi(y)$ against M when

$\frac{a}{c} = 0.1, K_w = 0.1, Pr = Sc = 1, Nb = Nt = 0.1, Bi = 1.$

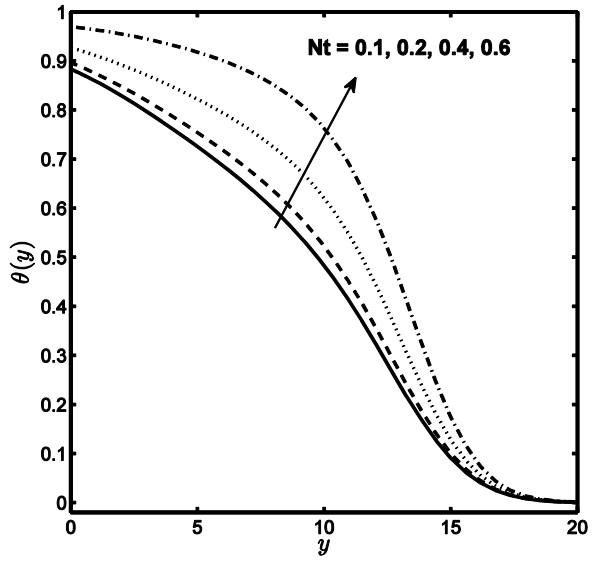

Fig (7.8): Temperature profile $\theta(y)$ against Nt when

$\frac{a}{c} = 0.1, K_w = 0.1, Pr = Sc = 1, M = 0.5, Nb = 0.3, Bi = 0.2.$

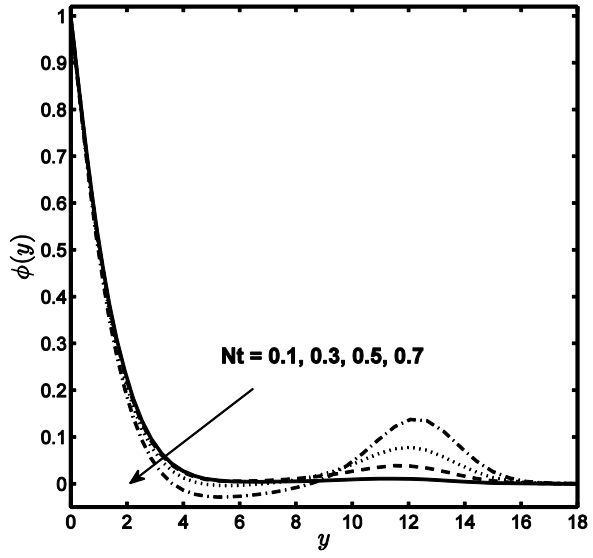

Fig (7.9): Concentration profile $\Phi(y)$ against Nt when

$\frac{a}{c} = 0.2, K_w = 0.5, Pr = \ Sc = 1, M = 0.5, Nb = 0.3, Bi = 0.3.$

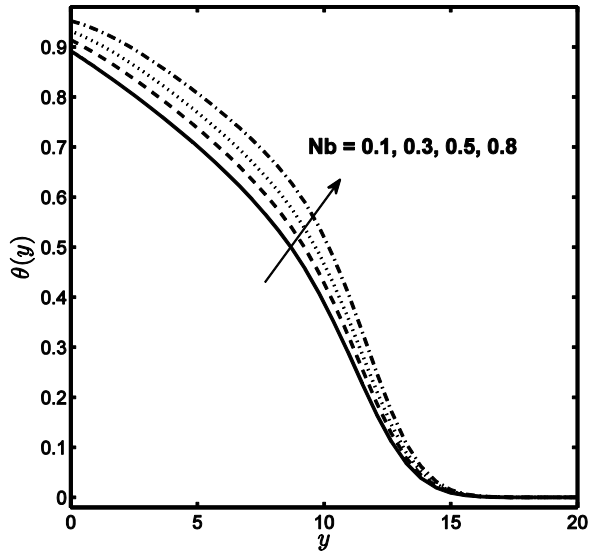

Fig (7.10): Temperature profile $\theta(y)$ against Nb when

$\frac{a}{c} = 0.2, K_w = M = 0.5, Pr = \ Sc = 1, Nt = Bi = 0.3.$

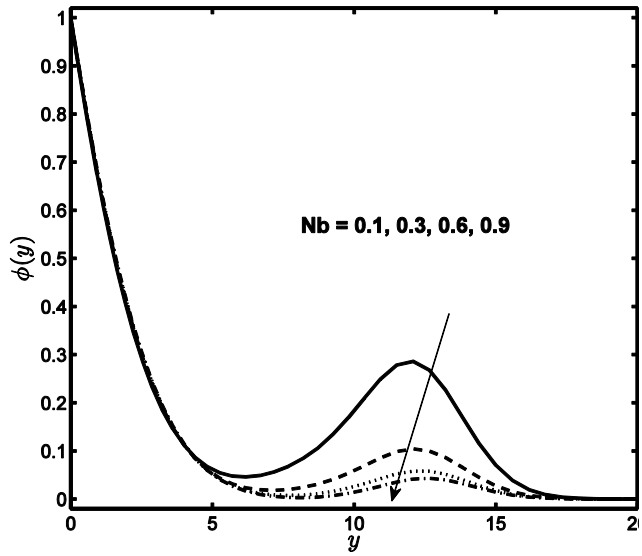

Fig (7.11): Concentration profile $\Phi(y)$ against Nb when

$\frac{a}{c} = 0.2, K_w = M = 0.5, Pr = 1, Sc = 0.5, Nt = 0.4, Bi = 0.3.$

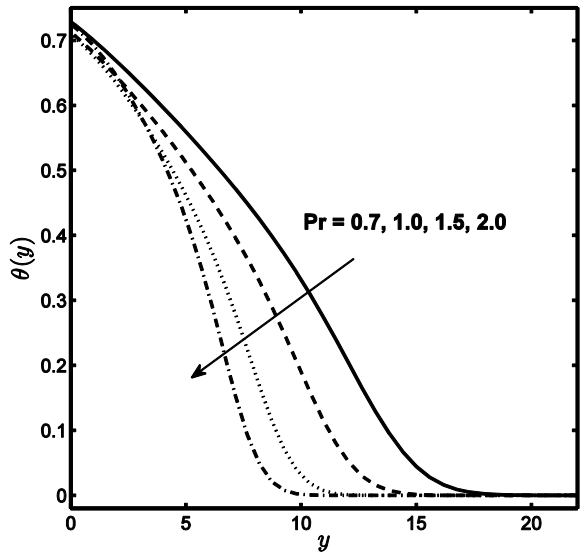

Fig (7.12): Temperature profile $\theta(y)$ against Pr when

$\frac{a}{c} = 0.2, K_w = Bi = 0.1, M = 0.5, Sc = 1, Nt = Nb = 0.3.$

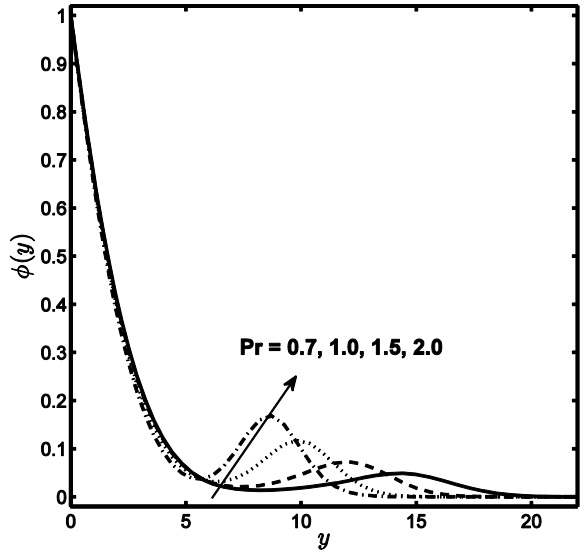

Fig (7.13): Concentration profile $\Phi(y)$ against Pr when

$\frac{a}{c} = 0.2, K_w = M = Sc = 0.5, Nt = Nb = Bi = 0.3.$

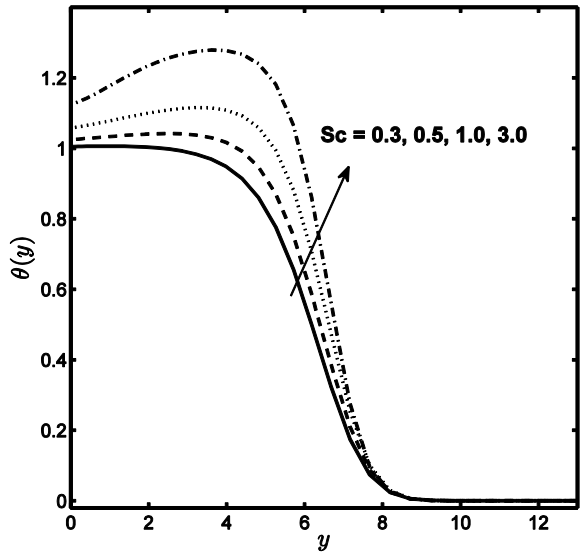

Fig (7.14): Temperature profile $\theta(y)$ against Sc when

$\frac{a}{c} = 0.2, K_w = M = 0.5, pr = 3.0, Nt = Nb = Bi = 0.3.$

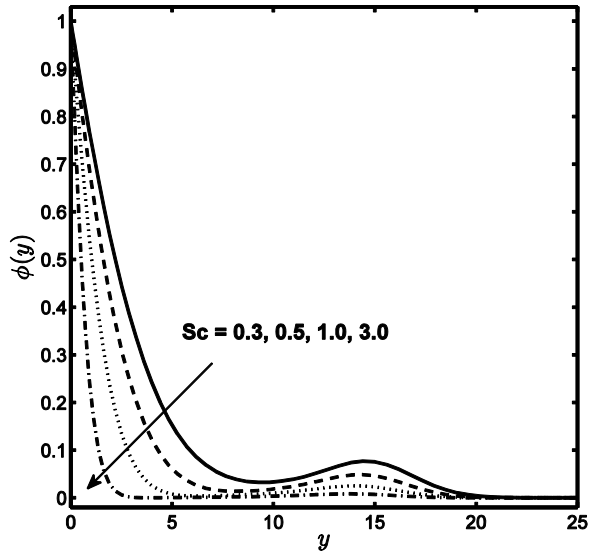

Fig (7.15): Concentration profile $\Phi(y)$ against Sc when

$\frac{a}{c} = 0.2, K_w = M = 0.5, pr = 0.7, Nt = Nb = Bi = 0.3.$

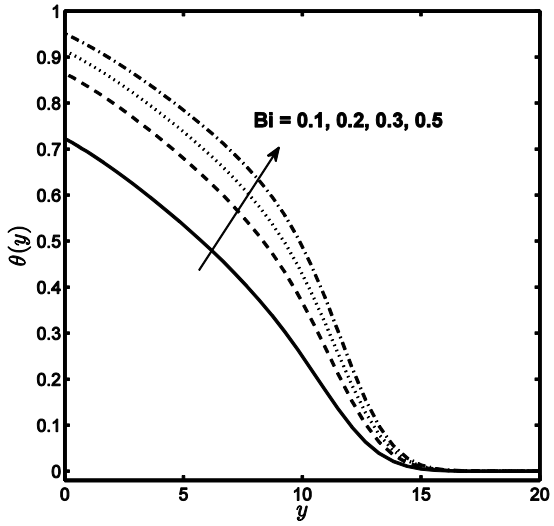

Fig (7.16): Temperature profile $\theta(y)$ against Bi against Sc when

$\frac{a}{c} = 0.2, K_w = M = 0.5, pr = Sc = 1.0, Nt = Nb = 0.3.$

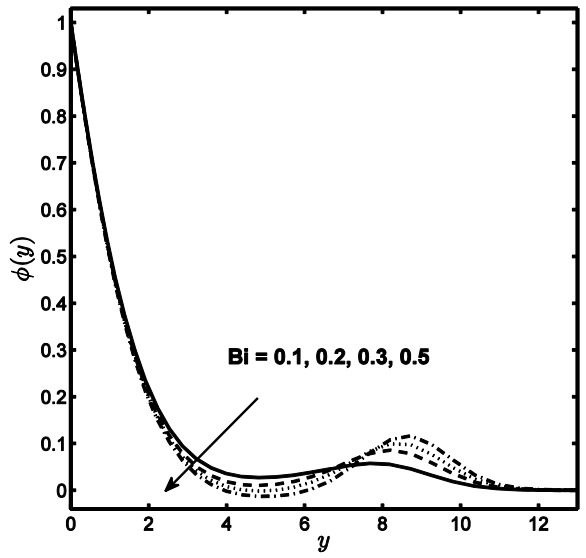

Fig (7.17): Concentration profile $\Phi(y)$ against Bi when

$\frac{a}{c} = 0.2, K_w = M = 0.5, pr = 2.0, Sc = 1.0, Nt = Nb = 0.3.$

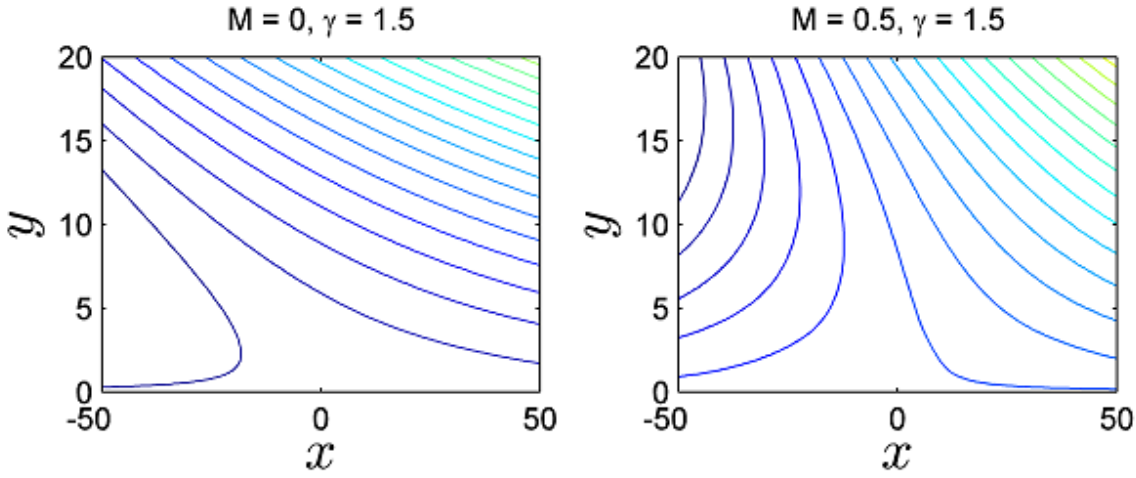

Fig (7.18): Stream line patterns for oblique flow when

$$\frac{a}{c} = 0.3, K_w = 0.2, \gamma_1 = +1.5.$$

	$f''(0)$		$h'(0)$		$-\theta'(0)$	
a/c	Present	Pop et al [14]	Present	Pop et al [14]	Present	Pop et al [14]
0.1	−0.96938	−0.96938	0.26278	0.26278	0.60281	0.60281
0.3	−0.84942	−0.84942	0.60573	0.60573	0.64732	0.64732
0.8	−0.29938	−0.29938	0.93430	0.93430	0.75709	0.75709
1.0	0.0	0.0	1.0	1.0	0.79788	0.79788
2.0	2.01750	2.01750	1.16489	1.16489	0.97872	0.97872
3.0	4.72928	4.72928	1.23438	1.23438	1.13209	1.13209

Table 7.1: Comparison with the existing literature when $K_w = 0$, $Bi \to \infty$.

M\K$_w$	0	0.1	0.2	0.4	0.6	0.8
0	0.32860	0.28959	0.24594	0.14574	0.13698	0.13376
0.1	0.32791	0.28899	0.24543	-0.76143	0.13808	0.13111
0.2	0.32587	0.2872	0.2439	0.21167	0.14156	0.12417
0.4	0.31809	0.28033	0.23806	0.17889	0.15757	0.10837
0.6	0.30622	0.26988	0.22917	0.26588	0.19058	0.10908
0.8	0.29158	0.25698	0.2182	0.12677	0.24908	0.13853

Table 7.2: Numerical values of boundary layer displacement constant A when $\frac{a}{c} = 0.5$.

M\K$_w$	0	0.1	0.2	0.4	0.6	0.8

0.0	-0.66726	-0.73000	-0.81021	-0.45861	-0.56181	-1.00182
0.1	-0.66910	-0.73203	-0.81251	-4.05864	-0.55023	-0.99097
0.2	-0.67459	-0.73810	-0.81937	0.69801	-0.51556	-0.95877
0.4	-0.69614	-0.76193	-0.84628	0.08536	-0.37786	-0.83487
0.6	-0.73071	-0.80014	-0.88942	0.86451	-0.15032	-0.64388
0.8	-0.77665	-0.85088	-0.94664	-1.18104	0.16756	-0.39986

Table 7.3: Numerical values of Normal skin friction co-efficient $f''(0)$ when $\frac{a}{c} = 0.5$.

M\K$_w$	0	0.1	0.2	0.4	0.6	0.8
0.0	0.78268	0.74961	0.70756	0.60383	0.38110	0.06251
0.1	0.69085	0.66268	0.62736	0.54442	0.33658	0.05022
0.2	0.45858	0.44312	0.42509	0.35539	0.22104	0.01829
0.4	-0.05075	-0.03617	-0.01496	-0.03014	-0.06444	-0.06160
0.6	-0.27686	-0.24785	-0.20933	-0.37416	-0.28032	-0.13211
0.8	-0.28924	-0.26069	-0.22359	-0.12284	-0.49315	-0.23385

Table 7.4: Numerical values of tangential skin friction co-efficient $h'(0)$ when $\frac{a}{c} = 0.5$.

M\K$_w$	0	0.1	0.3	0.5	1	3
0	0.06425	0.06366	0.06308	0.06333	-0.00022	0.00000
0.1	0.06425	0.06365	0.06309	0.06330	0.05536	-40.33956

0.3	0.06421	0.06364	0.06312	0.06310	0.23411	0.00000
0.5	0.06415	0.06360	0.06320	0.06280	0.00003	0.04601
0.8	0.06401	0.06353	0.06345	0.06235	0.05010	0.05752
1	0.06391	0.06348	0.06380	0.06223	0.05415	0.06502
3	0.06329	0.06315	0.06294	0.06297	0.06073	0.05839

Table 7.5: Numerical values of local heat flux $-\theta'(0)$ when $Bi = 0.5, Pr = Sc = 1.0, Nt = Nb = 0.3, \frac{a}{c} = 0.5$.

Nt\Nb	0.1	0.2	0.3	0.5	0.8	1
0.1	0.05710	0.05183	0.04690	0.03810	0.02753	0.02210
0.2	0.05389	0.04866	0.04380	0.03518	0.02499	0.01985
0.3	0.05059	0.04541	0.04061	0.03218	0.02238	0.01752
0.5	0.04361	0.03853	0.03386	0.02582	0.01678	0.01249
0.8	0.03179	0.02678	0.02225	0.01461	0.00644	0.00285
1.0	0.02235	0.01723	0.01260	0.00484	0.00340	0.00696

Table 7.6: Numerical values of local heat flux $-\theta'(0)$ when $Bi = 0.3, Pr = Sc = 1.0, M = K_w = 0.5, \frac{a}{c} = 0.2$.

Pr\Sc	0.1	0.3	0.5	0.8	1	3
0.1	0.02546	0.02541	0.02539	0.02538	0.02538	0.02536

0.3	0.03143	0.03113	0.03108	0.03105	0.03104	0.03101
0.8	0.04449	0.04175	0.04113	0.04083	0.04073	0.04051
1.0	0.04779	0.04364	0.04260	0.04207	0.04191	0.04156
10.0	0.09057	0.02769	0.04147	0.16607	0.28697	0.09585
100.0	0.42154	0.41740	0.39706	0.47281	3.22413	0.45802

Table 7.7: Numerical values of local heat flux $-\theta'(0)$ when $Bi = 0.3, Nt = Nb = 0.3, M = K_w = 0.5, \frac{a}{c} = 0.2$.

M\K$_w$	0	0.1	0.3	0.5	1	3
0	0.70720	0.69057	0.67582	0.71129	0.00026	0.00000
0.1	0.70704	0.69040	0.67657	0.71201	-0.02404	40.66124
0.3	0.70580	0.68911	0.68270	0.71785	-0.59007	0.00000
0.5	0.70343	0.68668	0.69581	0.72967	0.00001	0.73883
0.8	0.69827	0.68142	0.73369	0.75964	0.73477	0.76210
1	0.69412	0.67725	0.77690	0.78948	0.75472	0.77729
3	0.65383	0.63942	0.60378	0.66594	0.71312	0.71049

Table 7.8: Numerical values of local mass flux $-\phi'(0)$ when $Bi = 0.3, Pr = Sc = 1.0, Nt = Nb = 0.3, \frac{a}{c} = 0.5$.

Nt\Nb	0.1	0.2	0.3	0.5	0.8	1.0

0.1	0.53927	0.54250	0.54344	0.54397	0.54392	0.54375
0.2	0.54152	0.54572	0.54684	0.54726	0.54681	0.54634
0.3	0.54804	0.55092	0.55146	0.55114	0.54989	0.54901
0.5	0.57416	0.56738	0.56435	0.56059	0.55664	0.55456
0.8	0.64866	0.60846	0.59369	0.57955	0.56850	0.56357
1.0	0.72735	0.64978	0.62210	0.59691	0.57869	0.57096

Table 7.9: Numerical values of local mass flux $-\phi'(0)$ when $Bi = 0.3, M = K_w = 0.5, Pr = Sc = 1.0, \frac{a}{c} = 0.2$.

Pr\Sc	0.1	0.3	0.5	0.8	1	3
0.1	0.13529	0.25655	0.35086	0.47088	0.54216	1.08021
0.3	0.12994	0.25480	0.35007	0.47071	0.54221	1.08094
0.8	0.12532	0.25595	0.35286	0.47455	0.54642	1.08610
1.0	0.12377	0.25692	0.35460	0.47672	0.54873	1.08872
10.0	0.08717	0.31645	0.51361	0.78764	0.98737	0.97899
100.0	0.39419	0.31990	0.19249	0.49566	10.20110	0.16633

Table 7.10: Numerical values of local mass flux $-\phi'(0)$ when $Bi = 0.3, M = K_w = 0.5, Nt = Nb = 0.3, \frac{a}{c} = 0.2$.

7.5 Conclusion

We have discussed the oblique MHD Walter-B nanofluid flow over a convective surface. The governing differential equations of the problem are presented by means of suitable similarities and then solved by Spectral Quasilinearization method (QLM) along with Spectral Local linearization method (LLM). The graphical results for normal and tangential velocities, temperature and concentration have been presented against several emerging non-dimensional parameters. Numerical values of local surface shear stresses and heat as well as mass flux at the wall are offered in tabulated form and discussed. Following conclusions are drawn from this study:

- Magnetic field parameter M decreases the normal and tangential velocity profiles where as it increases the fluid temperature.
- Thermophoresis and Brownian motion has opposite influence on temperature and concentration profiles.
- Magnetic field parameter M and local Weissenberg number K_w decreases the local heat and mass flux at the convective surface.
- Prandtl number Pr and Schmidt number Sc have opposite influence on local heat and mass flux.

Chapter 8

Effect of internal heat generation/absorption on an obliquely striking Maxwell fluid past a convective surface

8.1 Introduction

This chapter numerically examines internal heat generation/absorption effects on oblique flow of a Maxwell fluid with convective boundary condition. By transforming the governing equations via suitable similarity transformations, Spectral Quasilinearization Method (QLM) along with Spectral Local Linearization Method (LLM) is applied to solve the system of equations. The velocity, temperature and local heat flux rate at the stretching convective surface are presented through graphs against pertinent flow parameters and analysed. It is found that elasticity parameter δ has opposite influence on normal and tangential components of velocity while it increases the temperature profile. Moreover temperature profile rises with heat generation (i.e. $\lambda > 0$). Local heat flux at the convective surface decreases with heat generation and it increases with an increase in heat absorption parameter.

8.2 Problem Formulation

Consider steady, incompressible, two-dimensional, obliquely striking Maxwell fluid past a stretching surface. It is presumed that the flow is being restrained in the region $y > 0$, where y is the coordinate measured normal to the stretching surface. We further assume that the stretching velocity is cx and the velocity far away is $ax + by$ due to oblique flow and $a, b, c > 0$ are

constants of inverse time dimension. Fig (8.1) describes the non-dimensional model and the coordinate system. The Cauchy stress tensor for Maxwell fluid is given by

$$\boldsymbol{\tau_{ij}} + \lambda_m \frac{\delta}{\delta t}\boldsymbol{\tau_{ij}} = 2\mu \boldsymbol{d_{ij}}$$

Where μ is the zero shear rate viscosity, λ_m the relaxation time of Maxwell fluid, $\boldsymbol{d_{ij}} = \frac{1}{2}(\frac{\partial u_i}{\partial x_j} + \frac{\partial u_j}{\partial x_i})$ is the deformation rate tensor and $\frac{\delta}{\delta t}$ is upper convective derivative of a tensor and can be obtained by $\frac{\delta}{\delta t}\boldsymbol{\tau_{ij}} = \frac{D}{Dt}\boldsymbol{\tau_{ij}} - \boldsymbol{L_{jk}\tau_{ik}} - \boldsymbol{\tau_{kj}L_{ik}}$, in which $\boldsymbol{L_{ij}}$ is the velocity gradient.

The basic steady conservation of mass, momentum and thermal energy can be written as [18, 19].

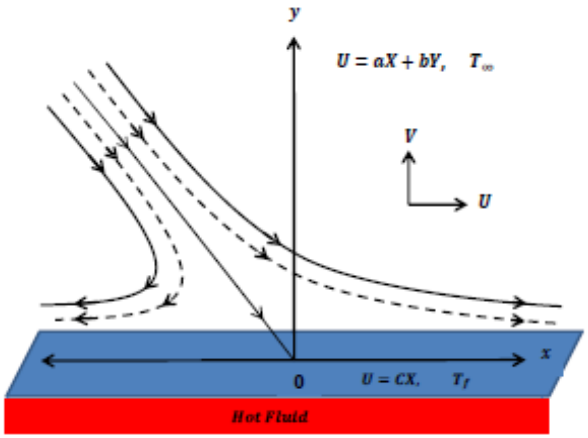

Fig (8.1): Non-dimensional description of the problem

$$\frac{\partial u^*}{\partial x^*} + \frac{\partial v^*}{\partial y^*} = 0 \qquad (8.1)$$

$$u^*\frac{\partial u^*}{\partial x^*} + v^*\frac{\partial u^*}{\partial y^*} + \lambda_m\left(u^{*2}\frac{\partial^2 u^*}{\partial x^{*2}} + v^{*2}\frac{\partial^2 u^*}{\partial y^{*2}} + 2u^*v^*\frac{\partial^2 u^*}{\partial x^*\partial y^*}\right) = -\frac{1}{\rho}\frac{\partial p^*}{\partial x^*} + \nu\nabla^{*2}u^* \qquad (8.2)$$

$$u^*\frac{\partial v^*}{\partial x^*} + v^*\frac{\partial v^*}{\partial y^*} + \lambda_m\left(u^{*2}\frac{\partial^2 v^*}{\partial x^{*2}} + v^{*2}\frac{\partial^2 v^*}{\partial y^{*2}} + 2u^*v^*\frac{\partial^2 v^*}{\partial x^*\partial y^*}\right) = -\frac{1}{\rho}\frac{\partial p^*}{\partial y^*} + \nu\nabla^{*2}v^* \qquad (8.3)$$

$$u^*\frac{\partial T^*}{\partial x^*} + v^*\frac{\partial T^*}{\partial y^*} = \alpha^*\nabla^{*2}T^* + \frac{Q_0}{\rho C_p}(T^* - T_\infty), \qquad (8.4)$$

Where u^*, v^* are velocities along coordinate axis, ν the effective kinematic viscosity, T^* temperature, α^* effective thermal diffusivity, Q_0 is the dimensional heat generation/absorption coefficient and C_p is specific heat. T_f the convective temperature of stretched surface, h_f is heat transfer coefficient and T_∞ is ambient fluid temperature. Keeping these assumptions in mind, the suitable conditions can be stated as [44].

$$u^* = cx^*, -k\frac{\partial T^*}{\partial y^*} = h_f\left(T_f - T^*\right) \ at\ y^* = 0$$

$$u^* = ax^* + by^*,\ T^* = T_\infty \ as\ y^* \to 0 \qquad (8.5)$$

In order to obtain the similarity solutions of Eqs (8.1) − (8.4) with boundary conditions (8.5), the dimension less variables can be chosen as [14]

$$x = x^*\sqrt{\frac{c}{\nu}}, y = y^*\sqrt{\frac{c}{\nu}}, u = \frac{1}{\sqrt{\nu c}}u^*,$$

$$v = \frac{1}{\sqrt{\nu c}}v^*, p = \frac{1}{\sqrt{\mu c}}p^*, T = \frac{T^* - T_\infty}{T_f - T_\infty}. \qquad (8.6)$$

Substituting, Eq (8.6) into Eqs (8.1) − (8.4) our governing system takes the following non-dimensional form

$$\frac{\partial u}{\partial x} + \frac{\partial v}{\partial y} = 0 \qquad (8.7)$$

$$u\frac{\partial u}{\partial x} + v\frac{\partial u}{\partial y} + \delta\left(u^2\frac{\partial^2 u}{\partial x^2} + v^2\frac{\partial^2 u}{\partial y^2} + 2uv\frac{\partial^2 u}{\partial x \partial y}\right) = -\frac{\partial p}{\partial x} + \nabla^2 u \qquad (8.8)$$

$$u\frac{\partial v}{\partial x} + v\frac{\partial v}{\partial y} + \delta\left(u^2\frac{\partial^2 v}{\partial x^2} + v^2\frac{\partial^2 v}{\partial y^2} + 2uv\frac{\partial^2 v}{\partial x \partial y}\right) = -\frac{\partial p}{\partial y} + \nabla^2 v \qquad (8.9)$$

$$u\frac{\partial T}{\partial x} + v\frac{\partial T}{\partial y} = \frac{1}{Pr}\nabla^2 T + \lambda T \qquad (8.10)$$

Where $\delta = \lambda_1 c$ is the non-dimensional relaxation time, $Pr = \frac{\mu C_p}{k}$ is the Prandtl number and $\lambda = \frac{Q_0}{\rho c C_p}$ is the heat source/sink parameter.

Introducing the stream function relations

$$u = \frac{\partial \psi}{\partial y}, v = -\frac{\partial \psi}{\partial x}. \qquad (8.11)$$

Using Eq (8.11) in Eqs (8.7) $-$ (8.10), by eliminating the pressure we get

$$\nabla^4\psi + \frac{\partial(\psi,\nabla^2\psi)}{\partial(x,y)} - \delta\frac{\partial}{\partial y}\left\{\frac{\partial^3\psi}{\partial x^2\partial y}\left(\frac{\partial\psi}{\partial y}\right)^2 + \left(\frac{\partial\psi}{\partial x}\right)^2\frac{\partial^3\psi}{\partial y^3} - 2\frac{\partial^3\psi}{\partial x\partial y^2}\frac{\partial\psi}{\partial x}\frac{\partial\psi}{\partial y}\right\} + \delta\frac{\partial}{\partial x}\left\{\frac{\partial^3\psi}{\partial x\partial y^2}\left(\frac{\partial\psi}{\partial x}\right)^2 -$$

$$\left(\frac{\partial\psi}{\partial y}\right)^2\frac{\partial^3\psi}{\partial x^3} + 2\frac{\partial^3\psi}{\partial x^2\partial y}\frac{\partial\psi}{\partial x}\frac{\partial\psi}{\partial y}\right\} = 0, \qquad (8.12)$$

$$\frac{\partial\psi}{\partial y}\frac{\partial T}{\partial x} - \frac{\partial\psi}{\partial x}\frac{\partial T}{\partial y} = \frac{1}{Pr}\nabla^2 T + \lambda T \qquad (8.13)$$

In order to transform Eqs (8.12) and (8.13) in to ordinary differential equations, following [14]

$$\psi(x,y) = xf(y) + g(y), T = \theta(y), \qquad (8.14)$$

Substituting Eq (8.14) in above, we achieve the following system of coupled non-linear differential equations

$$f''' - f'^2 + ff'' + \delta(2f'ff'' - f'''f^2) + C_1 = 0, \qquad (8.15)$$

$$g''' - f'g' + fg'' + \delta(2g'ff'' - f^2g''') + C_2 = 0, \qquad (8.16)$$

$$\theta'' + Pr(f\theta' + \lambda\theta) = 0, \qquad (8.17)$$

Along with the transformed boundary conditions

$$f(0) = 0, f'(0) = 1, f'(\infty) = \frac{a}{c}, g(0) = 0, g'(0) = 0,$$

$$g''(\infty) = \gamma_1, \theta'(0) = -Bi\big(1 - \theta(0)\big), \theta(\infty) = 0, \qquad (8.18)$$

where $Bi = \frac{h_f}{k}\sqrt{\frac{c}{\nu}}$ is the Biot number. Since $f(y = \left(\frac{a}{c}\right)y + A$ at $y \to \infty$, Where A signifies the boundary layer displacement constant. Substituting Eq (8.18) in above, we get $C_1 = (\frac{a}{c})^2$ and $C_2 = -A\gamma$.

Making use of the transformation

$$g'(y) = \gamma_1 h(y). \tag{8.19}$$

Equations (8.15) − (8.17) along with their boundary conditions (8.18), finally take the form as

$$f''' - f'^2 + ff'' + \delta(2f'ff'' - f'''f^2) + (\frac{a}{c})^2 = 0, \tag{8.20}$$

$$h'' - f'h + fh' + \delta(2ff''h - h''f^2) - A = 0, \tag{8.21}$$

$$\theta'' + Pr(f\theta' + \lambda\theta) = 0, \tag{8.22}$$

$$f(0) = 0, h(0) = 0, f'(0) = 1, f'(\infty) = \frac{a}{c},$$

$$h'(\infty) = 1, \theta'(0) = -Bi\big(1 - \theta(0)\big), \theta(\infty) = 0. \tag{8.23}$$

8.3 Non-dimensional quantity of interest

We are interested here in local heat flux, which can be determined by

$$q_w = -k\left(\frac{\partial T}{\partial y}\right)_{y=0} \tag{8.24}$$

In non-dimensional form, we can write

$$q_w = -\theta'(0) \tag{8.25}$$

8.4 Numerical Solution

The governing system of equations (8.20) − (8.23) are non-linear in nature so their solutions cannot be found exactly. We have employed a numerical scheme called Chebyshev spectral collocation to approximate the solution of equations(8.20) − (8.23). Before applying the spectral method, the equations are linearized using the quasi-linearization (QLM) approach that was initially proposed by Bellman and Kalaba [62] for solving functional equations. Considering that the momentum equation for determining f(y) is decoupled from the rest of the equations in the system, this equation is solved for $f(y)$ first using the QLM and spectral collocation method.

The approximate solution for $f(y)$ is then substituted in the other two equations which are solved, in turn, for $h(y)$ and $\theta(y)$. Applying the QLM on the system of equations give

$$a_{1,r}f'''_{r+1} + a_{2,r}f''_{r+1} + a_{3,r}f'_{r+1} + a_{4,r}f_{r+1} = R_{1,r,} \quad (8.26)$$

$$b_{1,r}h''_{r+1} + b_{2,r}h'_{r+1} + b_{3,r}h_{r+1} = R_{2,r,} \quad (8.27)$$

$$\theta''_{r+1} + c_{1,r}\theta'_{r+1} + Pr\lambda\theta_{r+1} = 0, \quad (8.28)$$

Subject to

$$f_{r+1}(0) = 0, h_{r+1}(0) = 0, \theta'_{r+1}(0) = -Bi\big(1 - \theta_{r+1}(0)\big),$$

$$f'_{r+1}(0) = 1, f'_{r+1}(\infty) = a/c, h'_{r+1}(\infty) = 1, \theta_{r+1}(\infty) = 0, \quad (8.29)$$

Where

$$a_{1,r} = 1 - \delta f_r^2, a_{2,r} = f_r + 2\delta f_r f'_r, a_{3,r} = -2f'_r + 2\delta f_r f''_r,$$

$$a_{4,r} = f''_r + 2\delta f'_r f''_r - 2\delta f_r f'''_r, R_{1,r} = f_r f''_r - (f'_r)^2 + 4\delta f_r f'_r f''_r - 2\delta f_r^2 f''_r,$$

$$b_{1,r} = 1 - \delta f_{r+1}^2, b_{2,r} = f_{r+1}, b_{3,r} = -f'_{r+1} + 2\delta f_{r+1} f''_{r+1}, R_{2,r} = A, c_{1,r} = Pr f_{r+1}.$$

Equations $(8.26) - (8.28)$ constitute a sequence of linear and decoupled equations so they are solved iteratively starting from a given initial approximation at $r = 0$. In this work, the Chebyshev spectral collocation method approach as described in [63] is chosen to integrate $(8.26) - (8.28)$. The domain in y is transformed in to the interval $[-1, 1]$ so that the spectral collocation method can be applied. For the convenience of the numerical computations,

the semi-infinite domain in y is approximated by the truncated domain $[0, L]$, where L is a finite number selected to be large enough to represent the behaviour of the flow properties when y is very large. We use the transformation $y = L\ (\eta + 1)/2$ to map the interval $[0, L]$ to $[-1, 1]$. The basic idea behind the spectral collocation method is the introduction of a differentiation matrix **D** which is used to approximate unknown derivatives of the function $f(y)$ at the grid points by the matrix vector product

$$\left.\frac{df(1)}{dy}\right|_{y_j} = \sum_{k=0}^{n} D_{jk}\, f(\eta k) = \mathbf{D}F, \quad j = 0,1, \dots, N \tag{8.30}$$

where $N + 1$ represents the total grid points, $\mathbf{D} = \frac{2D}{L}$ and

$$F = [F(\eta_0), F(\eta_1), \dots, F(\eta_N)]^T$$

denote vector function at collocation points. Similar vector functions corresponding to the other unknown functions such as h and θ are denoted by H and θ respectively. Moreover, other higher derivatives can be achieved by powers of D as

$$f^{(p)} = D^{(p)}F, h^{(p)} = D^{(p)}H, \theta^{(p)} = D^{(p)}\theta, \tag{8.31}$$

where p is the order of the derivative. The matrix D has the size $(N + 1) \times (N + 1)$. The grid points on y are defined as

$$\eta_j = \frac{cos\pi_j}{N}, \quad j = 0,1,2, \dots, N \tag{8.32}$$

Thus, applying the spectral method on equations $(8.26) - (8.28)$ give

$$A_1 F_{r+1} = R_{1,r}, \tag{8.33}$$

$$A_2 H_{r+1} = R_{2,r}, \tag{8.34}$$

$$A_3 \theta_{r+1} = R_{3,r}, \tag{8.35}$$

Where A_i $(i = 1, 2,3)$ are $(N + 1) \times (N + 1)$ matrices defined as:

$$A_1 = a_{1,r} D^3 + a_{2,r} D^2 + a_{3,r} D + a_{4,r}, \tag{8.36}$$

$$A_2 = b_{1,r} D^2 + b_{2,r} D + b_{3,r}, \tag{8.37}$$

$$A_3 = D^2 + c_{1,r} D + \lambda Pr\mathrm{I}, \tag{8.38}$$

and $R_{i,r}$ $(1,2,3,4)$ are $(N + 1) \times 1$ vectors obtained by evaluating the right hand sides of $(8.33) - (8.35)$ at the collocation points and incorporating the boundary conditions. The approximate solutions for $f(y)$, $h(y)$, and $\theta(y)$ are obtained by solving equations$(8.36) - (8.38)$. Figs $(8.2) - (8.4)$ are plotted to exhibit the residual errors for velocities and temperature profiles against elasticity parameter δ.

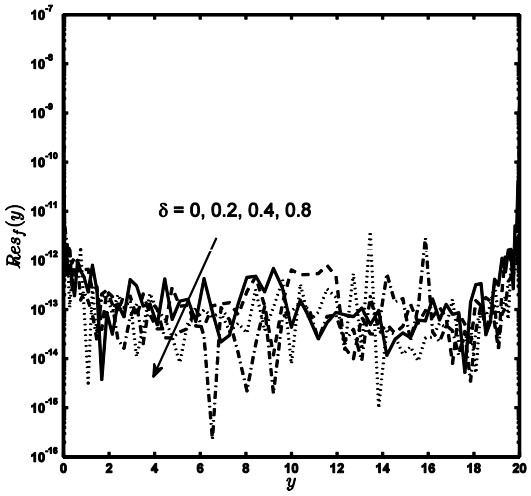

Fig (8.2): Residual Error for Normal flow $f(y)$.

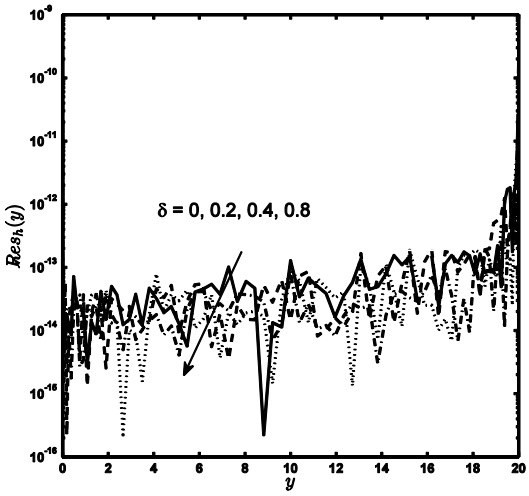

Fig (8.3): Residual Error for tangential flow $h(y)$.

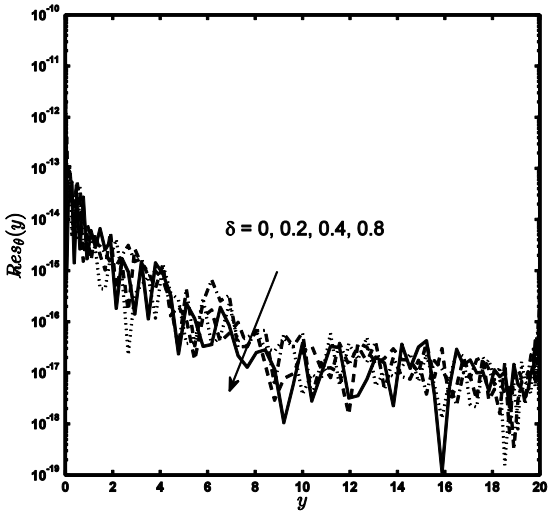

Fig (8.4): Residual Error for temperature profile $\theta(y)$.

8.5 Analysis of Graphical Results

The main purpose of this section is to study the influence of emerging parameters on non-dimensional quantities such as normal and tangential velocities, temperature profile and local heat flux rate at the convective surface. Figs (8.5) – (8.16) are prepared for this purpose. Figs

(8.5) and (8.6) describe the effects of Deborah number δ on normal $f'(y)$ and tangential component of velocity $h'(y)$ respectively. It is quite obvious from these figures that Deborah number δ has opposite influence on both the velocities. Normal component of the velocity $f'(y)$ decreases while tangential component of the velocity $h'(y)$ increases near the wall with an increase in δ. The effects of Deborah number δ and Biot number Bi on temperature profile $\theta(y)$ are presented through Figs (8.7) and (8.8) and found that $\theta(y)$ increases with Deborah number δ and Biot number Bi. Impact of heat source/sink parameter λ on the temperature profile $\theta(y)$ is expressed through Figs (8.9) and (8.10). These results clearly indicate that temperature profile $\theta(y)$ increases with an increase in heat generation ($\lambda > 0$) but it decreases with heat absorption ($\lambda < 0$). This is in good agreement with the physical situation because an internal heating naturally causes the temperature of the fluid to rise up and vice versa. Fig (8.11) shows that temperature profile $\theta(y)$ with prandtl number Pr as higher Prandtl nubmer means less thermal conductivity which casues the temperature to drop down. From Figs (8.12) and (8.13), it is noticed that local heat flux rate $-\theta'(0)$ increases with heat absorption parameter ($\lambda < 0$) and it decreases with heat generation parameter ($\lambda > 0$). Moreover, it is also observed from these figures that local heat flux rate $-\theta'(0)$ tends to decrease with an increase in Deborah number δ for heat generation as well as absorption case. Figs (8.14) and (8.15) are plotted to discover the effect of prandtl number Pr on local heat flux rate $-\theta'(0)$ for heat source and sink respectively. These results show that heat flux rate $-\theta'(0)$ increase as we increase the values of Pr. This increasing behaviour is found to be quite similar for both heat genaration and absorption cases. Finally, the influence of Biot number Bi on the heat flux rate $-\theta'(0)$ is discovered through Fig (8.16). It can be seen that heat flux rate $-\theta'(0)$ increases with an increase in Biot number Bi.

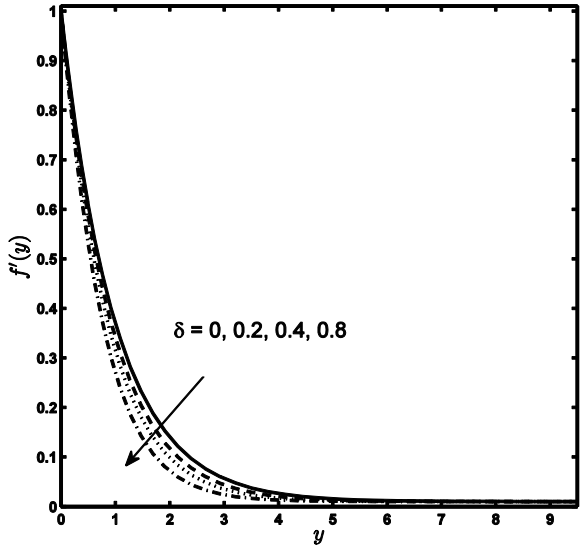

Fig (8.5): Velocity profile $f'(y)$ against δ.

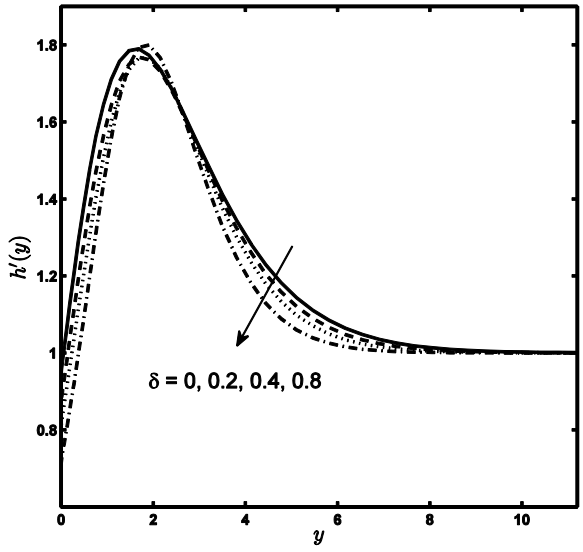

Fig (8.6): Velocity profile $h'(y)$ against δ.

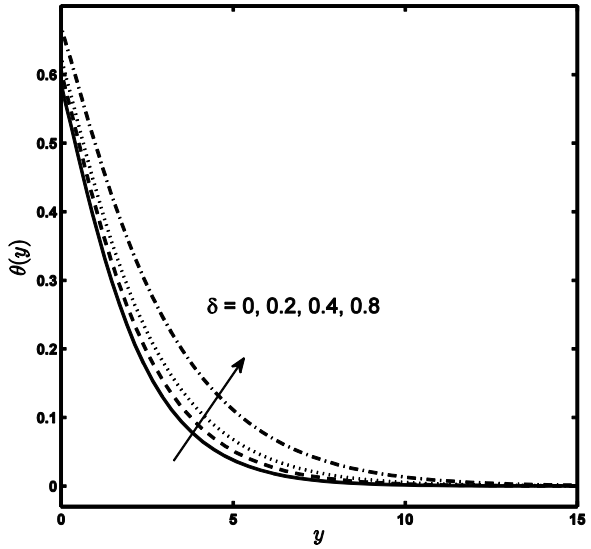

Fig (8.7): Temperature profile $\theta(y)$ against δ

when $Pr = 0.7,\ Bi = 0.5,\ \lambda = 0.1.$

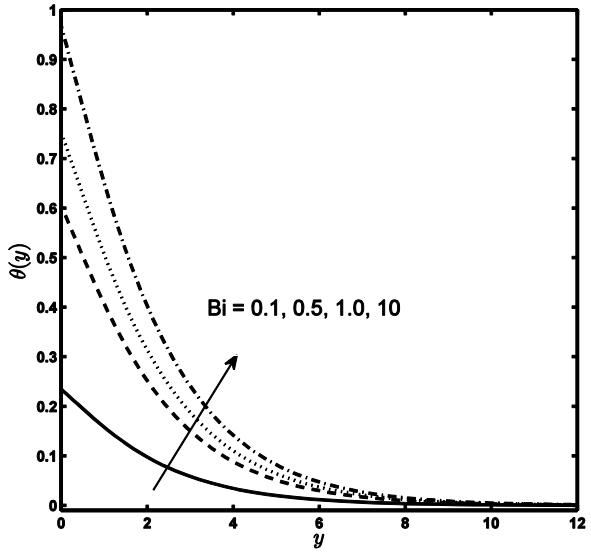

Fig (8.8): Temperature profile $\theta(y)$ against Bi

when $Pr = 0.7,\ \delta = 0.2,\ \lambda = 0.1.$

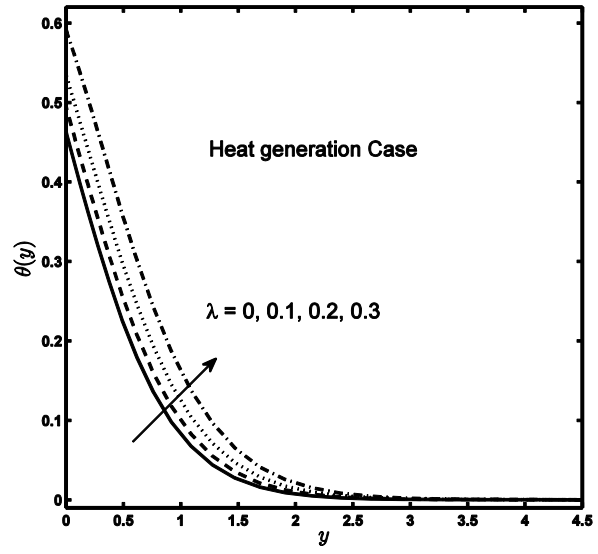

Fig (8.9): Temperature profile $\theta(y)$ against heat generation parameter ($\lambda > 0$) when $Pr = 3.0,\ Bi = 1.0,\ \delta = 0.1$.

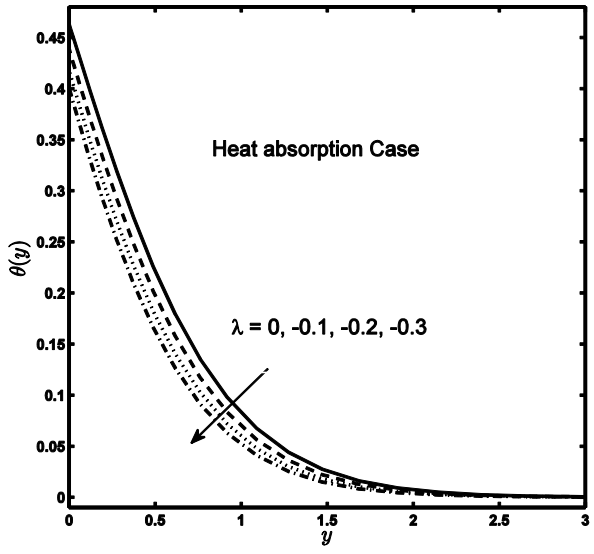

Fig (8.10): Temperature profile $\theta(y)$ against heat absorption

parameter ($\lambda < 0$) when $Pr = 3.0,\ Bi = 1.0,\ \delta = 0.1$.

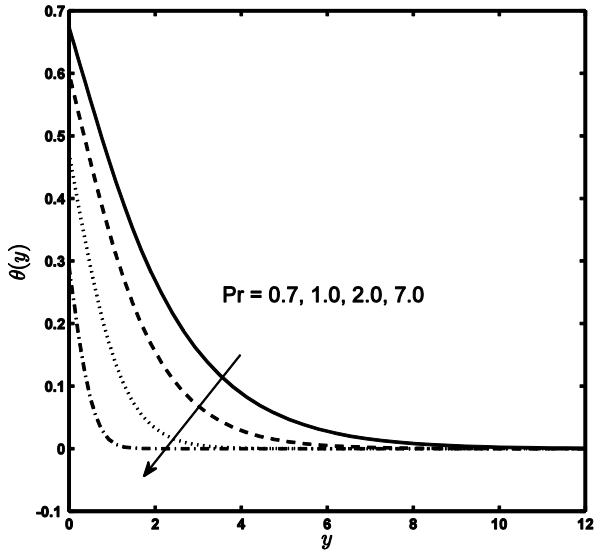

Fig (8.11): Temperature profile $\theta(y)$ against Pr

when $\lambda = 0.10,\ Bi = 0.7,\ \delta = 0.1$.

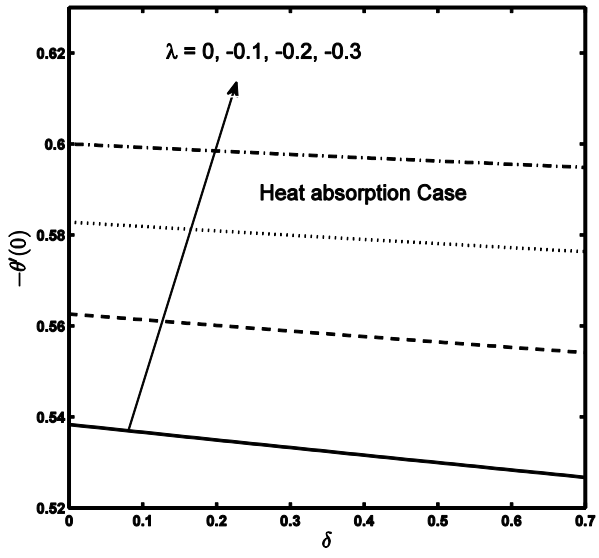

Fig (8.12): Local heat flux $-\theta'(0)$ against δ for heat absorption

case ($\lambda < 0$) when $Pr = 3.0,\ Bi = 1.0$.

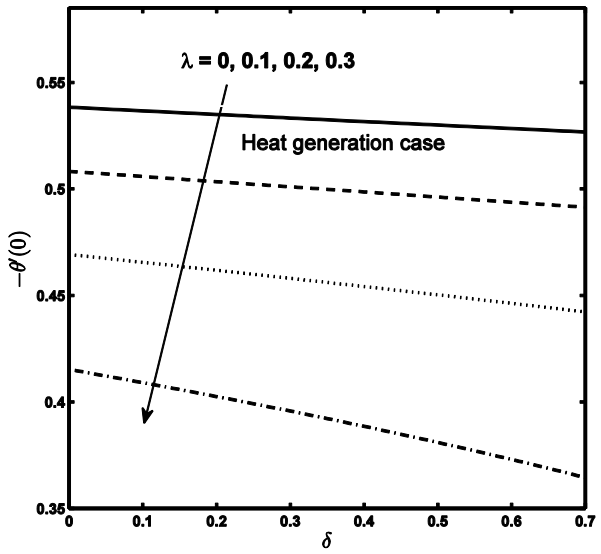

Fig (8.13): Local heat flux $-\theta'(0)$ against δ for heat generation

case ($\lambda > 0$) when $Pr = 3.0,\ Bi = 1.0$.

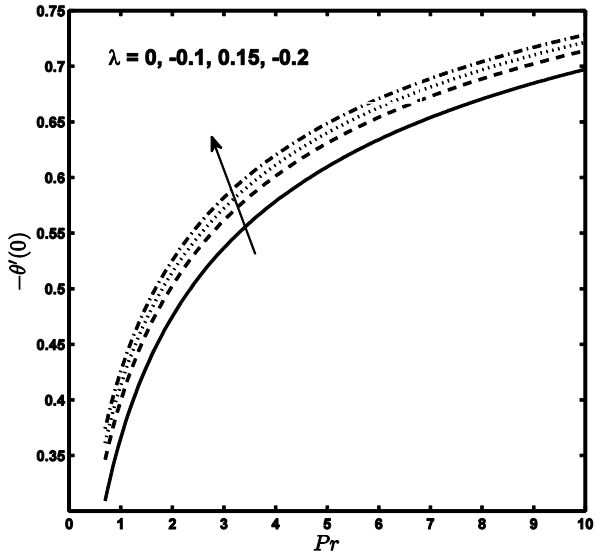

Fig (8.14): Local heat flux $-\theta'(0)$ against Pr for heat absorption

case $(\lambda < 0)$ when $\delta = 0.1,\ Bi = 1.0$.

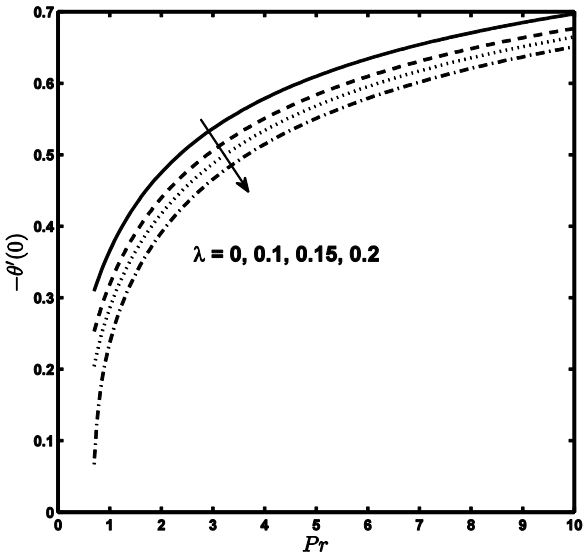

Fig (8.15): Local heat flux $-\theta'(0)$ against Pr for heat generation

case $(\lambda > 0)$ when $\delta = 0.1,\ Bi = 1.0$.

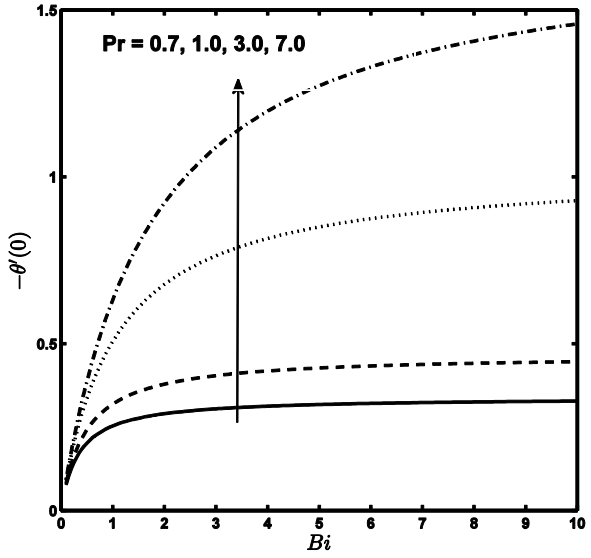

Fig (8.16): Local heat flux $-\theta'(0)$ against Bi for heat generation

case ($\lambda > 0$)when $\delta = 0.1,\ \lambda = 0.1$.

8.6 Concluding Remarks

The oblique stagnation point Maxwell fluid flow has been explored numerically with internal heat generation/absorption over a convective surface. The governing non-linear coupled ordinary differential equations are solved through Spectral Quasilinearization Method (QLM) and Spectral Local Linearization Method (LLM). The key points of this study are:

- It is found that elasticity parameter δ has opposite influence on normal and tangential components of velocity while it increases the temperature profile.
- The Prandtl number enhances the surface heat transfer for heat generation as well as heat absorption case.
- Local heat flux decreases with heat generation and increases with an increase in heat absorption parameter.

References

[1] K. Hiemenz, Die Grenzschicht an einem in den gleichförmigen Flüessigkeitsstrom eingetauchten geraden Kreiszylinder. Dinglers Polytechnisches Journal. (1911)321.

[2] L. Howarth, CXLIV. The boundary layer in three dimensional flows. Part II. The flow near a stagnation point, Philosophical Magazine (Series 7), (1951)1433.

[3] J. T. Stuart, The viscous flow near a stagnation point when the external flow has uniform vorticity, J. Aerospace Sci. 26(1959) 124.

[4] K. J. Tamada, Two-dimensional stagnation point flow impinging obliquely on a plane wall, J. Phys. Soc. Jpn. 46(1979)310.

[5] J. M. Dorrepaal, An exact solution of the Navier-Stokes equation which describes non-orthogonal stagnation-point flow in two dimensions, J. Fluid Mech. 163(1986)141.

[6] T. C. Chiam, Stagnation-point flow towards a stretching plate, J. Phys. Soc. Jpn. (1994)2443.

[7] T.R. Mahapatra, A.S. Gupta, Heat transfer in stagnation-point flow towards a stretching sheet, Heat Mass Transf. (2002)521

[8] T.R. Mahapatra, S.K. Nandi, A.S. Gupta, Dual Solution of MHD Stagnation-Point Flow towards a Stretching Surface, Engineering, 2 (2010) 299.

[9] Y.Y. Lok, A. Ishak, I. Pop, MHD stagnation-point flow towards a shrinking sheet, Int. J. Num. Meth. Heat Fluid Flow, 21 (2011) 61.

[10] M. Reza and A.S. Gupta, Steady two-dimensional oblique stagnation-point flow towards a stretching surface, Fluid Dyn. Res. 37 (2005) 334.

[11] Y.Y. Lok, I. Pop, A. J. Chamkha, Non-orthogonal stagnation-point flow of a micropolar fluid. Int. J. Engg. Sci. 45 (2007) 184.

[12]T. R. Mahapatra, S. Dholey and A. S. Gupta, Oblique Stagnation-Point flow of an Incompressible Visco-Elastic Fluid to-wards a Stretching Surface, Int. J. Non-Linear Mech, 42 (2007) 484.

[13]M. Reza and A.S. Gupta, Some Aspects of Non-Orthogonal Stagnation-Point Flow towards a Stretching Surface, Engineering, 2 (2010) 705.

[14]F. Labropulu, D. Li and I. Pop, Non-orthogonal stagnation-point flow towards a stretching surface in a non-Newtonian fluid with heat transfer, Int. J. Therm. Sci.49(2010)1042.

[15]A. Kimiaeifar, and G.H. Bagheri, On the Analytical Solution of Non-Orthogonal Stagnation Point Flow towards a Stretching Sheet, Int. J. Appl. Math, 41 (2011) 89.

[16]K. Walters, Second-Order Effects in Elasticity, Plasticity and Fluid Dynamics, Pergamon, Oxford, 1964.

[17]J.C. Maxwell, On the dynamical theory of gases. Philosophical Transactions of the Royal Society London. A157 (1866) 26.

[18]K.R. Rajagopal, A note on novel generalizations of the Maxwell fluid model, Int. J. Non-Linear Mech. 47 (2012) 72.

[19]M. Nakamura and T. Sawada, Numerical study on the flow of a non-Newtonian fluid through an axisymmetric stenosis, J. Biomechanical Engg. 110 (1988) 137.

[20]M.S. Abel and N. Mahesha, Heat transfer in MHD viscoelastic fluid flow over a stretching sheet with variable thermal conductivity, non-uniform heat source and radiation, Appl. Math. Modell. 32 (2008) 1965.

[21]A. Ahmad, S. Asghar, Flow of a second grade fluid over a sheet stretching with arbitrary velocities subject to a transverse magnetic field, Appl. Math. Lett. 24 (2011) 1905.

[22]H. Xu, S.J. Liao, Laminar flow and heat transfer in the boundary-layer of non-Newtonian fluids over a stretching flat sheet, Comput. Math. Appl. 57 (2009) 1425.

[23]H. Xu, S.J. Liao, Series solutions of unsteady magnetohydrodynamic flows of non-Newtonian fluids caused by an impulsively stretching plate, J. Non-Newton. Fluid Mech. 129 (2005) 46.

[24]R. Nazar & N. Latip, Numerical investigation of three-dimensional boundary layer flow due to a stretching surface in a viscoelastic fluid, Europ. J. Sci. Res. 29 (2009) 509.

[25]K.V. Prasad, P. Dulal, V. Umesh & N.S. Prasanna Rao, The effect of variable viscosity on MHD viscoelastic fluid flow and heat transfer over a stretching surface, Commun. Nonlinear Sci. Num. Simulat. 15 (2010) 331.

[26]U. S. Choi, Enhancing thermal conductivity of fluids with nanoparticles, in: D. A. Siginer and H. P. Wang (editors), Developments and Applications of Non-Newtonian Flows, ASME FED. 66 (1995) 105.

[27]N. Putra, W. Roetzel and S. K. Das, Natural convection of nano-fluids, Heat Mass Transf. 39 (2003) 784.

[28]Y. Xuan and Q. Li, Investigation on convective heat transfer and flow features of nanofluids, J. Heat Transf. 125 (2003) 151.

[29]J. Buongiorno, Convective transport in nano fluids, ASME J. Heat transf. 128 (2006) 240.

[30]A.V. Kuznetsov and D.A. Nield, Natural convective boundary layer flow of a nano fluid past a vertical plate. Int. J. Therm. Sci. 49 (2010) 243.

[31]N. Bachok, A. Ishak and I. Pop, Stagnation-point flow over a stretching/shrinking sheet in a nanofluid, Nanoscale Research Lett. 6 (2011) 623.

[32]H.I. Anderson, MHD flow of a viscoelastic fluid past a stretching surface, Acta Mech. 95 (1992) 227.

[33] A. Ishak, K. Jafar, R. Nazar and I. Pop, MHD stagnation point flow towards a stretching sheet, Physica A. 388 (2009) 3377.

[34]R. Ellahi, Arshad Riaz, Analytical solutions for MHD flow in a third-grade fluid with variable viscosity, Math. Comput. Modell. 52 (2010) 1783.

[35]F.M. Ali, R. Nazar, N.M. Arifin, I. Pop, MHD boundary layer flow and heat transfer over a stretching sheet with induced magnetic field, Heat Mass Transf. 47 (2011) 155.

[36]Navier CLMH, Sur les lois du mouvement des fluids, Men Acad R Sci Instt. France. 6 (1827) 389.

[37]H. I. Andersson, Slip flow past a stretching surface, Acta Mech. 158 (2002) 11.

[38]C.Y. Wang, Flow due to a Stretching Boundary with Partial Slip – An Exact Solution of the Navier-Stokes Equations, Chem. Engg. Sci. 57 (2002) 3745.

[39]C.Y. Wang, Stagnation Flows with Slip, Exact Solutions of the Navier-Stokes Equations, ZAMP 54 (2003) 184.

[40]F. Labropulu, I. Husain, and M. Chinichian, Stagnation Point Flow of The Walters' B' Fluid with Slip, Int. J. Math. Math. Sci. 61 (2004) 3249.

[41]P.D. Ariel, Two dimensional stagnation point flow of an elastico-viscous fluid with partial slip, ZAMM · Z. Angew. Math. Mech. 88 (2008) 320.

[42]M. Turkyilmazoglu, Multiple solutions of heat and mass transfer of MHD slip flow for the viscoelastic fluid over a stretching sheet. Int. J. Therm. Sci. 50 (2011) 2264.

[43]A. Aziz, A similarity solution for laminar thermal boundary layer over a flat plate with a convective surface boundary condition, Commun. Nonlinear Sci. Numer. Simulat. 14 (2009)

1064.

[44]O.D. Makinde, Similarity solution of hydromagnetic heat and mass transfer over a vertical plate with a convective surface boundary condition, Int. J. Phys. Sci. 5 (2010) 700.

[45]A. Ishak, Similarity solutions for flow and heat transfer over a permeable surface with convective boundary condition, Appl. Math. Comput. 217 (2010) 837.

[46]O.D. Makinde, P.O. Olanrewaju, Buoyancy effects on thermal boundary layer over a vertical plate with a convective surface boundary condition, Trans. ASME J. Fluid Eng. 132 (2010) 044502.

[47]A. Aziz, Hydrodynamic and thermal slip flow boundary layers over a flat plate with constant heat flux boundary condition, Commun. Nonlinear Sci. Numer. Simulat. 15 (2010) 573.

[48]O.D. Makinde, A. Aziz, MHD mixed convection from a vertical plate embedded in a porous medium with a convective boundary condition, Int. J. Therm. Sci. 49 (2010) 1813.

[49]O.D. Makinde, On MHD heat and mass transfer over a moving vertical plate with a convective surface boundary condition, Can. J. Chem. Eng. 88 (2010) 983.

[50]O.D. Makinde, T. Chinyoka, L. Rundora, Unsteady flow of a reactive variable viscosity non-Newtonian fluid through a porous saturated medium with asymmetric convective boundary conditions, Comput. Math. Appl. 62 (2011) 3343.

[51]R. Tsai, J.S. Huang, Heat and mass transfer for Soret and Dufour's effects on Hiemenz flow through porous medium onto a stretching surface, Int. J. Heat Mass Transf. 52 (2009) 2399.

[52]O. Beg Anwar, A.Y. Bakier, V.R. Prasad, Numerical study of free convection magneto hydrodynamic heat and mass transfer from a stretching surface to a saturated porous medium with Soret and Dufour effects. Comput. Mater. Sci. 46 (2009) 57.

[53]A.A. Afify, Similarity solution in MHD: effects of thermal-diffusion and diffusion-thermo on free convective heat and mass transfer over a stretching surface considering suction or injection, Commun. Nonlinear Sci. Numer. Simulat. 14 (2009) 2202.

[54]D. Pal, H. Mondal, Effects of Soret Dufour, Chemical Reaction and Thermal Radiation on MHD Non-Darcy Unsteady Mixed Convective Heat and Mass Transfer over a Stretching Sheet, Commun. Nonlinear Sci. Numer. Simulat. 16 (2011) 1942.

[55]S.J. Liao, On the homotopy analysis method for nonlinear problems. Appl Math Comput. 147 (2004) 499.

[56]S.J. Liao, Notes on the Homotopy analysis method: Some definitions and theorems, Comm. Nonlinear. Sci. Numer. Simulat, 14 (2009) 983.

[57]A. Alizadeh-Pahlavan, V. Aliakbar, F. Vakili-Farahani, K. Sadeghy. MHD flows of UCM fluids above porous stretching sheets using two-auxiliary-parameter homotopy analysis method. Commun Nonlinear Sci Numer Simulat. 14 (2009) 473.

[58]S. J. Liao, An optimal Homotopy-analysis approach for strongly nonlinear differential equations, Commun. Nonlinear Sci. Numer. Simulat. 15 (2010) 2003.

[59]S. Abbasbandy, Numerical solutions of the integral equations: Homotopy perturbation method and Adomian's decomposition method, Math. Comput. Modell. 173 (2010) 493.

[60]A.A. Joneidi · G. Domairry · M. Babaelahi, Homotopy Analysis Method to Walter's B fluid in a vertical channel with porous wall, Meccanica 45 (2010) 857.

[61]S.J. Liao, On the analytic solution of magneto hydrodynamic flows of non-Newtonian fluids over a stretching sheet, J. Fluid Mech. 488 (2003) 189.

[62]R. E. Bellman and R.E. Kalaba, Quasilinearization and nonlinear boundary-value problems, Elsevier, New York, 1965.

[63]L. N. Trefethen, Spectral Methods in MATLAB, SIAM, 2000.

[64]W. Ibrahim and B. Shanker, Unsteady Boundary Layer Flow and Heat Transfer Due to a Stretching Sheet by Quasilinearisation Technique, World J. Mech. 1(6) 2011.

[65]U. Ascher, R. Mattheij, R. Russell. Numerical Solution of Boundary Value Problems for Ordinary Differential Equations. SIAM Classics in Applied Mathematics 1995; 13:327-357.

[66]U. Ascher, L. Petzold. Computer Methods for Ordinary Differential Equations and Differential-Algebraic Equations. SIAM Philadelphia 1998.